UiO **:** **Department of Chemistry**
University of Oslo

Copper-based Photocathode for Solid State Photoelectrochemical Cell

Lars Kristian Henriksen
M.Sc. Thesis, Spring 2018

Copper-based Photocathode for Solid State Photoelectrochemical Cell

Lars Kristian Henriksen

M.Sc. thesis
in Materials, Energy and Nanotechnology
60 credits

Department of Chemistry
Faculty of Mathematics and Natural Sciences

UNIVERSITY OF OSLO

May 2018

Acknowledgements

My supervisors have been instrumental in the realisation of this thesis. I wish to thank Prof. Truls Norby for giving me the opertunity to work on such an exciting project, and for his guidance and ever constructive feedback, i am grateful. I would like to thank Dr. Athanasios E. Chatzitakis, Dr. Tor S. Bjørheim and Kaiqi Xu for the fruitful discussions we have had and the insights you have provided. For her help with TEM analysis, i would like to thank Patricia Almeida Carvalho at Sintef.

Also, I am truly grateful to my family and friends for their love and support through all these years.

Finally, my biggest and most sincere thanks goes to Kristin, the love of my life. You made this possible.

This is to you.

Summary

Realizing cheap, effective, and non-toxic electrode materials for efficient solar-to-hydrogen conversion are of great interest as hydrogen is in demand. Oxide semiconductors are particularly interesting, and this work investigates two copper-based oxides as candidates for use in photoelectrochemical cells, namely cuprous oxide (Cu_2O) and delafossite ($CuFeO_2$).

Cu_2O photoactive nanostructures have been deposited on several substrates over a range of deposition parameters with the aim of establishing a route for making high-performance photocathodes for use in photoelectrochemical cells for direct solar water splitting.

Spontaneous potential oscillations encountered during galvanostatic deposition of Cu_2O was investigated to understand the deposition system better, and subsequently to find ways to avoid the oscillations, as metallic Cu in Cu_2O electrodes are known to degrade photocatalytic performance. By intentionally initiating oscillations after a period of steady Cu_2O deposition, distinct cauliflower structures arose that were then studied by STEM, XRD, and EDS; this provided evidence of metallic Cu depositing as a direct consequence of potential oscillations. By avoiding potential oscillations, galvanostatic deposition of high quality crystalline Cu_2O samples was made possible.

Several substrates were used to deposit Cu_2O, and it was found that stainless steel mesh outperformed Ti-mesh and carbon-paper substrates in regards to surface coverage, reproducibility and measured photocurrents; the best Cu_2O electrode deposited on ss-mesh exhibited a photocurrent in excess of -1.0 mA cm^{-2} at -0.6 V vs. SCE. However, photocorrosion of the Cu_2O photocathode was anticipated, and through prolonged exposure to light in a 0.5 M $NaSO_4$ electrolyte, degradation was confirmed. After approximately 350 s of illumination, the photocurrent was reduced from to less than 15% of an initial photocurrent of -1.0 mA cm^{-2} at -0.6 V vs. SCE.

As the primary hypothesis to be tested in this project was whether Cu_2O would remain stable under dry conditions in a solid-state photoelectrochemical cell, a custom-made SS-PEC cell was constructed to facilitate the photoelectrochemical measurements, and dry conditions were imposed on the cathode, while the anode was provided with wet Ar. The SS-PEC cell utilizing a Pt-C-electrocatalyst as an anode material initially displayed a photocurrent of -1.5 µA cm^{-2} at -2.0 V vs. Pt-C, but this dropped to -0.8 µA cm^{-2} after approximately 1800 s of illumination. This might seem like a small drop in photocurrent over an extended period, compared to previously discussed results, but as the reduction of Cu_2O is electrochemical, low photocurrents will equal low reduction rates. The conclusion is hence that Cu_2O reduces to metallic Cu even if kept in a dry atmosphere. The reduction is attributed to the fact that as protons are supplied to the Cu_2O photocathode, the energetically favourable reduction is

$$Cu_2O + 2e^- + 2H^+ \rightarrow Cu + H_2O \quad \text{rather than} \quad 2H^+ + 2e^- \rightarrow H_2$$

Upon confirming degradation of performance in SS-PEC cells experimentally, alternatives were dis-

cussed, and two main routes were investigated; one was to cover the Cu_2O electrode with a protective layer, the other was to find another copper-based oxide materials that could replace Cu_2O and remain stable during PEC operations.

By covering the Cu_2O electrode with a layer of amorphous TiO_2 deposited by PLD, an increase in photocurrent to 1.38 mA cm^{-2} at -0.6 V vs. SCE in a 0.5 M $NaSO_4$ electrolyte was observed. This was 0.28 mA higher than the best *bare* Cu_2O electrode, as mentioned above, and approximately ten times higher than that found in reference samples with the same deposition parameters. However, electrode instability persisted, and after ~280 s of illumination photocurrents dropped to less than 10% of the initial photocurrent and it was concluded that a layer of TiO_2 alone was not able to stabilize the Cu_2O electrode

Other, more stable, copper-based oxides could potentially be used instead of Cu_2O, and efforts were directed to the preparation and characterization of delafossite, $CuFeO_2$; a material that has been shown in the literature to exhibit excellent prospects as a photocathode material for PEC operations. The drawback of $CuFeO_2$ is that the methods for preparation are not as straightforward as is for Cu_2O. This work sets out to explore preparation of $CuFeO_2$ by electrodeposition, but resulting samples showed no signs of Fe, presumably because of unoptimized deposition parameters, and annealed samples were mainly comprised of quasi-spherical Cu-agglomerates on the FTO surface.

Even if this work did not succeed in depositing $CuFeO_2$ electrodes, the project as a whole has expanded the understanding of electrochemically deposited Cu_2O, and in investigating the spontaneous potential oscillations that emerge during galvanostatic deposition of Cu_2O, completely new insights have been presented. High quality Cu_2O samples have been realised, and it has been shown that these electrodes show both photocurrent and photovoltage in solid-state PEC cell operations.

Abbreviations

ABF	Annular bright field
ADF	Annular dark field
ALD	Atomic layer deposition
CA	Chronoamperometry
CB	Conduction band
CBM	Conduction band minimum
CV	Cyclic voltammetry
CGB	Compositionally graded buffer
DI	De-ionized
DMSO	Dimethylsulfoxide
DOS	Density of states
EDS	Energy-dispersive x-ray spectroscopy
ETD	Everhart Thornley detector
FEG-ESEM	Field emission gun - environmental SEM
FIB	Focused ion beam
FTO	Flourine-doped tin-oxide (SnO_2)
HAADF	High angle annular dark field
HER	Hydrogen evolution reaction
IHP	Inner Helmholtz plane
LSV	Linear sweep voltammetry
OCP	Open circuit potential
OER	Oxygen evolution reaction
OHP	Outer Helmholtz plane
PLD	Pulsed laser deposition
PV	Photovoltaic
RHE	Reversible hydrogen electrode
SCE	Saturated calomel electrode
SEM	Scanning electron microscope
SHE	Standard hydrogen electrode
STH	Solar-to-hydrogen efficiency
SSD	Solid-state detector
SS-PEC	Solid-state photoelectrochemical
STEM	Scanning transmission electron microscope
VASP	Vienna *ab initio* simulation package
VB	Valence band
VBM	Valence band maximum
XC	Exchange-correlation
XPS	X-ray photoelectron spectroscopy
XRD	X-ray diffraction

Contents

1   Introduction

As the earth and its inhabitants move into unknown climate territory, the quest for solutions that can contribute to the stagnation, or reduction, of global warming is on. In 2017 the Norwegian Research Council (NRC) funded "climate, environment, and green energy"-related areas with 1046 MNOK, almost 10% of the total NRC project funding in 2017. [1] This shows that Norway, as part of the growing number of countries to ratify the Paris climate agreement of 2015, is committing to a green shift.

Fuels to drive our plant are in high demand, and choices as to what sort of fuel we want to use are emerging. We are witnessing explosive growth in the number of electric vehicles populating our roads, and both private transportation, and transportation of heavy goods, see electrification. However, a significant disadvantage of electric vehicles is the long charging times. Rapid charging of car batteries are available to the consumer today, but charging times can never become sufficiently short, according to some experts. Besides, 'supercharging' reduces battery life-times substantially. [2]

A great alternative to electricity as a fuel is hydrogen. Refueling hydrogen is fast and emits only pure water when used. Quick refueling times become especially important when we consider bigger vehicles, such as ships and planes. Since the emissions are purified water, hydrogen also makes for an excellent fuel in areas hit by disasters and catastrophes. For instance, in the U.S., fuel cells are already being used as on-site backup power generators during natural disasters such as the hurricane Katrina. [3]

1.1   Hydrogen as Energy Carrier

Hydrogen as an energy carrier has gained a fair amount of attention during the last decade. It can be used directly as fuel in combustion engines, but a more expedient way to utilize hydrogen is to use it in fuel cells. Today there are several series-production cars from manufacturers like Nissan and Toyota, which run on hydrogen fuel cells. In the future, we might expect to see an increase in hydrogen utilization in the transport sector, and as the demand increases so does the demand for production.

Producing hydrogen is typically done by either natural gas reforming or electrolysis. These methods usually require lots of energy and, in the case of natural gas reforming, it is based on fossil fuels. Additionally, if the energy needed to produce hydrogen originates from fossil fuels, it is clear that new and green alternatives are required to meet present and future consumer needs.

Photocatalytic water splitting is a promising technology and might one day be able to deliver clean cost-efficient hydrogen. This photocatalytic process can in many aspects be compared to photosynthesis in plants. As the leaves use the incident energy of sunlight to convert CO_2 to sugars, the photocatalytic process mentioned above would use the incoming light to split water. To achieve this, we have to select materials that absorb light in such a way that the energy of the incident light is converted to energy we can use to break up the H_2O molecule. If we combine this material with another material that absorbs light in

the same way but use the harvested energy to selectively combine the broken pieces of H_2O into hydrogen gas, a system capable of making hydrogen gas from water emerges.

The challenges to this technology are that the conversion efficiency is low, and the power of the incident sunlight will limit the current densities obtainable from these devices. A solar-to-hydrogen (STH) device would require 50-200 times the electrode area of conventional electrolyzers, so to make such technology viable both the production- and running cost need to be sufficiently low. The Fuel Cell Technologies Office (part of the U.S. Department of Energy's Office of Energy Efficiency and Renewable Energy) predicts that production of hydrogen gas must fall below $2/kg to become a viable source of fuel. [4]

One way to achieve this is to use cheap materials in combination with low-cost manufacturing methods, and at the same time operate as a self-contained system not relying on external driving forces.

1.2   Oxide-based Photocathodes for Hydrogen Production

In the review article *Emerging earth-abundant materials for scalable solar water splitting* by Septina et al. [5] it is stated that ...*in order to reduce the cost of solar hydrogen, new Earth- abundant light absorber materials are needed that can be fabricated with less cost than crystalline silicon, while maintaining high solar-to-hydrogen (STH) efficiency and stability of at least several years*. As a result, we see a lot of research directed towards low cost, p-type oxide semiconductors.

One disadvantage of oxides semiconductors is that many of these oxides are very unstable when operated in aqueous solutions under illumination and as a result photocorrodes. This photocorrosion is an obvious handicap of such a system, and hence, a lot of effort has been made to stabilize these oxides. A standard way to avoid this problem is to cover the oxide photoabsorber with one or several protective layers to enhance stability and increase performance. Paracchino et al. [6] give an example of a state of the art photocathode for hydrogen evolution based on Cu_2O, reporting a photocurrent of -5.7 mA cm^{-2} at 0 V vs. RHE with excellent stability; achieved by protecting the Cu_2O surface with a $ZnO/Al_2O_3/TiO_2$ 'sandwich'. This protective layer not only functions as a Cu_2O stabilizer but also increase the photocatalytic performance of the electrode. A table highlighting several other emerging photocathode materials, most of which have protective layers, are provided in ref. [5]

1.3   Aims of the Thesis

This project aims to assess Cu_2O as a photocathode material for implementation in a solid state photo-electrochemical (SS-PEC) cell. The Electrochemistry (ElChem)[1] group at the University of Oslo is working on novel tandem cells capable of unassisted photoelectrochemical hydrogen production. In such a set-up light excites an electron hole pair at the anode by

---

1   http://www.mn.uio.no/kjemi/english/research/groups/solid-state-electrochemistry-fase/
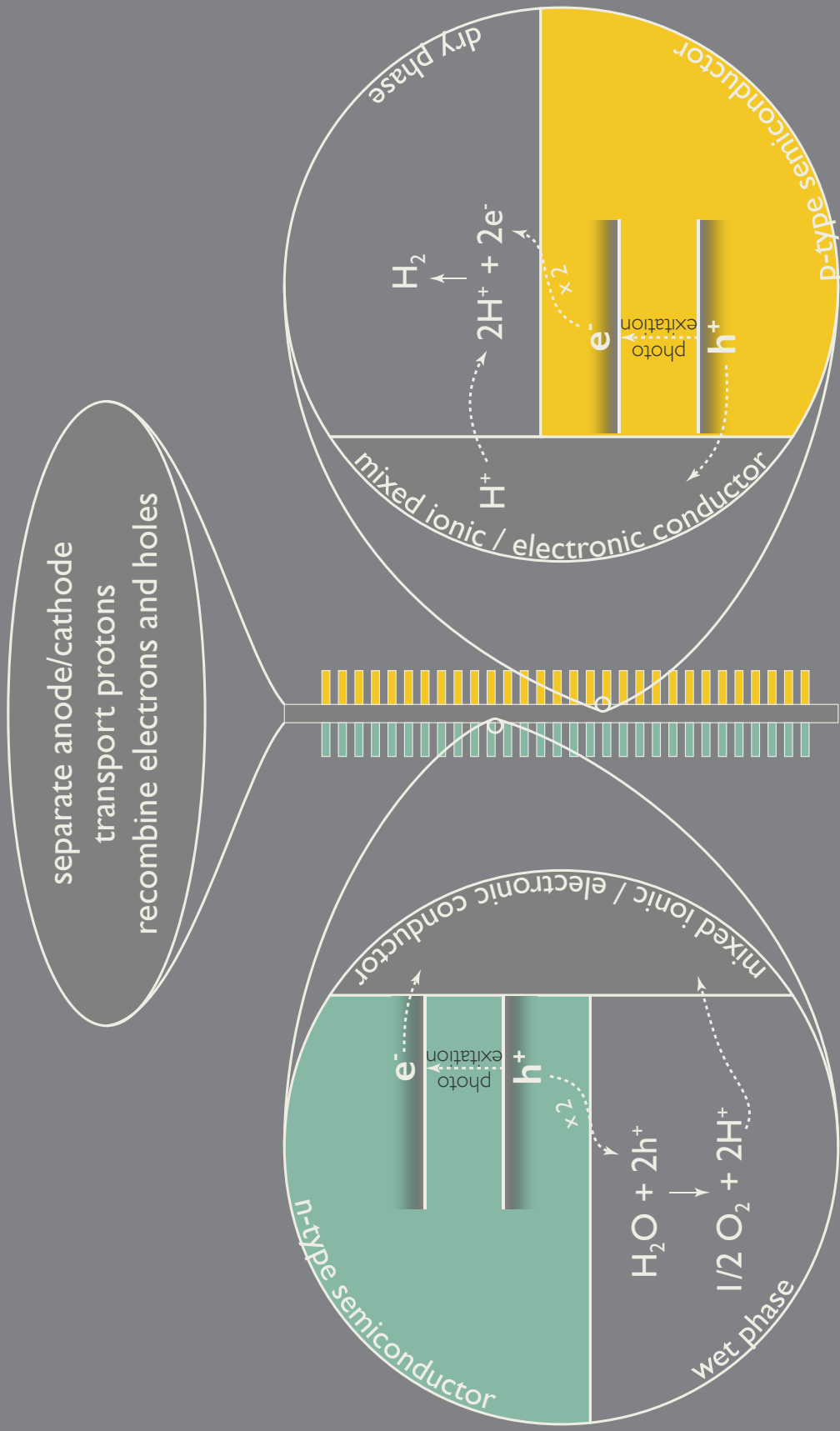
figure 1: Schematics of SS-PEC cell and the reactions occurring at the different locations. Left (anode): oxidizing water by photoexcited holes on the anode surface with subsequent proton transport to the membrane. Right (cathode): reducing protons by photoexcited electrons, forming hydrogen gas. Center: facilitate the recombination of anode electrons and cathode holes and transport protons from the anode to cathode side. This idealized cell utilizes a mixed conductor membrane.

$$h\nu \rightarrow e^- + h^+ \qquad (1.1)$$

where the resulting holes facilitate the oxidation of water through

$$H_2O \ (l) + 2 \ h^+ \rightarrow 2 \ H^+ \ (aq) + 1/2 \ O_2 \ (g) \qquad (1.2)$$

using mainly the UV part of the solar spectrum. Thereafter, protons (H^+) are transported through a sol-id-state electrolyte, providing the cathode with protons, whereupon using additional photons from the visible range of the solar spectrum can drive the reduction

$$2 \ H^+ \ (aq) + 2 \ e^- \rightarrow H_2 \ (g) \qquad (1.3)$$

In their study of the ...*optimal band gaps of light absorbers in integrated tandem photoelectrochemical water-splitting systems*, Hu et al. [7] indirectly shows that there are many candidates for the task of reducing protons, one of these being Cu_2O, which has a well-suited band structure for driving this reaction, but the drawback of having Cu_2O in a conventional photoelectrochemical cell is the photocorroding nature of Cu_2O when exposed to light and water simultaneously. [8]

The main hypothesis to be tested in this project is whether Cu_2O will remain stable under dry conditions in a SS-PEC cell or not. A Cu_2O photocathode is accomplished by depositing Cu_2O on different conducting substrates, subsequently combining this photocathode with a photoanode to make a full n-p like solid state PEC cell. A proton conducting polymer membrane separate the n-type anode and p-type cathode, thus hindering Cu_2O from reacting with water by keeping the water vapor confined to the anode side. The role of the membrane, apart from the proton conductivity and water confinement, is to provide structural support for the anode and cathode electrodes, as well as to separate the gaseous hydrogen and oxygen products. This set-up depends on short circuiting the two sides by an external circuit in order to transport the excited electrons from n- to p-side.

Schematics of an idealized purpose-built solar-to-hydrogen SS-PEC cell is shown in figure 1 with the anode to the left and cathode to right. In this figure a *mixed conductor* membrane is used as a vehicle for both proton and electron/hole conductivity. In this case an external circuit would be obsolete, and the unit would be totally self-contained.

This project will also be a proof-of-concept for a full n-p like SS-PEC cell, constructed and operated under asymmetric conditions as shown by Xu et al. [9]. In this work, asymmetric conditions translate to keeping the anode of such SS-PEC cell in humidified Ar (80% humidity), while the cathode is kept in dry Ar.

Although this project will mainly focus on synthesis, characterization and measurement of Cu_2O, an effort has been made to investigate another candidate to act as the photocathode, namely $CuFeO_2$. The motivation for this is the unstable nature of Cu_2O in PEC cell environments and finding stable substitutes are of great interest.

2 Theory

This chapter introduces the reader to most of the theory needed to understand this work, with focus on semiconductor theory and the semiconductor-electrolyte interface applicable for water-splitting and hydrogen evolution.

2.1 Understandig the Semiconductor

In the world of materials science, semiconductors have occupied the minds of researchers for centuries and the fascination continues to this day. According to Busch [10] the word semiconductor was first mentioned by Alessandro Volta *...in a paper read in English before the Royal Society in London on 14 March 1782*. Later, Michael Faraday would prove the semiconducting properties of materials by showing that increasing temperature could drastically increase the conductivity in certain materials; the reason for this will become apparent later in this section.

The photovoltaic (PV) effect, and subsequently photoelectrocemistry, was discovered only a few decades later in 1839 by Edmond Becquerel when he was able to detect a voltage between a solid material and a liquid electrolyte under illumination [11].

More modern contributions to the field of semiconductor electrochemistry include the mid-1950s work on the germanium/electrolyte interface by Brattain and Garrett and Letaw and Bardeen's work on the 'electrolytic analog transistor', marking the start of modern semiconductor electrochemistry according to Peter. [12]

2.1.1 Band Structure and Density of States

The basic idea of semiconductors can be explained by showing how atoms and their corresponding electron energies behave when bonding to other atoms, going from single atom electron energies through more complex *energy levels* in molecules to *energy bands* in solids as shown in figure 2.

figure 2: Bonds to bands schematics of a typical system when similar atoms bond to form a bulk material where electron energies overlap to form bands of allowed energies.

The allowed electron energy levels, or states, are grouped into bands, separated by forbidden energy gaps. Electrons in a material have a certain kinetic energy, and this energy determines what bands the electrons can fill. At 0 K, the highest filled energy bands is called the valence band, E_V. The lowest unfilled energy band at 0 K is called the conduction band, E_C. The semiconductor is by definition a material where these two bands are separated by a gap in allowed energies called the bandgap, $E_{gap} = E_C\text{-}E_V$.

The density of allowed states in the bands are typically intricate functions of energy and can be calculated by DFT to produce figures such as figure 3. In the inset of figure 3, an enlarged view of the bandgap region is depicted, showing no allowed states close to 0 eV. The VBM is typically set to 0 eV in plots like these
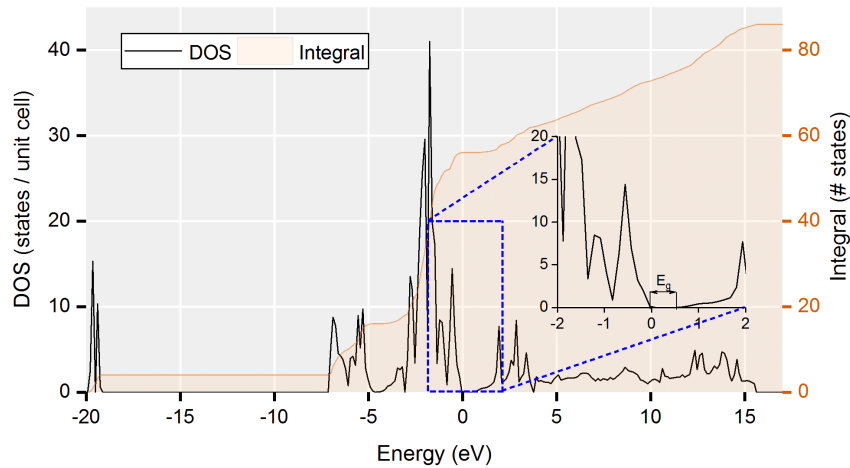

figure 3: Cu_2O DOS plot from DFT calculations conducted during this work. Inset shows details in DOS 2 eV above and below VBM, with no states just positive of VBM, indicating the bandgap.

to indicate the filled and unfilled bands below and above 0 eV, respectively, as this is the area of interest in semiconductor research. The CBM is located where the first indications of states appear[1].

By adding a reciprocal dimension to the system we gain even further insights into the material properties. This dimension is called k-space and is the reciprocal space of the structure. A plot of energy vs. **k** yields the band structure of the bulk material and can tell us a great deal about the material properties such as mobility and effective mass of charge carriers. Plotting E vs. **k** is done by choosing points of high symmetry in the reciprocal k-space. A depiction of where these high-symmetry points are located can be seen in figure 13 on page 21 and is typically denoted by capital greek letters as shown in figure 4. The center of k-space is usually given the letter Γ and marks the (000) 'plane' in the crystal.

All points on the lines connecting high-symmetry points in figure 4 are k-points in the reciprocal k-space of the structure. In the case of Cu_2O, figure 4 shows that the CBM and VBM are both located at Γ, meaning that Cu_2O is a *direct bandgap* material. If the CBM and VBM are located at different k-points, the material is an *indirect bandgap* material.

---

1   In this case the bandgap is greatly underestimated. This is a typical problem with DFT calculations
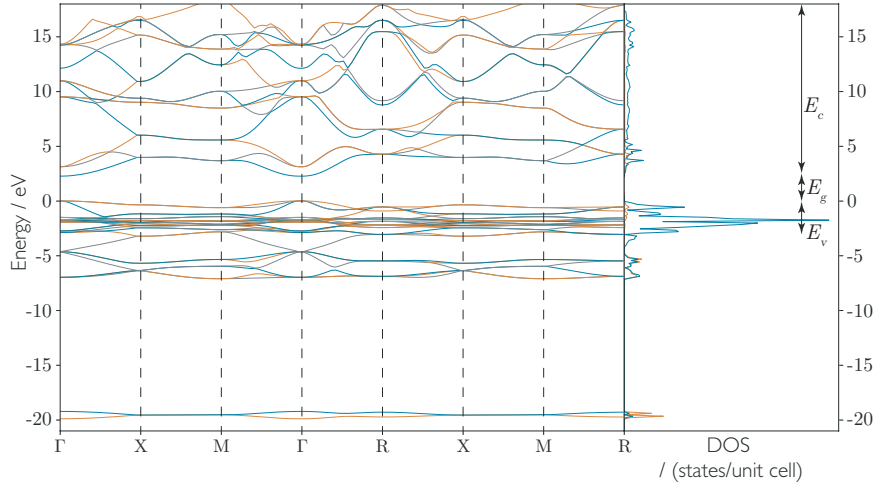
figure 4: Bandstructure of Cu_2O as calculated in this work.

Another way to describe k-space is that every k-point is explicitly described by a vector **k** that originates in Γ. These vectors are defined in one dimension as

$$k \equiv \frac{p}{\hbar} = \frac{\sqrt{2m_e E}}{\hbar} \tag{2.4}$$

where p is the momentum of the crystal structure, and m_e is the electron mass.

As can be seen in equation (2.4), **k** is directly related to the momentum of the crystal structure. Direct bandgap materials have the advantage that electron excitations from VBM to CBM do not include a change in crystal momentum, and as a result the light adsorption coefficients for direct bandgap materials are higher than for indirect bandgap materials. The momentum change needed in order to excite electrons in an indirect bandgap material can be provided by, e.g., phonon interactions (lattice vibrations), and results in lower adsorption coefficients, therefore the material has to be thicker in order to adsorb incoming photons.

$$m^* = \frac{h}{\left(\frac{\partial^2 E}{\partial k^2}\right)} \tag{2.5}$$

$$\mu = \frac{q\tau}{m^*} \tag{2.6}$$

Equation (2.5) and (2.6) show that both the effective mass, and the charge carrier mobility can be derived from the band structure. Equation (2.5) show that the effective mass of electrons are inversely proporsonal to the curvature of the bands. Equation (2.6) shows that the mobility of charge carriers are inversly proportional to the effective mass.

Studying a band diagram is therefore particularly useful when performing a quick qualitative analysis on the properties of any material. Photon adsorption coefficients, effective mass and mobility of charge carriers are all important parameters in deciding if a material can perform well under the conditions we want to impose on it. A great advantage is that this can be done theoretically by DFT even before any physical material is synthesized, avoiding unnecessary laborious trail-and-error lab work.

2.1.2   Fermi Level

The density of states available for electrons is just one part of the puzzle. It also needs to be considered what states are actually filled with electrons. At 0 K all states up to and including the VBM are filled, and all states above and including CBM are empty. The probability for an electron to occupy an energy level E is defined by the Fermi–Dirac function $f(E)$.

$$f(E) \ = \ \frac{1}{1 + \exp\left[\dfrac{E - E_\mathrm{F}}{k_\mathrm{B}T}\right]} \tag{2.7}$$

where E_F is the Fermi energy level, k_B is Boltzmann's constant and T is the temperature. This equation shows that if $E = E_\mathrm{F}$ the probability of finding an electron at an energy E_F is $1/2$. This is in fact one of the definitions of the Fermi energy level: the probability of having an electron occupy the energy level corresponding to the Fermi energy level is 50%. Another simplified way to explain the Fermi energy level is that the Fermi level equals the chemical potential of electrons in the solid at 0 K. In semiconductors, the Fermi level is located within the band gap, per definition. Hence, at 0 K all electrons are confined to the highest energy level below E_F, and all bands above E_F are consequently empty.

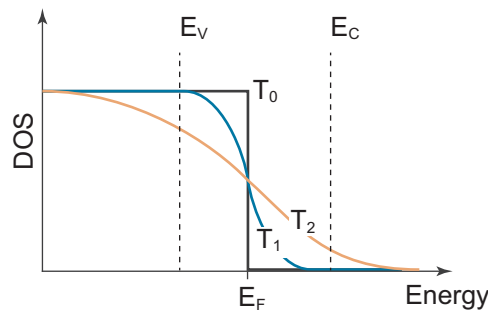However, the systems we look at gets much more interesting when the temperature is *not* zero. Equation (2.7) with varying temperatures is represented in figure 5 and shows that as the temperature increases, the density of available states shifts towards higher energies and thus higher energy states become available for the electrons; this is electrons gaining energy and, if the 'tail' of electron energies overlap with allowed energy states, *excitation* of electrons to higher empty energy states is possible. In practice, this means that electrons are able to make the jump from the valence band to the conduction band as long as the energy provided is sufficient. In figure 5, $f(E)$ overlaps with CB at T_2 but not at T_1, meaning that at T_1 no thermal excitation will take place. On the other hand, at T_2 the electrons have gained enough energy from the increased temperature that thermal excitation can take place over the bandgap. This is in fact the effect Michael Faraday discovered back in the 19th century.

figure 5: Representation of equation (2.7) at different temperatures where $T_0 = 0\ \mathrm{K} < T_1 < T_2$

When electrons make the jump from the valence band to the conduction band, electron vacancies, or *holes,* are left in the valence band. The concentration of electrons n and holes p can be calculated by

$$n_0 \ = \ n_i e^{(E_\mathrm{F} - E_i)/k_\mathrm{B}T} \tag{2.8}$$

$$p_0 \ = \ n_i e^{(E_\mathrm{F} - E_i)/k_\mathrm{B}T} \tag{2.9}$$

where the subscript 0 indicates equilibrium conditions. The equilibrium concentrations of electrons and holes are also related through the mass balance equation .

$$n_0 p_0 \; = \; n_i^2 \; = \; N_V N_C \exp\left[-\frac{E_{\text{gap}}}{k_B T}\right] \tag{2.10}$$

where N_V and N_C are the *effective* DOS in the VB and CB, respectively.

For intrinsic semiconductors where $N_V = N_C$ it follows that the Fermi level reside in the middle of the bandgap. In reality however, E_F is displaced slightly from the middle as the density of available states in the CB and VB is not equal, such as shown in, e.g., figure 3. [13]

Most materials, including semiconductors, are in practice extrinsic, meaning that the material is imperfect and contain impurities, either naturally or by design, and $N_V \neq N_C$. Typically, if the material are extrinsic by design, i.e., if we introduce impurities in the form of foreign atoms etc., the material is said to be *doped*. When doping a material with atoms capable of accepting electrons from the structure, the material is said to be acceptor doped. Doping a material with electron-acceptor or electron-donor atoms results in a shift of the Fermi-level either towards the valence band or towards the conduction band, making it either a *p-type* or *n-type* semiconductor, respectively, by introducing new allowed energy states within the bandgap. Even in undoped materials, *defects* are always present and function much the same way as when intentionally doped, introducing new energy states in the bandgap and act either as an acceptor or donor.

This shift of E_F leads to a change in conduction properties, making the material behave different from the intrinsic material. In n-type semiconductors, electrons are the major contributor to any electronic conductivity, whereas holes are the major contributor in a p-type semiconductor. These are often termed *majority carriers*, while holes and electrons are termed the *minority carrier*s in n- and p-type semiconductors, respectively.

Electrochemical potential

The electrochemical potential of a species i is a measure of how much the Gibbs energy of a system with an inner potential, ϕ, changes when the chemical species i is added to a system. The molar electrochemical potential is given as

$$\bar{\mu}_i \; = \; \mu_i + z_i F \phi \tag{2.11}$$

where μ_i is the molar chemical potential and $z_i F$ represents the electrical work done by one mole of charge, F being the Faraday constant. ϕ is the work function; the absolute chemical potential of the electrons, μ_n. The chemical potential of electrons and holes depends on their concentration. By changing the molar concentrations to number densities it is possible to express the chemical potentials per electron or hole [12]

$$\mu_n \; = \; \mu_n^0 + k_B T \ln \frac{n}{N_C} \qquad \text{and} \qquad \mu_p \; = \; \mu_p^0 + k_B T \ln \frac{p}{N_V} \tag{2.12}$$

where μ^0_n and μ^0_p are the standard chemical potentials of holes and electrons, respectively. Würfel and Würfel [14] also show that the electrochemical potentials of holes and electrons are in fact equal to the Fermi energy level.

$$\bar{\mu}_n = E_\mathrm{F} \quad \text{and} \quad \bar{\mu}_p = -E_\mathrm{F} \tag{2.13}$$

2.2 The illuminated Semiconductor

As light interacts with a semiconducting material, incident photons provide energy to electrons in much the same way as temperature does, enabling electron excitation from the valence band to the conduction band. Under photostationary conditions, the excitation of electron-hole pairs is balanced by their recombination and $\Delta n = \Delta p$.

The recombination process is an important bulk property and determines the *minority carrier lifetime*, τ_{min}, typically ranging from 10^{-3} s to 10^{-9} s for ultra-pure silicon and compound semiconductors, respectively. If τ_{min} is long enough, minority carriers can diffuse to the surface and recombine via surface states if the minority carrier diffusion length

$$L_\mathrm{min} = \sqrt{D_\mathrm{min}\tau_\mathrm{min}} \tag{2.14}$$

is equal or greater than the sample thickness. Here D_min is the diffusion coefficient of minority carriers. Surface recombination can be described by a surface recombination velocity

$$v_\mathrm{sr} = v_\mathrm{th}\sigma N_\mathrm{ss} \tag{2.15}$$

where v_th is the thermal velocity of electrons and hole, σ and N_ss is the capture cross section and number of surface states, respectively. This mechanism is especially important in photocatalysis using photoelectrodes as the surface recombination competes with interfacial electron transfer, lowering the quantum efficiency of processes such as light-driven water splitting and hydrogen production.

If we want to look at the concentrations of electrons and holes in the semiconductor, neglecting surface recombination, these concentrations are determined only by the generation rate G and the bulk minority carrier lifetime. In a p-type semiconductor under steady state illumination, the excess electron concentration Δn is described by

$$\frac{\mathrm{d}\Delta n}{\mathrm{d}t} = G - \frac{\Delta n}{\tau_\mathrm{n}} = 0 \tag{2.16}$$

so that

$$\Delta p = \Delta n = G\tau_\mathrm{n} \tag{2.17}$$

Illuminating a semiconductors will perturb the equilibrium of the system. The kinetics of the processes needed to restore equilibrium describes the time needed to achieve this. This restoring process occurs both

within in the bands, and between the bands. Within the bands, local equilibrium is reached within ~10^{-12} s by phonon scattering. Restoring equilibrium between the bands by electron-hole recombination takes a few multiples of the carrier lifetime, i.e., at least nanoseconds. Since recombination takes so much longer, one Fermi-Dirac function can no longer describe the distribution of electrons and holes. Instead, we use two Fermi-Dirac functions to describe the effective electron and hole carrier concentrations, one for electrons and one for holes, defined by unique quasi-Fermi level energy (QFL).

$$n + \Delta n = N_C \exp\left(-\frac{E_C - E_{Fn}}{k_B T}\right) \quad \text{and} \quad p + \Delta p = N_V \exp\left(-\frac{E_{Fp} - E_V}{k_B T}\right) \tag{2.18}$$

where E_{Fn} and E_{Fh} is the Fermi level of electrons and holes, respectively.

The free energy of electron-hole pairs is the sum of the electrochemical potentials, but as the electrical charge of electron and holes cancels out, the energy of electron-hole pairs is the sum of their chemical potentials, and according to equation (2.13): the difference in QFL.

$$\mu_{eh} = \mu_n + \mu_h = E_{Fn} - E_{Fp} \tag{2.19}$$

Utilizing the largest possible fraction of this chemical potential is the goal of any energy converting semiconductor device.

2.3   Junctions

When the semiconductor surface comes in contact with another material (e.g., a metal or another semiconductor) or phase (e.g., electrolyte) the junction that emerges accounts for many of the effects we utilize in materials science. This junction is the reason for the current flowing in solar-cells, transistors' ability to turn on and off, and why some semiconductors can split water and make hydrogen.

When these materials (or phases) first make contact, the two sides need to equilibrate, which means that the Fermi levels must align. By transfering mobile charges to achieve equilibrium, a region appears that differs from the bulk composition on either side. In this *space charge region*, mobile charges are depleted or accumulated as they go across, or to, the interface to compensate and equilibrate, respectively. The imbalance in charge neutrality leads to band bending in the depletion region. The concentration of mobile charge carriers and the necessitous charge compensation determine the width of this region.

Shown in figure 6 to illustrate this region is an n-type semiconductor put in contact with a metal with a higher work-function. Electrons migrate from the semiconductor to the metal and Fermi-levels align, generating a potential difference that establishes electronic equilibrium. This potential difference is the *built-in voltage*, V_{bi}, of the junction and is the difference in work-functions of the two materials. In turn, the potential difference produces a region of positive charge near the semiconductor surface in the form of ionized donors, and the bands bend as a result of this. Even though the electrical potential across the junction varies with distance, the electrochemical potential is constant due to the variations in electron densities
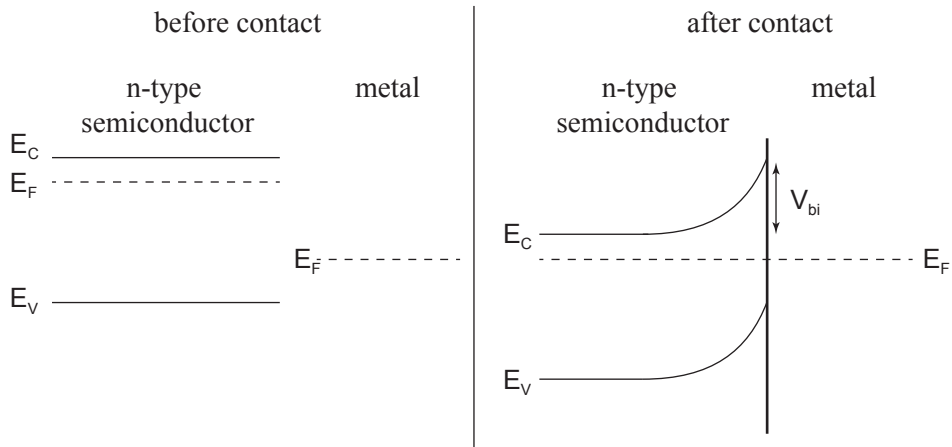
figure 6: Schematics of a semiconductor-metal junction before (left) and after contact (right).

over the same distance, indicated by the constant Fermi-level.

2.3.1 Semiconductor Electrolyte interface

A semiconductor in contact with an electrolyte acts much the same way as it would when in contact with metal. However, the electrolyte is not electronically conducting per se, but ions close to the semiconductor surface can accept electrons or holes through redox reactions. Thus, electric current flows over the junction until the Fermi-level of the semiconductor equals the redox potential of the electrolyte, E_{redox}, setting up a space charge layer on each side of the interface. In the semiconductor, this bends the bands as previously discussed. In the electrolyte, however, an electrolytic double layer forms: closest to the interface is the Helmholtz layer, followed by the Gouy- Chapman region as illustrated in figure 7.
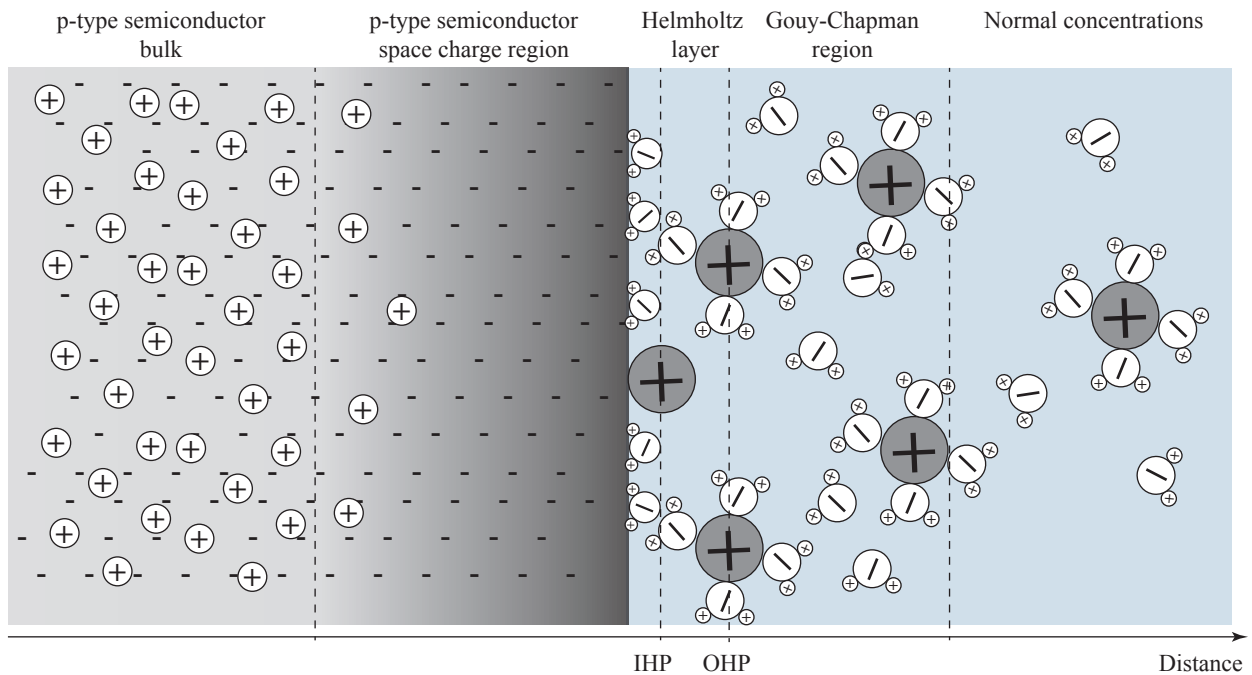

figure 7: Schematics showing the double layer at the surface of a p-type semiconductor in contact with an electrolyte with solved cations. It shows the inner and outer Helmholtz plane (i.e., IHP and OHP, respectively) making up the Helmholtz layer, and the Gouy-Chapman region, starting at the OHP and ending where bulk electrolyte concentrations appear.

Double Layer

Closest to the electrode surface in the electrolytic double layer is the inner Helmholtz plane (IHP), defined by the radius of the *specifically adsorbed species* on the electrode surface (i.e., a molecule or ion. In the case of figure 7: a cation). Solvated ions can approach the electrode only to a specific distance defined by the outer Helmholtz plane (OHP), and the IHP to the OHP together defines the Helmholtz layer. The Gouy-Chapman region starts at the OHP; a region where charged species experience long-range electronic interactions from the semiconductor surface, and as a result, showing a higher concentration of charged species than in the bulk electrolyte. [15]

Band Position and Bending

The nature of the band bending in the semiconductor depend on the position of the Fermi-level in the solid and the redox potential of the electrolyte. If the Fermi-level of the electrode is equal to the redox potential in the electrolyte, no band bending occurs. However, if the Fermi level does not align with E_{redox}, mobile charges must migrate either to the surface or electrolyte to compensate. If mobile charge carriers accumulate on the semiconductor side, accumulation occurs. However, if these charge carriers migrate from the solid into the electrolyte, a depletion layer forms. Depletion may also reach a state of inversion, i.e., the surface of a p-type semiconductor effectively becomes n-type as the hole concentrations fall below the intrinsic level. [16] The different situations are shown in figure 8.
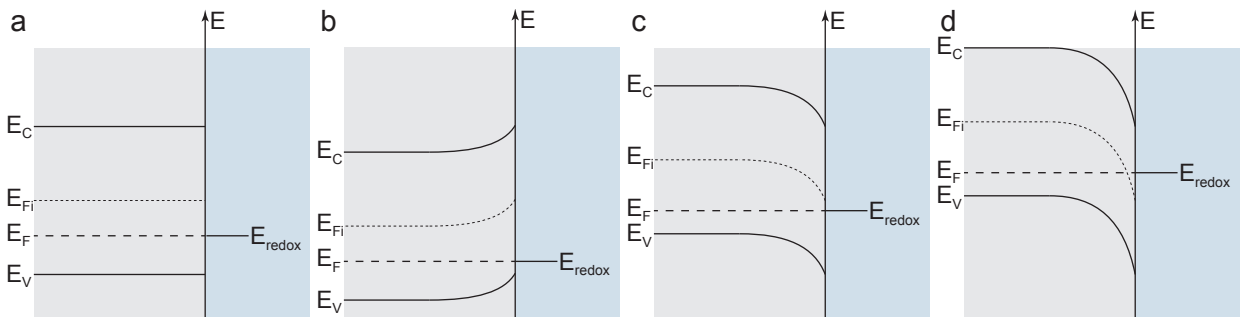

figure 8: Band bending schematics of a p-type semiconductor in contact with an electrolyte containing a redox couple with a redox potential of E_{redox}. The four instances shown are flat-band potential (a), accumulation of holes (b), depletion of holes (c) and surface inversion (d).

2.3.2 Applied Voltage

As mentioned in section 2.3, all junctions have a built-in voltage, and this applies to the semiconductor-electrolyte junction as well (as long as $E_F \neq E_{\text{redox}}$). However, by applying an external voltage and hence shifting the Fermi-level of the semiconductor, the bands can be manipulated further. Finding the flat-band potential (figure 9) is a particularly useful quantity in photoelectrochemistry from which we can locate the energetic position of the valence band and conduction band. Running electrochemical impedance spectroscopy with subsequent application of the Mott-Schottky equation accomplishes this. [17]
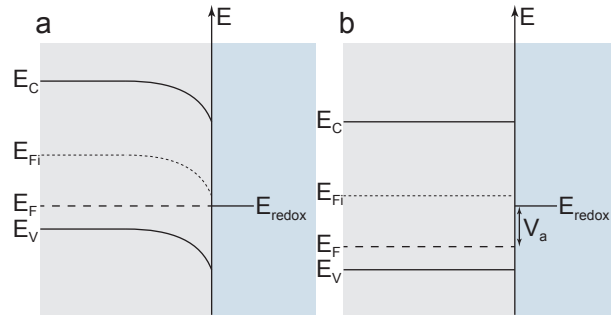
figure 9: A voltage $|V_a| = |V_{bi}|$ is applied to the semiconductor to achieve flat bands.

Applying a voltage will also shift the chemical potential of charge carriers in the semiconductor, along with the shift in Fermi-level. This shift may facilitate increased charge transfer over the interface if the voltage applied is such that the band bending reduces; the opposite is true if applied voltage increase band bending. Assuming an equilibrium can be reached, this charge transfer only takes place to reestablish equilibrium and reconfigure the space charge region. In the dark (at equilibrium), there is no driving force separating thermally generated electrons and holes, and no oxidation or reduction of electrolyte species occur. However, if the voltage applied is such that the redox species consume electrons or holes provided by the solid through a reduction or oxidation process, the interface will not reach equilibrium, and the redox process continues. This mechanism also applies to conductors in general and is in fact how water electrolysis works. Immerse two conductors in a glass of water and connect them to a power source of at least 1.23 V and electrolysis takes place (i.e., in an ideal case. An overpotential is probably needed to overcome contact resistances, double layer capacitance, etc.)

2.4 Photoelectrocatalysis

Even if there can be no oxidation or reduction of species in the dark at equilibrium, illumination of the semiconductor will change this. As earlier stated, steady illumination of a semiconductor perturbs equilibrium, splitting the Fermi-level into QFLs. Besides, it induces an internal photovoltage, V_{ph}, in the solid, a voltage that increases the chemical potential of majority charge carriers by a shift in majority carrier Fermi-level. If we picture a p-type semiconductor under illumination, bulk Fermi-level $E_F = E_{Fp}$ while E_{Fn} will shift to higher energies as the electrons concentration increase a lot more than the holes concentration as shown in figure 10.

A driving force to separate electrons and holes are present in the space charge region at steady state illumination, and for a p-type semiconductor, electrons goes to the electrolyte and holes towards bulk. If the location of CBM sits above a species reduction potential (e.g., H^+ to $H_2(g)$) the photogenerated electrons facilitate this reduction (i.e., assuming ideal conditions).

Analogous considerations apply for n-type semiconductors; electrons are the mobile charge carriers and the immobile positively charged states of the donor dopant form the excess space charge within the deple-

tion layer. Photoexcitation produces holes that are driven to the interface and can oxidize a chemical species with a higher oxidation potential than VBM.
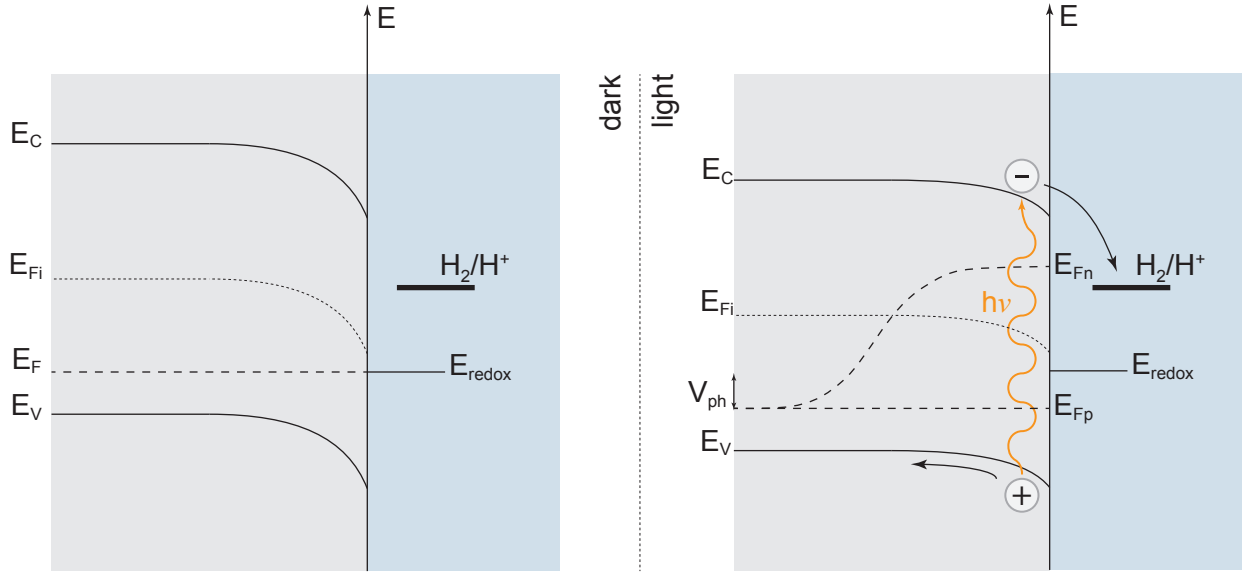

figure 10: Schematics showing a p-type semiconductor in contact with an electrolyte with redox potential E_{redox} in the dark (left) and the same semiconductor during steady state illumination with quasi Fermi-levels and photoexcitation (right). The photovoltage is indicated by V_{ph}.

Semiconductors acting as electrodes in photocatalytic cells are called *photocathodes* and *photoanodes* for p- and n-type, respectively, since p-type semiconductors provide electrons to the electrolyte for reduction and n-type semiconductors offer holes for oxidation. Thus, to identify appropriate materials for, e.g., water splitting, looking at the materials band structure and the energetic location of VMB and CBM provides valuable information.

2.4.1   Photocorrosion

Even if a material has perfect band alignment for redox applications, many materials have corrosion issues, especially oxides. The problem is that the photoexcited electron-hole pair can reduce or oxidize the material itself if the decomposition potentials fall within the range of the chemical potential of electrons and holes. For a p-type metal oxide semiconductor under illumination, a cathodic reaction can occur, reducing the material with subsequent metal deposition

$$M_xO_x(s) + 2y\ e^- + 2y\ H^+(aq) \rightarrow xM(s) + yH_2O(l) \tag{2.20}$$

Similarly, n-type semiconductors can experience anodic decomposition

$$M_xO_x(s) + \frac{2y}{x}\ h^+ \rightarrow xM^{\left(\frac{2y}{x}\right)+}(aq) + \frac{y}{2}\ O_2(g) \tag{2.21}$$

The Gibbs free energy determines the rate at which the material reduces or oxidizes. If the equilibrium potentials for these reactions, $V_{\text{p,d}}$ and $V_{\text{n,d}}$ (i.e., anodic and cathodic decomposition, respectively), is within

the bandgap, anodic or cathodic photocorrosion may occur. Figure 11 presents a selection of semiconductors with favorable band alignment for water-splitting and hydrog en production with, $V_{n,d}$ and $V_{p,d}$ given. Using Cu_2O as an example, both the cathodic and the anodic photocorrosion potentials lay within the bandgap, and thus cuprous oxide will photocorrode under illumination in aqueous solution. Yet, most materials are resistant to cathodic photocorrosion as figure 11 shows, although not so much anodic photocorrosion.
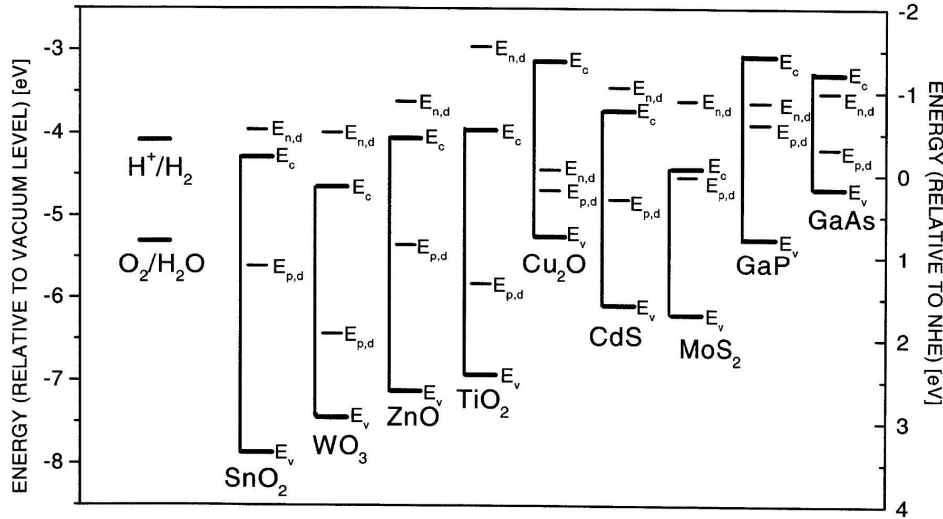

figure 11: A selection of cathodic and anodic photocorrosion reaction potentials ($E_{n,d}$ ($=V_{n,d}$) and $E_{p,d}$ (= $V_{p,d}$), respectively) for a range of semiconductors with otherwise auspicious band positioning. [18]

TiO_2 is an example of the latter, i.e., the anodic photocorrosion potential lies just below the center of the bandgap, and one would expect that TiO_2 is highly prone to corrosion. This is not the fact however. TiO_2 is a very stable photoanode material in PEC operations, and the reason for not corroding is slow kinetics. This means that even if the corrosion potentials lie within the bandgap of a material, it does not necessarily mean that the material will corrode. Hence, experimental work has to compliment theoretical work to conclude if corrosion occurs or not.

2.5 Quantum mechanical modeling

Modeling of complex structures and systems has become more readily accessible in recent decades as the computational power of the world has increased at an incredible rate. Also, a lot of effort has been made to optimize these calculations and materials scientists today are preforming calculations on large systems with complex structural interactions with high accuracy. The results of these calculations are sometimes impossible to obtain from experimental data and often provide valuable information.

This section is to a large extent adopted and modified from the comprehensive book on density functional theory by Sholl et al. [19]

2.5.1   Many Particle Schrödinger Equation

One of the fundamental things we want to solve is the energy of atoms and *the change in energy* as we move them around. The many particle Schrödinger equation (SE) can, in theory, be used to describe such a system with interacting atoms. The simplest form of the time independent, nonrelativistic SE in

$$\hat{H}\psi \;=\; E\psi \tag{2.22}$$

where $\hat{H}$ is the Hamiltonian operator and is ψ a set of eigenstates of the Hamiltonian, all with an associated eigenvalue E; a real number satisfying the eigenvalue equation.

For the situation of interest to us, a many-particle system, we need to apply a Hamiltonian to tackle all these interactions. SE would the be

$$\left[\frac{h^2}{2m} \sum_{i=1}^{N} \nabla_i^2 \;+\; \sum_{i=1}^{N} V(\mathbf{r}_i) \;+\; \sum_{i=1}^{N} \sum_{j<1} U(\mathbf{r}_i, \mathbf{r}_i) \right] \psi = E\psi \tag{2.23}$$

m being the electron mass, h Planck's constant[2] and N the number of atoms in the system. The sums represent the kinetic energy of electrons, interaction energy between electron i and the nuclei, and the electron-electron interaction, respectively. The energy E in equation (2.22) is the ground state energy of the electrons.

Electron wave functions in systems like these interact, but to such small extent that approximating the total wave function ψ to a product of individual electron wave functions are possible

$$\psi \;=\; \psi_1(\mathbf{r})\psi_2(\mathbf{r})\psi_3(\mathbf{r}) \dots \psi_N(\mathbf{r}) \tag{2.24}$$

Expressing the wave function like this is known as a Hatree product, but as shown in equation (2.23), the electron-electron interaction is crucial to solving SE, so solving SE by using the Hartree product approach means solving every electron wave function with respect to all the others, a job requiring massive computational power.

Further, the density of electrons at any point in space can be expressed by means of the individual electron wave function, $\psi_i(\mathbf{r})$, through

$$n(\mathbf{r}) \;=\; 2 \sum_i \psi_i^*(\mathbf{r})\psi_i(\mathbf{r}) \tag{2.25}$$

such that the term inside the summation is the probability that an electron with corresponding wave function $\psi_i(\mathbf{r})$ is located at $\mathbf{r}$; the factor of 2 accounting for Paulis exclusion principle, allowing two electrons of different spin to occupy the same wave function. The fact that the electron density $n(\mathbf{r})$ at any point is a function of only three coordinates will prove extremely useful in calculations of atom stuctures utilizing SE; henceforth known as *density functional theory*.

---

2        $h = 6.62 \cdot 10^{-34}$ Js

2.5.2   Density Functional Theory

The field of density functional theory (DFT) is basically founded on two mathematical theorems by Kohn and Hohenberg [20], and the Kohn-Sham equation [21]. The first theorem states that *the ground-state energy from SE is a unique functional of the electron density*; there is a one-to-one mapping between the wave function of the ground state and electron density in this state. This means that the ground state energy E can be expressed explicitly by the functional

$$E\left[n(\mathbf{r})\right] \tag{2.26}$$

where $n(\mathbf{r})$ is the electron density, hence **density functional theory**.

In practice this means that solving SE is possible by finding a function of three variables rather than $3N$ variables, since the ground state electron density uniquely determine all properties, including the energy and wave function. The problem with this theorem is that although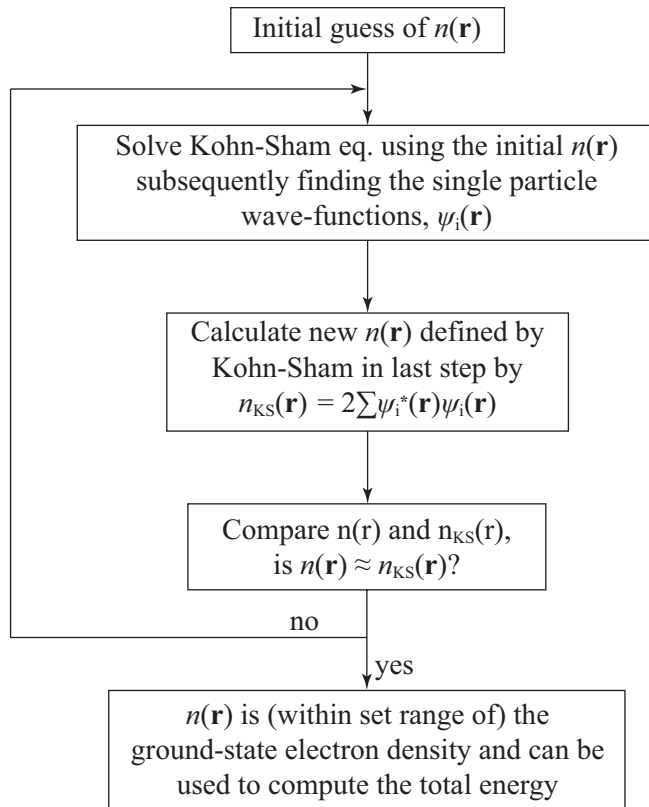 it states that a functional like this exist, it does not declare what this functional is, although an important property of this functional is defined in the second Hohenberg-Kohn theorem: *The electron density that minimizes the energy of the overall functional is the true electron density corresponding to the full solution of SE*, meaning that if the 'correct' functional were known, varying the electron density and subsequently finding an energetic minimum in the system would yield the relevant electron density; this *variation principle* is what is practically implemented in computational functional calculations such as PBE, PBE0, HSE06 etc.

Using the property that the electron density, $n(\mathbf{r})$, are defined by the single-electron wave functions from, as of equation (2.25), the Hohenberg-Kohn theroem can be written as

$$E\left[\{\psi_i\}\right] = E_{\text{known}}\left[\{\psi_i\}\right] + E_{\text{XC}}\left[\{\psi_i\}\right] \tag{2.27}$$

figure 12: Schematics of the circular Kohn-Sham argument.

The flowchart reads:

Initial guess of $n(\mathbf{r})$

Solve Kohn-Sham eq. using the initial $n(\mathbf{r})$ subsequently finding the single particle wave-functions, $\psi_i(\mathbf{r})$

Calculate new $n(\mathbf{r})$ defined by Kohn-Sham in last step by $n_{\text{KS}}(\mathbf{r}) = 2\sum\psi_i^*(\mathbf{r})\psi_i(\mathbf{r})$

Compare n(r) and n_{KS}(r), is $n(\mathbf{r}) \approx n_{\text{KS}}(\mathbf{r})$?   no

yes

$n(\mathbf{r})$ is (within set range of) the ground-state electron density and can be used to compute the total energy

splitting the functional into two parts: one known and one collecting everything unknown, E_{XC}. The known terms have four contributions

$$E_{\text{known}}\left[\{\psi_i\}\right] \;=\; \frac{h^2}{m} \sum_i \int \psi_i^* \nabla^2 \psi_i \, \mathrm{d}^3 r \;+\; \int V(\mathbf{r}) n(\mathbf{r}) \, \mathrm{d}^3 r$$
$$+\; \frac{e^2}{2} \iint \frac{n(\mathbf{r})n(\mathbf{r}')}{|\mathbf{r} - \mathbf{r}'|} \, \mathrm{d}^3 r \, \mathrm{d}^3 r' + E_{\text{ion}} \tag{2.28}$$

while the unknown term, E_{XC}, is called the exchange-correlation functional and include all the quantum mechanical effects left out in E_{known}. The complexity of the calculations are at this point not guaranteed to be simpler than solving the full SE, but this changes when including the Kohn-Sham equation:

$$\left[\frac{h^2}{2m}\nabla^2 \;+\; V(\mathbf{r}) \;+\; V_{\text{H}}(\mathbf{r}) + V_{\text{XC}}(\mathbf{r})\right] \psi_i(\mathbf{r}) \;=\; \varepsilon_i \psi_i(\mathbf{r}) \tag{2.29}$$

where the correct electron density is found by a set of equations, each equation involving only one electron. The Kohn-Sham equation itself is somewhat similar to equation (2.23) but is missing the summations as this is in fact single electron wave functions only dependent on $\psi_i(\mathbf{r})$. The three potentials V, V_{H} and V_{XC} is the potential defined by electron and nuclei; the Hartree potential.

As shown in figure 12 this becomes a circular argument using an initial guess of the electron density $n(\mathbf{r})$ and its associated energy to find the electron 'ground' state, or at least something very close, by adjusting $n(\mathbf{r})$ for each iteration minimizing energy.

2.5.3   Exchange-Correlation Approximations

No matter how elegant and beautiful the results of Kohn, Sham and Hohenberg may be, one important parameter remains to be decided; namely the exchange–correlation function $E_{\text{XC}}[\{\psi_i\}]$. This is not an easy task, and although the Hohenberg-Khon theorem states that there is in fact an exchange–correlation function, it is not readily found. However, in one special case this function is known, namely for a uniform electron gas where the electron density is constant at all points in space; that is $\mathrm{d}n(\mathbf{r})/\mathrm{d}\mathbf{r} = 0$, and provides a practical way to use the Kohn-Sham equations. To do this the exchange-correlation potential at each position is set to the known exchange–correlation potential from the uniform electron gas at the electron density observed at that position

$$V_{\text{XC}}(\mathbf{r}) \;=\; V_{\text{XC}}^{\text{electron gas}}\left[n(\mathbf{r})\right] \tag{2.30}$$

This approximation is known as the *local density approximation* (LDA) as it uses only the local density to define the approximate exchange-correlation; this does completely define the Kohn-Sham equation but not necessarily SE as this is not the exact exchange-correlation functional.

As time has progressed new exchange-correlation functionals has been established in an effort to more closely resemble physical properties of structures, and after LDA the best known class of functionals are those using the local density of electrons as well as the local gradient in the electron density; the *generalized*

gradient approximation (GGA). Several widely used functionals are using GGA such as the Perdew-Wang functional (PW91) [22] and the Perdew-Burke-Emzerhof functional (PBE) [23], often providing results closer to experimental values than LDA, although this is not always the case.

2.5.4 Hybrid Functionals

The efforts to increase the accuracy of electronic structure calculations are ever going and in addition to LDA and GGA, there is also a group of exchange-correlation functionals that in essence mix other functionals to try and bring the strengths of other functionals together to better represent specific systems. One example of this is the PBE0 functional

$$E_{XC}^{PBE0} = \frac{1}{4}E_X^{HF} + \frac{3}{4}E_X^{PBE0} + E_C^{PBE} \tag{2.31}$$

utilizing the Hartree-Fock exchange functional, the PBE functional and the PBE correlation functional, respectively, with mixing coefficients determined by perturbation theory [24]. Another important hybrid functional is the HSE functional where the authors *...propose to apply a screened Coulomb potential only to the exchange interaction in order to screen the long-range part of the HF exchange}* [25].

$$E_{XC}^{\omega PBEh} = aE_X^{HF,SR}(\omega) + (1-a)E_X^{PBE,SR}(\omega) + E_X^{PBE,LR}(\omega) + E_C^{PBE} \tag{2.32}$$

where a is the mixing parameter and ω is an adjustable parameter governing the extent of short-range interactions. SR and LR denote the short range and long range components of the HF and PBE functionals, respectively. Assigning standard values $a = 1/4$ and $\omega = 0.2$ provides the functional often referred to as the HSE06 hybrid functional. It is also observed that $\omega = 0$ results in the PBE0 functional; $\omega \to \infty$ asymptotically reaches the PBE functional.

3 Literature

This chapter is devoted to a review of relevant literature for this thesis. It includes literature on the materials used in this work, along with relevant publications and reviews on photoelectrochemical systems for water-splitting and a short review of *ab initio* calculations performed on Cu_2O. Lastly, a summary with a brief discussion of the reviewed literature is included.
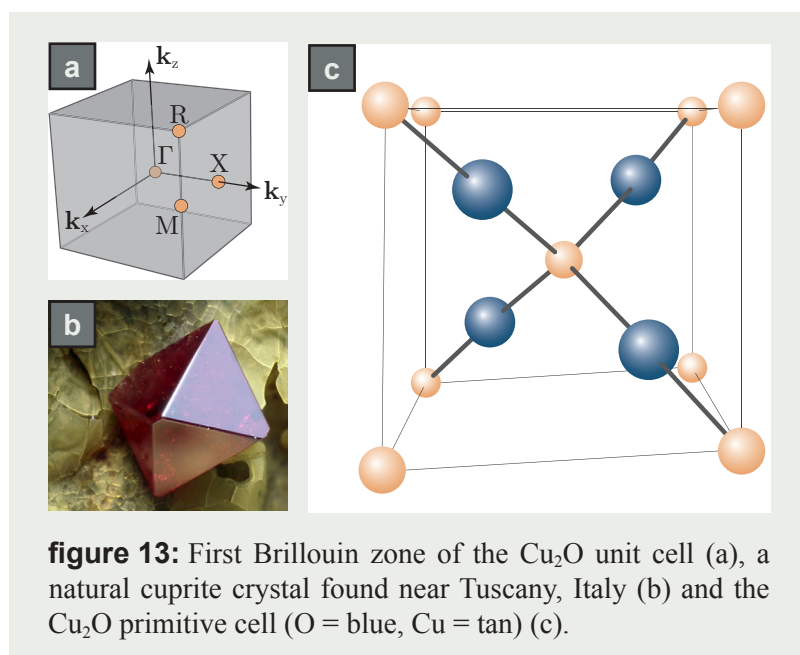
3.1 Cuprous Oxide

The first known description of cuprous oxide comes with a patent filed in august 1925 by a man of Norwegian ancestry, namely Lars O. Grondahl [26]. The discovery of cuprous oxide as a rectifying device was published in Science the subsequent year and marks the beginning of current semiconductor electronics [27]. Although it never gained much interest back then, there has been renewed interest on cuprous oxide in the last two decades in solar-cell applications, and more recently in photocatalytical water splitting applications. Much of this interest is due to its abundance and low cost, as well as the non-toxic nature of Cu_2O and high theoretical efficiency for solar-to-hydrogen (STH) conversions.

3.1.1 Physics of Cu_2O

Cu_2O is a stable oxide crystallizing in a simple cubic Bravais lattice (*Pn-3m* space group). The unit cell contains six atoms: four copper atoms positioned in a face-centered cubic lattice and two oxygen atoms at tetrahedral sites forming a body-centered cubic sublattice as shown in figure 13.

Natural crystals of Cu_2O can be found worldwide, although they usually contain high levels of defects and are generally of low quality. Synthetic crystals of Cu_2O can be prepared by a range of methods such as oxidizing copper sheets, melt growth, floating zone growth and by hydrothermal growth [28]. Thin films of Cu_2O can be grown by methods such as electrodeposition [6][29][30][31] and sputtering [32][33][34][35], using a wide variety of substrates such as fluorine-doped tin oxide (FTO), TiN, glass etc.

figure 13: First Brillouin zone of the Cu_2O unit cell (a), a natural cuprite crystal found near Tuscany, Italy (b) and the Cu_2O primitive cell (O = blue, Cu = tan) (c).

Epitaxial growth of cubic Cu_2O is possible by, e.g., molecular beam epitaxy [36][37], pulsed laser deposition [38][39] etc. and a MgO substrate is often the preferred choice as both possess cubic unit cells with comparable lattice parameters; $a(MgO) = 4.213$ Å and $a(Cu_2O)=4.269$ Å. Other substrates on which epitaxial growth of cubic Cu_2O has been shown include Si and Y-ZrO_2.

Cu_2O is a p-type semiconductor due to an acceptor level at 0.4 eV above the VBM that emerge as result of Cu vacancies in the structure, and the electrical properties are known to depend strongly on the preparation method. [41] For example, hole density is typically in the 10^{14} cm^{-3} range for electrodeposited samples, 10^{16} cm^{-3} when obtained by sputtering and 10^{20} cm^{-3} when produced by thermal oxidation. The drawback with thermal oxidation is that it is difficult to scale up, as well as the relative high energy cost, compared to, e.g., electrodeposition. Scaling is also an issue with sputtering, hence electrodeposition is preferred with large scale application in mind.

Cu_2O has a bandgap of ~2.1 eV and the VBM is located at 1.3 V vs. SHE (-5.74 eV vs. vacuum). This places the VBM 0.07 V below water reduction potential. The CBM is located at -0.7 V vs. SHE as shown in figure 14, making it highly attractive as a photocathode material for HER, as discussed further in section 3.3.3 on page 30.
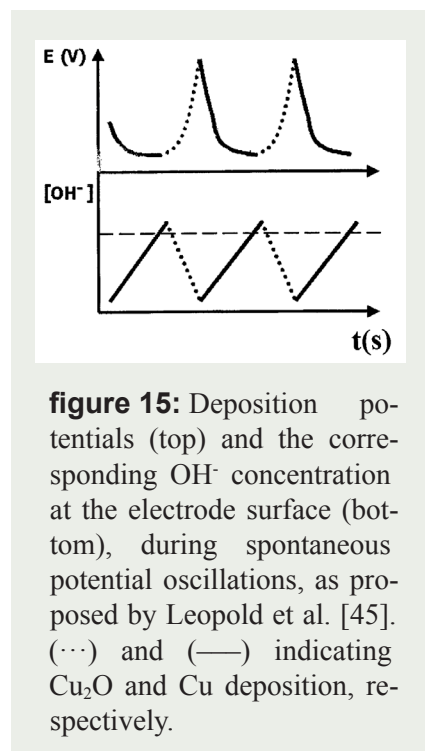
table 1: Properties of Cu_2O [40]

lattice constant	4.2696 Å
space group	Pn-3m (224)
bond length Cu-O	1,849 Å
separation O-O	3,68 Å
separation Cu-Cu	3,012 Å
cell volume	77.833 ± 0.055 ×10^{-24} cm^{-3}
formula weight	143.14 g mol^{-1}
density	5.749 - 6.140 g cm^{-3}
melting point	1235.0
thermal expansion coefficient	2.3*10-7 K^{-1} (238 K)
band gap	2.1 eV
electron affinity χ	3.1 eV
work function Φ	4.84 eV

figure 14: Band comparison of three photoactive materials used in this work.

3.1.2 Electrodeposition

After Stareck [42] introduced the idea of electrodepositing Cu_2O in 1943, the technique has been widely used due to its simplicity, low cost, low operating temperatures and ease of scalability. Along with a high level of deposition parameter control, depositing highly pure Cu_2O is possible. Also, the ability to tailor electrical properties through optimization of morphology and crystal structure by deposition parameters is yet another attractive feature of electrodeposition.

Electrodeposition of Cu_2O is usually done either galva-

nostatically or potentiostatically; that is, having a fixed current or fixed potential between the electrodes, respectively. Both these methods of deposition have their advantages and both are described in literature as being advantageous to the other. Rakhshani et al. [29] finds that thicker films can be produced potentiostatically, but that these films do not follow a linear growth rate, but rather a slight decrease in growth rate over time. Galvanostatic deposition follows a linear growth rate; a feature Paracchino et al. [6] claims to be ...*advantageous from a processing perspective because the film deposition rate can be precisely controlled*.

figure 15: Deposition potentials (top) and the corresponding OH⁻ concentration at the electrode surface (bottom), during spontaneous potential oscillations, as proposed by Leopold et al. [45]. (···) and (——) indicating Cu_2O and Cu deposition, respectively.

On the other hand, Yang [43] claims in his thesis that *Galvanostatic deposition is found to be less suitable than potentiostatic deposition for solar cell fabrication due to the difficulty in controlling Cu metal content in the film*, and even though this is stated with PV applications in mind, it would be highly relevant to photocatalysis application, as metallic Cu would negatively affect the catalytic properties.

A typical effect of galvanostatic deposition is in fact a self-assembly of Cu/Cu_2O layered nanostructures, indicated by *spontaneous potential oscillations* during deposition. This self-assembly is highly dependent on pH, Cu^{2+} concentration, and temperature in the deposition electrolyte. [44] Leopold et al. [45] propose that the mechanism of the oscillations depend on the concentration of

OH⁻ (i.e., pH) at the electrode surface, and that the subsequent shift in pH dictates a change in deposited species as illustrated in figure 15. To avoid this, Paracchino et al. [6] points to relatively low deposition currents to account for this, showing high quality Cu_2O deposited galvanostatically at a constant current of 0.1 mA cm⁻².

The mechanism proposed for the deposition of Cu_2O from a lactate stabilized copper sulphate plating bath such as the route described by Parracchino et al., is that Cu^{2+} ions, usually forming insoluble $Cu(OH)_2$ at high pH, is stabilized by the lactic acid forming Cu*Lac*$_2$ and remain soluble as KOH is added to raise the pH to 12 where deposition is carried out. The subsequent electrochemical reduction of Cu^{2+} to Cu_2O involves the formation and dehydration of a CuOH intermediate as shown through reaction (3.33) and (3.34). An interpretation of the mechanism is proposed in figure 16.
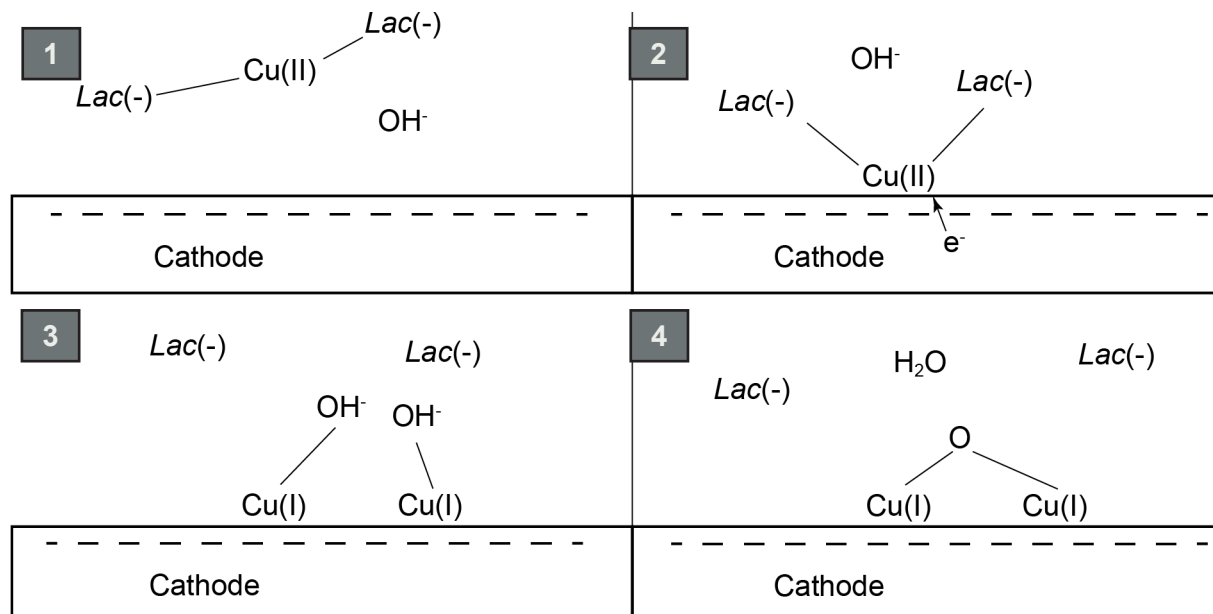
$$Cu\textit{Lac}_2 + OH^- + e^- \rightarrow CuOH + 2\textit{Lac}^- \qquad (3.33)$$

$$2CuOH \rightarrow Cu_2O + H_2O \qquad (3.34)$$
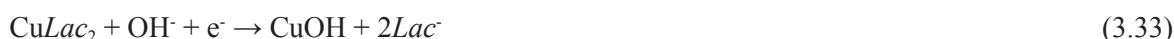
figure 16: A proposed reaction mechanism for the formation and dehydration of the CuOH intermediate and subsequent formation of Cu_2O during cathodic deposition.

3.1.3   Morphologies

There are numerous investigations into different morphologies obtained by varying electrodeposition parameters such as temperature, pH, concentrations etc. Yang [43] thoroughly investigates the subject and reports *a range of Cu_2O morphologies including cubic, octahedral, truncated and irregular polyhedral shapes, branched particles, as well as reformed shapes due to dissolution can be formed depending on the deposition conditions*. Yang ascribe the variations in morphologies to the relative growth rates of <111> and <100> orientations, and conclude that <100> predominates under reaction limited conditions, while <111> growth predominates in a system limited by mass transport. Specifically, it is showed that morphologies shift from octahedral to cubic as the overpotential (or current) is increased, while grains become more irregular without a clear orientation as temperature is increased. As pH is increased from 9.5 to 12.5 <111>-oriented growth becomes increasingly dominant over <100>-oriented growth. At pH 13.5 the polyhedral grain structure is no longer evident as Cu_2O dissolutes in OH^-. It is assumed that dissolution occurs at lower pH as well, but at these pH levels deposition rates are so much higher than dissolution rates, and no evidence of dissolution is apparent during deposition. However, immersing deposited samples in the $CuSO_4$ electrolyte of pH >= 12.5 post deposition, without an applied bias, the samples experience dissolution at elevated temperatures, suggesting that this dissolution is chemical rather than electrochemical in nature.

3.2   Delafossite

Delafossite is a great candidate for STH operations as this section will show. Delafossite was given its name by Charles Friedel (1832-1899) in 1873, as a tribute to his predecessor as Professor of Mineralogy at the Sorbonne, Gabriel Delafosse (1796-1878). [46] Friedels first description was of a Siberian mineral which he found to be of a $Cu_2O \cdot Fe_2O_3$ composition, and Rogers [47] shows that the similar mineral sent to him by 'Mr. Tovote' *...warrant the establishment of delafossite as a distinct mineral species*. But even after a chemical analysis showing a close to Cu:Fe:O=1:1:2 ratio, Rogers are still *left in doubt as to whether the formula of delafossite is* $Cu'Fe'''O_2$ *or* $Cu''Fe''O_2$, but concludes that *it is probably cuprous metaferrite*, $Cu'Fe'''O_2$. Further analysis by Pabst [48] supported this hypothesis, although it was later shown that $Cu''Fe''O_2$ does indeed exist.[1] The delafossite name is also applied in more general terms to structures with $A(I)B(III)O_2$ composition and the same structure as $CuFeO_2$. For that reason, $CuM(III)O_2$ are sometimes referred to as cuprous delafossite. This work use the name delafossite for $CuFeO_2$, unless otherwise stated.

3.2.1   Structure

The crystal structure of $CuFeO_2$ was first proposed by Soller and Thompson, [49] and later confirmed by XRD powder patterns by Pabst [48]. Today it is known that $Cu^{1+}Fe^{3+}$-delafossite crystallizes in two polytypes: the rhombohedral 3R-delafossite as first described by Pabst and the hexagonal phase 2H-delafossite, described by Effenberger. [50] XRD of single crystal $CuFeO_2$ has also been used to show the same results [51]. As mentioned above, a third (although rare) phase also exist, justifying Rogers initial doubts about the chemical constitution and $Cu''Fe''O_2$-delafossite crystallizes in R-3m. [52]

table 2: Crystal structure parameters of $CuFeO_2$.

	3R-delafossite	2H-delafossite
lattice constant	a = b = 3.0349 Å, c = 17.1656 Å [§]	a = b = 3.0349 Å, c = 11.4490 Å *
lattice angles	α = β = 90°, γ = 120° [§]	α = β = 90°, γ = 120° *
space group	**_R_**-3m (166) [§]	**P6**$_3$/mmc (194) *
bond length Cu-O	1.8075 Å [§]	1.8410 Å *
bond length Fe-O	2.0445 Å [§]	2.0281 Å *
cell volume	136.9236 Å^3 [§]	91.3305 Å^3*
formula weight	151.389 g mol^{-1}	151.389 g mol^{-1}
density	5.52 g cm^{-3}	5.52 g cm^{-3}

[§] Villars [53]

*Effenberger [50]

Both the 3R- and 2H-delafossite structure can be visualized as consisting of planar layers of Cu in a triangular pattern and FeO_6 octahedron sharing its edges to the Cu-layer. If the Cu layers are oriented 180° relative to each other, the resulting structure is 2H-delafossite as shown in figure 21 b) and d). When the

---

1   Notation by ′ to indicate positive charge used in an effort to stay true to the original paper by Rogers

3R-delafossite
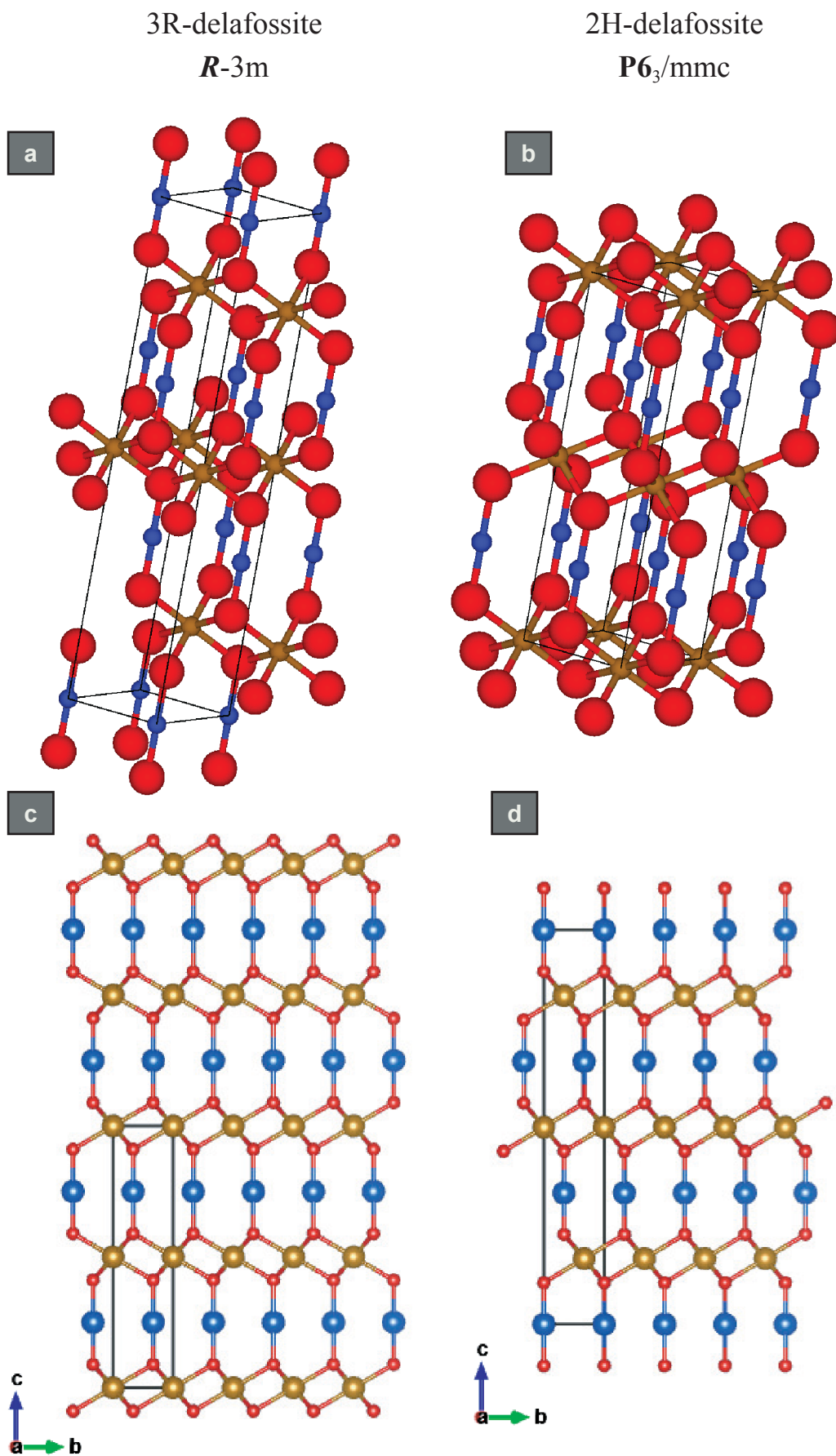**R**-3m

2H-delafossite
P6$_3$/mmc

figure 21: CuFeO$_2$ structure showing the two polytypes, 3R (a,c) and 2H (b, d). Illustrations created using the VESTA software [54], with crystal data from ref. [53] and [50], respectively.

Cu layers are oriented in the same direction but offset from each other by 1/3 in a three layered sequence, 3R-delafossite is formed as depicted in figure 21 a) and c).

3.2.2   Physics of Delafossite

$CuFeO_2$ is an oxide p-type semiconductor with a valence band comprised of hybridized Cu 3d states and O 2p states. In the presence of excess oxygen in the structure, holes form as a result of the oxidation of 3d^{10} Cu(I) to 3d^9 Cu(II) and is the reason for the p-type conductivity. Other cuprous delsfossites have bandgaps > 3 eV, but in $CuFeO_2$ the Fe 3d states form an intermittent band in this wide bandgap with the result that $CuFeO_2$ has a relatively small bandgap of 1.5 eV. The flat band potential E_{FB} is located at 1.05 V vs. RHE (-5.55 eV vs. vacuum), the Fermi-level is located ~60 meV above the valence band and the water reduction potential reported at roughly 300 mV below the CBM, suggesting that $CuFeO_2$ has the capability to produce a high photovoltage for HER. In contrast to Cu_2O, $CuFeO_2$ is a much more robust oxide and can operate in aqueous environments over long time periods (at least days). [55] This is the main motivation for using $CuFeO_2$ over Cu_2O.

Prévot et al. [55] have investigated a sol-gel deposited sample to establish several useful features, in addition to the ones mentioned above. By "mapping" the bandgap of the material using a series of redox species with known electrochemical potentials, they could determine band position and investigate the semiconductor-electrolyte interface. Combining these results with impedance spectroscopy they find a high concentrations of surface states (~10^{14} cm^{-2}) at +0.7 V vs. RHE and suggest *that the majority of the states are accessible under illumination onl*y. These surface states pins the Fermi-level at the semiconductor electrolyte interface, drastically limiting the photovoltage to roughly 0.35 V. However, the flat-band potential (E_{FB} = 1.05 V vs. RHE) and the acceptor density (N_A = 10^{18} cm^{-3}) remained unchanged during illumination. In addition, Prévot et al. report a carrier life time $\tau \sim$ 200 ns, and carrier diffusion length $L_D \sim$ 300 nm. Hence, the limiting factor for PEC performance is not due to bulk properties, but rather the surface states. Prévot et al. estimate that a maximum photovoltage of 0.8 V could be achieved if the surface states could be passivated.

As with Cu_2O, several methods have been shown to deposit $CuFeO_2$. Sol-gel [55][56][57], hydrothermal synthesis [58], PLD [59][60], sputtering [61][62] and electrochemical deposition [63][64] have all been shown to successfully produce $CuFeO_2$. Although crystalline $CuFeO_2$ has been shown to deposit directly by hydrothermal synthesis, samples usually need to be annealed after deposition to become crystalline. Annealing are typically executed at 450-900°C in either Ar or N_2 for 1 - 2 h, depending on the deposition method.

3.2.3 Electrodeposition of Delafossite

To the best of the author's knowledge, only one route to $CuFeO_2$ by electrochemical deposition exists. This route was established by Read et al. [63] and involves using a dimethylsulfoxide (DMSO) solution containing 1 mM copper (II) nitrate, 3 mM iron(III) perchlorate, and 100 mM potassium perchlorate as the supporting electrolyte. This method employs DMSO due to the low solubility of Fe^{3+} in aqueous solution at the pH required for deposition. In practice, this method co-deposits Cu_2O and Fe_2O_3, and subsequently re-structure to $CuFeO_2$ during annealing. As shown in figure 17, the pH required to achieve this co-deposition from an aqueous Fe-Cu-S-O-H system is pH 5 - 14, a region where solved Fe^{3+} will reduce or precipitate (depending on the conditions and system).

Riveros et al [64] develop this route further, pointing to the importance of the complexing agents in controlling the quantity of copper in the films. By controlling the concentration of chloride in the solution they show that co-deposition of stoichiometric films are achieved, and utilize a chlorate / perchlorate mixture to control copper concentrations (0.01 M $CuCl_2$+ 0.005 $Fe(ClO_4)_3$ + 0.1 M $LiClO_4$ + DMSO). By saturating the solution with molecular oxygen before and d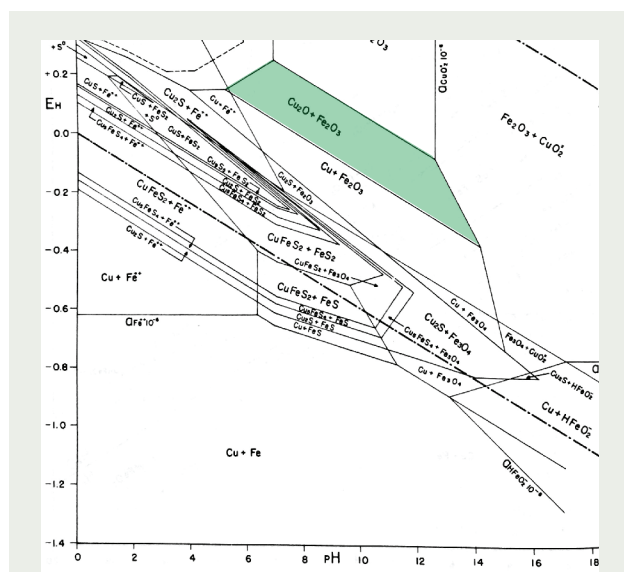uring deposition, they achieve a 1:1 ratio of Cu:Fe in their films by potentiostatic deposition at -0.6 V vs. Ag/ $AgCl_{(sat)}$ at 50°C. The as-deposited films were shown to be amorphous and subsequent annealing at 650°C for 30 min was required to achieve crystalline $CuFeO_2$.

A fundamental limitation to electrodepositing $CuFeO_2$ is the poor conductivity of the amorphous material deposited, preventing charge from transferring to the surface, and hence limiting the deposition thickness to ~130 nm. As a result of this, the photocurrents reported by Read et al. are very low, stabilizing at 16 $\mu A\ cm^{-2}$ after an initial value of 85 $\mu A\ cm^{-2}$. By introducing molecular oxygen through bubbling and using this as a sacrificial electron scavenger, they were able to reach a stable value of 160 $\mu A\ cm^{-2}$.

figure 17: Pourbaix diagram of the Fe-Cu-S-O-H system at 25°C. Total dissolved sulfur = 10^{-4} m. The zone of $Cu_2O \cdot Fe_2O_3$ co-deposition highlighted in green. (image is a scan of the book *Solutions, Minerals, and Equilibria* [65])

3.3 Photoelectrochemistry

This review section covers history, state-of-the-art performances in different cell configurations and promising photoelectrodes for water splitting PEC cells concerning, as well as relevant work on cop-

per-based photocathodes.

3.3.1   Water Splitting Photoelectrochemical Cells

The first paper to describe water splitting by a PEC cell was Fujishima and Hondas' Nature article *Electrochemical Photolysis of Water at a Semiconductor Electrode* in 1972. [66] They used a single crystal TiO_2 anode and a Pt-metal cathode and reported both an increase in anodic current and oxygen gas evolution. Furthermore, they showed that the photocurrent onset potential corresponded to the flat-band potential.

This discovery sparked interest in the scientific community, leading to numerous studies, especially on wide bandgap semiconductors like TiO_2. Oxides were particularly attractive, but as Grätzel [16] points out, none of these oxides meet all the requirements to serve as ideal photoelectrode materials. It proved to be particularly challenging to combine suitable bandgaps with proper band edge positioning. In 1975, Yoneyama et al. [67] showed a tandem cell exclusively made of semiconductor electrodes. In this study, the authors use TiO_2 as photoanode and p-type GaP as photocathode. Initially, they advocate the use of p-GaP as photocathode material on the grounds of stability, but encounter photodegradation in their cell and accounts this to the p-GaP photocathode. They conclude that the *utilization of solar energy was found to be quite limited by the pair of semiconductors chosen*, but was still able to detect hydrogen evolution on the cathode and visibly confirm oxygen formation on the anode.

There are plenty of recent reviews commenting on the same challenge as Yoneyama tried to tackle, namely that of combining semiconductors to optimize STH. Hu et al. [7] did a comprehensive analysis of the optimal band gaps of light absorbers in integrated tandem photoelectrochemical water-splitting systems. The calculated maximum STH efficiency for an integrated photoelectrochemical system was found to be 31.1% at 1 Sun (= 1 kW m^{-2}, air mass 1.5) and fundamentally limited by a matching photocurrent density of 25.3 mA cm^{-2} produced by the light absorbers.

3.3.2   Photoelectrode Materials

A system using photoactive materials for the hydrogen evolution reaction (HER) and the oxygen evolution reaction (OER) is limited by the power of the incident sunlight (0.1 W cm^{-2} at most), which means that realistic current densities are on the order of 10 mA cm^{-2} for such systems (compared with ~0.5–2 A cm^{-2} for commercial electrolyzers).This means that combining cheap materials with low-cost manufacturing is critical to making the technology viable since a photoelectrochemical solar-to-hydrogen device would require around 50–200 times the electrode area of a conventional electrolyzer to achieve the same amount of product. [68]

Roger et al. [68] compile a comprehensive list of earth-abundant HER and OER photoelectrochemical systems in conjunction with catalyst materials. A n^+–p–p^+ -Si sandwich covered by a CoPS catalyst shows

the highest cathodic photocurrent of the HER cathodes at -35 mA cm^{-2} (at 0 V vs. RHE, 1.0 sun illumination, pH=0). Further, they show that Co, Ni, and Fe are the go-to elements in choosing co-catalysts for OER, the best performing being a $BiVO_4$ electrode first covered with NiOOH and subsequently with FeOOH.

The current world record for STH (to the best of the authors' knowledge) is held by scientists at the U.S. Department of Energy's (DOE) National Renewable Energy Laboratory (NREL), reporting an STH of 16.2% (at AM1.5G) in a so-called inverted metamorphorphic multijunction device. [69] This device is indeed complex and comprise of a Si-epoxy-Au-GaInAs-CGB-pGaInP-nGaInP-nAlInP-nGaInP-layered photocathode in contact with a RuO_x anode. This is certainly a high performance system, but the complexity of production and extensive use of rare-earth elements exclude it from the discussion of materials for practical device implementation.

3.3.3   Cuprous Oxide Photocathode

Hara et al. [70] reports using Cu_2O powder as a photocatalyst for overall water splitting in 1998, without noticing any decrease in activity over a 1900 hour period. Motivated by the findings in this work, de Jongh et al. [71] use electrodeposited Cu_2O on an FTO substrate as a photoelectrode in a PEC cell and investigates its properties. They report that Cu_2O is unlikely to achieve water splitting, but communicate high efficiencies for the photocathodic reduction of oxygen and methylviologen cation, and conclude that *cuprous oxide could be promising as a p-type photoelectrode in an electrochemical photovoltaic cell*.

In 2008, Nian et al. [72] report direct evidence that the photoinduced charges in the conduction band of p-type Cu_2O reduce water to H_2 in a 0.5 M $NaSO_4$ electrolyte. They achieve the Cu_2O samples by electrodeposition on ITO. Also, they comment on the effect of electrodeposition temperature on HER, stating that samples deposited at 25°C show higher photocurrents than samples deposited at 65°C. They attribute the increase in photocurrents to a difference in crystal orientation; they observe exclusively (111) orientations in samples deposited at 25°C, while observing only (110) and (220) orientations in samples prepared at 65°C.
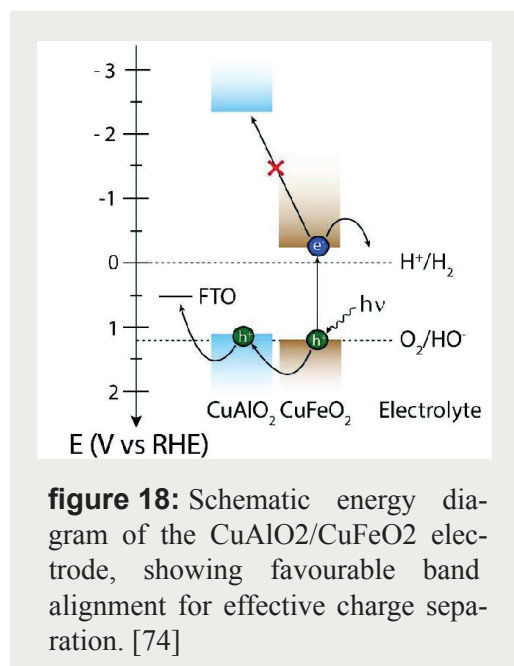
Parrachino et al. [30] investigates the deposition parameters further and backs the Nian et al. paper on the fact that lower deposition temperatures increase photocurrents. Their highest photocurrent obtained was -2.4 mA cm^{-2} at 0.25 V vs. RHE for a film thickness of 1.3 μm, deposited galvanostatically at -0.1 mA cm^{-2} for 220 min at 30°C and pH 12. A corollary paper was published by the same group on the use of these samples in a PEC cell, showing hydrogen evolution with a Faradaic efficiency of close to 100% at 0 V vs. RHE. [6] The latter also investigates protecting the Cu_2O against photocathodic decomposition, using a combination of protective ZnO, Al_2O_3, and TiO_2 layers to both increase stability and performance. They show that Cu_2O can perform to 78% of the initial photocurrent after 20 minutes of illumination by applying a protective layered structure of '5×(4nm ZnO/0.17nm Al_2O_3)/11nm TiO_2' by atomic layer deposition

(ALD) on top of the electrodeposited Cu_2O.

3.3.4   Delafossite Photocathode

Read et al. [63] was one of the first to communicate using thin film $CuFeO_2$ as a cathode material in a PEC cell for water splitting. Although they report only small photocurrents, less than 100 µA cm^{-2} without an electron scavenger present, the photovoltage and proof of hydrogen product showed that the material had favorable band positioning for HER. However, other methods have shown much better results, such as sol-gel deposition with post treatment by hybrid microwave annealing (HMA). HMA post-treatment in air enhanced the activity of the electrode more than 4 times compared to samples without HMA, from -0.3 to -1.3 mA cm^{-2} (at 0.4 V vs. RHE). The same group also modifies the $CuFeO_2$ electrode with a NiFe-layered double hydroxide (LDH)/reduced graphene oxide (RGO) electrocatalyst, showing an even higher photo-current of -2.4 mA cm^{-2}. [73]

The Sivula group at EPFL[2] have published numerous articles on the subject of using $CuFeO_2$ as photoca-thode in PEC and through the doctoral work of M. Prévot [74] developed and optimized a robust sol-gel-process *in an attempt to overcome issues with controllable film deposition and improve electrode performance.* By this method, Prévot reports steady state photocurrents of 1.05 mA cm^{-2} for a ~300 nm thick electrode at 0.4 V vs RHE when using O_2 as a sacrificial electron acceptor. While this work demonstrates the photocathodic capabilities of $CuFeO_2$ for solar water reduction, self-sustained water re-duction (i.e., without a sacrificial electron acceptor) can not be achieved due to poor charge separation. In an effort to overcome this limitation, Prévot investigates the possibility of using $CuAlO_2$ as a scaffolding for the $CuFeO_2$. [75] $CuAlO_2$ (Eg = 3.5 eV) has a much larger bandgap than $CuFeO_2$, but the VBM is only slightly higher in energy, which would favor hole transport from $CuFeO_2$ to $CuAlO_2$, while blocking any electron trans-port in the same direction, as shown in figure 18. This charge separation is indeed shown to have a positive effect on photocurrents, and an increase from ~1 mA cm^{-2} to 1.95 ± 0.25 mA cm^{-2} is shown at 0.4 V vs. RHE. As the bare $CuAlO_2$ showed only a small photocurrent of 0.13 mA cm^{-2}, the increase in observed photocurrent in the $CuAlO_2$/$CuFeO_2$ scaffolding system is accredited to the charge sep-aration of the scaffold.

figure 18: Schematic energy dia-gram of the CuAlO2/CuFeO2 elec-trode, showing favourable band alignment for effective charge sepa-ration. [74]
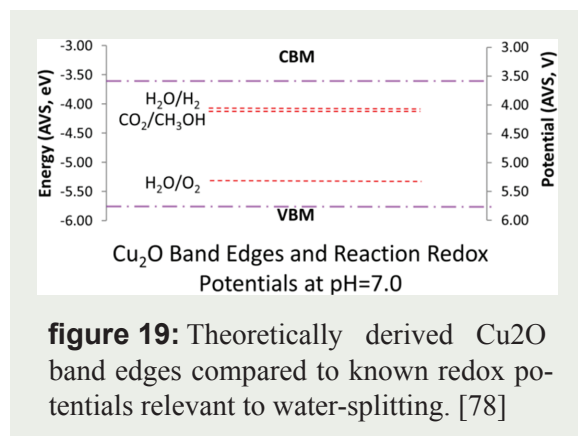
In a recent article (march 2018) Crespo [76] investigates the *potentiality of CuFeO$_2$-delafossite as a solar energy converter* through *ab initio* calculations on both ferromag-

netic and antiferromagnetic spin ordering. Especially two aspects of this paper is worth mentioning: first the analysis on the optical properties shows that any Cu-Fe transitions *are very improbable*, and that light absorption originates from Cu-Cu and O-O transitions. However, several papers show an indirect transition in $CuFeO_2$ by UV-vis absorption spectrum of ~1.5 eV, confirming that these transitions in fact do occur. Secondly, Crespo shows that the maximum theoretical photovoltage of $CuFeO_2$, even with maximum sunlight concentrations, are not high enough for water-splitting and only reaching a theoretical maximum at 1.1 V (antiferromagnetic), less than the 1.23 V needed to split water.

3.4 Quantum Mechanical Modelling of Cuprous Oxide

In addition to experimental device preparation and characterization, Cu_2O has seen a lot of attention on *ab initio* calculations and quantum modeling concerning the nature of electronic and optical properties, its band structure, surface stability and structure etc. Understanding these mechanisms is essential in order to achieve better performing devices, and the fundamental understanding of surfaces and interfaces are of great help when trying to stabilize and optimize oxide PEC systems.

In an effort to establish proper procedures, and determine functionals for studying the ground state

figure 19: Theoretically derived Cu2O band edges compared to known redox potentials relevant to water-splitting. [78]

properties of Cu_2O, Isserhoff et al. [77] conducts a thorough survey of common DFT-based approaches and XC functionals. By comparing numerical results and analyzing the accuracy of DFT, DFT+U and DFT with hybrid functionals, they conclude that *the HSE functional as the most accurate in reproducing a number of experimental observables, confirming it as the proper functional for studying ground-state properties of Cu_2O*. However, to reproduce and analyze more complex features like the photoemission/inverse-photoemission spectrum, they conclude that a combined HSE+G_0W_0 approach is the best, as long as the correct Hamiltonian is chosen. This should also serve well as a starting point for calculating and studying the optical absorption spectrum of Cu_2O, according to the authors.

A subsequent paper by Bendavid et al. [78] (same group) propose *first-principle predictions of the structure, stability, and photocatalytic potential of* Cu_2O *surfaces* by implementing the approach mentioned above. In this work, calculations of a wide array of different surface configurations were conducted in order to obtain the most stable configuration for use in the calculation of the band edges. The results of this procedure is shown in figure 19 and reveal that, according to this paper, Cu_2O is a good photocathode material for PEC cell applications.

As mentioned in the chapter on semiconductor theory, several materials properties can be derived by

looking at the band structure of the material, and Cu_2O is no different. Heinemann et al. [79] calculates band structures and DOS for all the Cu-based oxides (Cu_2O, CuO and Cu_4O_3) using LDA+U and HSE06
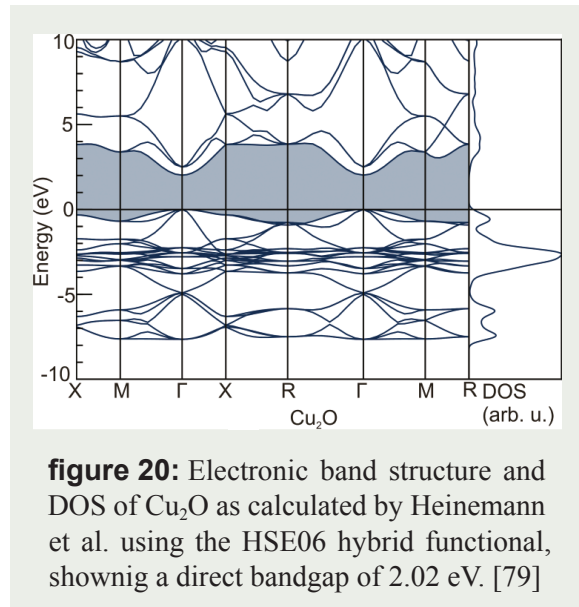

figure 20: Electronic band structure and DOS of Cu_2O as calculated by Heinemann et al. using the HSE06 hybrid functional, shownig a direct bandgap of 2.02 eV. [79]

hybrid functionals, and show a direct bandgap in good agreement with experimental values using the HSE06 hybrid functional; E_g = 2.02 eV against 2.1 eV (experimental, [40]). Heinemann also comment on the fact that transition to the first conduction band is dipole forbidden, and report the optical excitation energy to the second conduction band to be 2.5 eV (2.64 eV experimental, [40]).

Yet another feature that has been investigated using *ab initio* calculations is the *origin of the p-type nature and cation deficiency in* Cu_2O *and related materials*, by Raebiger et al. [80] They show that Cu_2O *is intrinsically copper-deficient due to formation of copper vacancies* V_{Cu} *that act as a shallow and efficient hole producer.* Cu_2O *is intrinsically p-type because (a) the potential hole killer* V_O *has no transition level in the gap and thus cannot annihilate holes, and (b) the possible hole killer* Cu_i *has both high formation energy and deep transition level and is thus incapable to efficiently destroy holes created by* V_{Cu}. They point to low formation energies of V_{Cu} in the cuprite structure, contrary to other main group oxides showing a much higher cation vacancy formation energy, and calculations of LDOS of the ideal Cu vacancy in Cu2O show a resonance at 4 eV below VBM *implying that the hole produced by* V_{Cu} *"float up" and occupy a delocalized perturbed-host state just above the VBM.*

3.5 Summary

From this review of literature concerning Cu_2O and $CuFeO_2$ it is obvious that both materials are very good candidates for water splitting and hydrogen production by solar energy conversion, each with their strengths and weaknesses. By comparing the bandgaps of the two in the context of the review by Hu et al. [7] it is apparent that the lower bandgap of $CuFeO_2$ is favorable, assuming that the cathode act as the underlaying electrode in a PEC cell. $CuFeO_2$ also show a superior stability in aqueous solution under illumination but the experimental photocurrents achieved are still much lower than what is seen in Cu_2O photocathodes.

In addition to suitable bandgaps, both materials exhibit great band alignment for solar hydrogen production. However, because of high concentrations of surface states, photodegradation of the material, or ineffective electron-hole separation, there is still a lot of optimization to be done in order to even remotely approach the maximum theoretical photocurrents. Even so, clear evidence of hydrogen production has

been published for both Cu_2O and $CuFeO_2$, and both materials see an increasing interest in their use as a photocathode material.

Several methods have been shown to produce both Cu_2O and $CuFeO_2$. Electrodeposition of Cu_2O has been proven highly successful, while electrodepositing $CuFeO_2$ has its challenges. In general, electrodeposition has the advantage of scalability and low-cost, but generally results in samples with lower efficiencies and lower charge carrier concentrations than other more advanced methods, such as sputtering and sol-gel. Even so, electrodeposited Cu_2O shows great prospects and promisess as a scalable and low cost method to produce photocathodes for PEC cells.

To overcome the challenge of photocorrosion in Cu_2O, layered protection have been introduced. This is not only acting as protection layer, but also as a performance enhancer, and using other cheap and scalable oxide materials has been shown.

Lastly, *ab initio* calculations have been shown to be a powerful tool in predicting the properties of Cu_2O, predicting bandgap values and band positioning close to what experimental works has shown by using the HSE functional.

4   Methods

In this project, work has been directed at producing high quality samples of both Cu_2O and $CuFeO_2$ on different substrates in order to confirm results reported in literature, and produce new results to test the hypothesis brought forward in this work. Samples were produced by electrochemical deposition and pulsed laser deposition was used in order to cover a small selection of samples with TiO_2. Samples were characterized by XRD, SEM and TEM to establish bulk properties such as crystallinity, composition, thickness etc. Electrochemical methods were used in order to determine PEC performance. In addition to *In-* and *Ex Situ* characterization, *ab initio* calculations were performed to better understand the intrinsic properties of the Cu_2O. In this chapter, all the above mentioned techniques and methods are explained, enabling the reader to better understand the work as a whole.

4.1   Sample Preparation

In an effort to consistently produce high quality samples, a lot work was dedicated towards finding suitable substrates, optimizing hardware configurations and establishing deposition parameters. In total, more than 100 samples have been prepared to better understand the systems in question and the effect different parameters have on the resulting samples. Also, a number of hardware configurations have been considered and assessed, and several methods for cleaning substrates prior to deposition has been tested.

4.1.1   Substrates

table 3: substrates used and their specifications according to manufacturer

given name	specifications	Normalized area per nominal cm^2
C-paper	**carbon paper** Quintech Toray Carbon paper, TP-060 untreated	1 cm^2
SS-mesh	**stainless steel mesh** Goodfellow Cambrige Ltd. part #: FE228710 Wire dia.: 0.25 mm, open area: 37 %	0.63 cm^2
Ti-mesh	**titanuim mesh** Goodfellow Cambrige Ltd. part #: TI008710 Wire dia.: 0.23 mm, open area: 20 %	0.8 cm^2
FTO	**flourine doped SnO_2 on glass** Sigma-Aldrich Surface resistivity ~13 Ω cm^{-2}	1 cm^2
Fine SS-mesh	**fine stainless steel mesh** Alfa Aesar, Thermo Fisher Sci. part # 13476 Wire dia.: 0.05 mm, open area: 36 %	0.64 cm^2

I total, five different substrates have been used in this work: carbon paper (C-paper), two configurations of stainless steel mesh (ss-mesh and fine ss-mesh), titanum-mesh (Ti-mesh) and flourine doped tin oxide covered glass (FTO). In order to achieve values from experimental measurements that are comparable to other works, and across substrates, a rough normalization of substrate surface area was conducted, and is calculated on the basis of the open area of the mesh given in the specification section of table 3, where applicable. Since the C-paper are not a mesh-type substrate, normalized area is set to equal the nominal area. Also, the specifications regarding all substrates are provided in table 3.

Cleaning

A wide variety of chemicals and solutions have been tested in order to clean substrates prior to deposition in order to ensure high quality samples and good PEC performance i.e. by good substrate adhesion, uniform coverage etc.

When depositing on carbon paper no initial cleaning was utilized as the stock substrate was shipped and stored in an airtight wrapping and only exposed to the environment as small 1x1 cm pieces were cut.

All mesh substrates were cleaned by either of the following:

- 10 min 0.5 M $NaSO_4$ + 10 min DI H_2O (all in ultrasonic bath)
- 10 min acetone + 10 min DI H_2O (all in ultrasonic bath)
- 10 min acetone + 10 min isopropanol + 10 min DI H_2O (all in ultrasonic bath)
- 10 min acetone (ultrasonic bath) + electrochemical cleaning in 2.0 M KOH

Electrochemical cleaning was done by cyclic voltammetry at a scan rate of 1000 mV s^{-1} ranging from ~-0.5 V to ~1.5 V in a two electrode set-up at room temperature with a platinum counter electrode, using a 2.0 M KOH electrolyte.

All substrates were subsequently dried in air before immersed in electrolyte for deposition.

4.1.2 Electrochemical Deposition of Cu_2O

Several methods for electrodepositing Cu_2O has been established as discussed in section 3.1.2 on page 22, and deposition of Cu_2O in this work is to a large extent based on the process described by Paracchino et al. [30] with slight modifications. Cu_2O was deposited on all substrates mentioned above, except FTO, although the stainless steel mesh became the main substrate for deposition as work progressed.

Electrolyte

To deposit Cu_2O, an alkaline lactate-stabilized copper sulphate solution was used with dipotassium phosphate working as a buffer in DI H_2O, adjusted to pH 12 by potassium hydroxide, with concentrations given in table 4.

The chemicals were mixed with DI H_2O and stirred well for periods of 24 hours to ensure a homogeneous solution. A stock solution (before pH adjustment) were typically made in 500 ml batches or 25 ml for single electrolyte use. KOH was then added over a few minutes to the stock solution to adjust pH to 12, culminating in 80 to 100 ml finished electrolyte. Lactic acid is crucial as it acts as a complexing agent to the Cu^{2+} ions and stabilize these, avoiding precipitates ($Cu(OH)_2$) as pH is increased to 12.

table 4: copper sulphate plating bath concentrations

Chemical	Concentration
$CuSO_4$	2.0 M
K_2HPO_4	0.5 M
Lactic acid	3.0 M
KOH	2.0 M

Equipment

Two deposition set-ups have been used, the second an improved version of the first, building on the experiences using the first set-up.

Initially, an open beaker system was adopted as depicted in figure 22 (a) with the electrodes and a temperature sensor suspended by an external support. Temperature was controlled by a heated stir plate connected to the temperature sensor.

As discussed in section 3.1, Cu_2O deposition is highly dependent on several factors, including temperature. In an effort to better control deposition temperatures a double walled beaker was made, allowing a Julabo EC-5 water heater to circulate heated w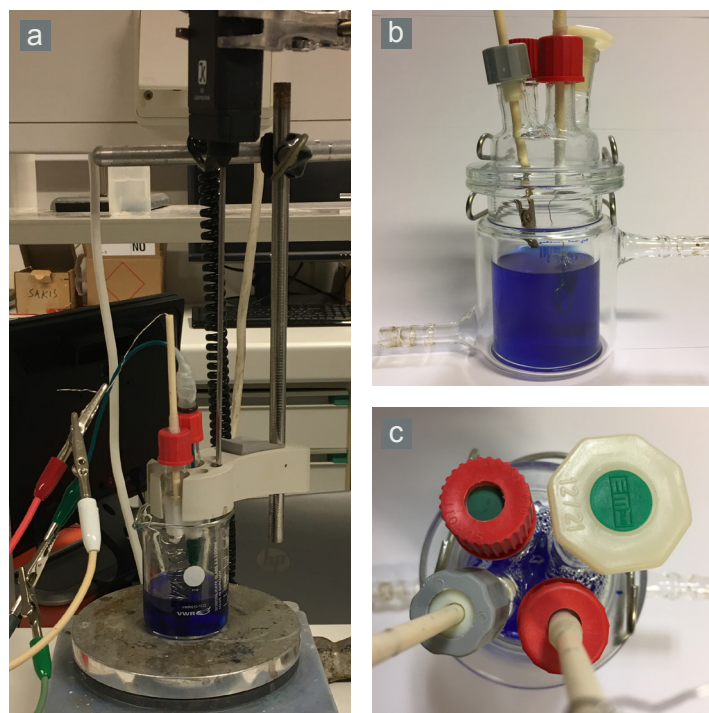ater uniformly around the electrolyte as shown in figure 22 (b). In addition a gas-tight lid was made facilitating three electrodes and gas inlet as seen in figure 22 (c, top-view). In this set-up, the stir plate was used only as a stirrer where applicable, and no heat was applied from the plate. A water bath temperature was established prior to deposition so that no temperature sensor was needed during deposition.

Both two and three electrode configurations were used, with either a silver chloride or standard calomel electrode as reference electrode in the three electrode configuration, and a coiled up platinum wire working as counter electrode in both cases. However, only results from galva-

figure 22: Initial deposition set-up **a**) and a second set-up with improved temperature control and gas-tight lid fascilitating three electrodes and a gas-inlet **b**, **c**.

nostatic, two electrode, setups are reported in this work. A Parstat 2273 potentiostatic/glavanostatic cell controlled the deposition in conjunction with the PowerSuite software provided by Princeton Applied Research.

Deposition parameters

In order to establish parameters that would consistently produce high quality samples, Pourbaix diagrams of copper solutions were studied. Pourbaix diagrams can be seen as a map of thermodynamic information and shows whether a chemical reaction can proceed or not. The technique used to draw Pourbaix diagrams rest on understanding half-cell reaction potentials between an oxidized and a reduced chemical species,

$$Ox + ne^- \leftrightarrow Red \qquad (4.35)$$

with the corresponding half-cell potential given by the generalized Nernst equation,

$$E_H = E^0 + \frac{2.3RT}{nF} \log \frac{[Ox]}{[Red]} \qquad (4.36)$$

where E_H is the half-cell potential relative to the standard hydrogen electrode, E^0 is the standard half cell potential, R and F are the universal gas and Faraday constants respectively, and T is the absolute temperature. By considering all half reactions in a system with the appropriate activities and standard potentials, a full Pourbaix diagram can be derived by using equation (4.36).

The Pourbaix diagram provided in figure 23 shows the region where Cu2O deposition can occur according to the plating bath pH and deposition potential. At the concentration and temperature given in figure 23 a deposition potential of -0.2 V vs. SHE marks the transition from Cu to Cu_2O. The deposition parameters was to a large extent established using recipes developed in other works, but the Pourbaix diagram was still
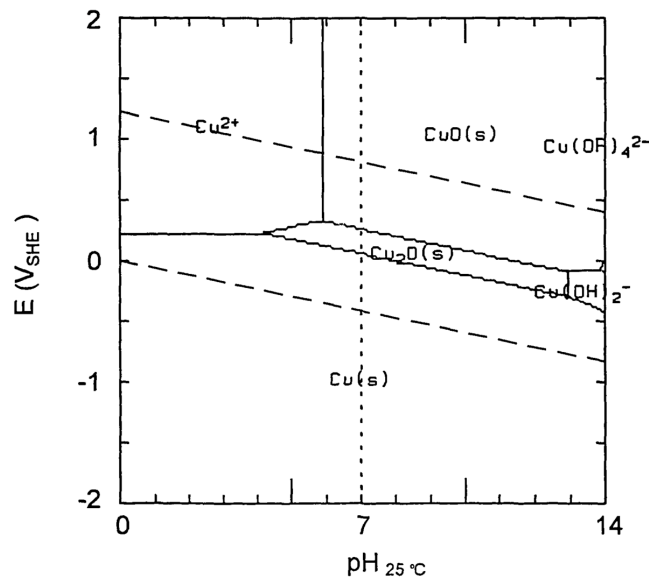

figure 23: Pourbaix diagram for copper at 25°C with a total concentration of soluble species of 10^{-4} mol kg^{-1} [81]

used to gain valuable insight in deposition parameters.

The deposition parameters given in table 5 show the range of parameters used. The specific deposition parameters of samples presented in the results section are stated where appropriate. Deposition currents are not given in area specific terms, as the substrates are made of mesh and the actual area of the substrates are hard to predict. All deposition currents are therefore absolute values, and since all samples have been made to have a nominal area of 1x1 cm; deposition currents can be seen as current (mA) per nominal cm^2.

table 5: deposition parameters for Cu_2O

Time	100 - 300 min
Temperature	RT - 60°C
pH	12
Current	0.1 - 0.36 mA
Potential	-0.5 V vs $Ag/AgCl_{(sat)}$
Stirring	0 - 650 rpm

4.1.3   Electrochemical Deposition of Delafossite

Compared to Cu_2O, depositing delafossite ($CuFeO_2$) by electrochemical methods is not as straight forward, mainly because Fe^{3+} ions are highly insoluble in aqueous solutions at high pH. A prerequisite for Cu_2O deposition in aqueous solution is a relatively high pH, hence other solvents are needed in order to make an electrolyte where the $Cu_2O \cdot Fe_2O_3$ co-deposition can occur. By using dimethylsulfoxide (DMSO) as solvent, Read et al. [63] established an electrodeposition route that was later refined by Riveros et al. [64], and forms the basis for the $CuFeO_2$ electrodeposition method used in this work. $CuFeO_2$ was only deposited on FTO substrates.

Preparation of electrolyte

To make the electrolyte for $CuFeO_2$ deposition, copper chlorate and iron perchlorate were solved in DMSO with lithium perchlorate as a supporting electrolyte in the concentrations given in table 6.

The chemicals were mixed with DMSO and stirred well for a period of 24 hours in order to ensure a homogeneous solution. Molecular oxygen (O_2) was employed as an oxygen precursor, and prior to each deposition, molecular oxygen was bubbled through the solution for at least 20 minutes. Molecular oxygen was also provided to the system during deposition to ensure O_2 saturation.

table 6: iron-copper plating bath concentrations

Chemical	Concentration
$CuCl_2$	0.01 M
$Fe(ClO_4)_3$	0.005 M - 0.01 M
$LiClO_4$	0.1 M
DMSO	Solvent

Equipment

The equipment used in this section is identical to the equipment described in section 4.1.2 on page 36, with slight modifications. Molecular O_2, as required for this deposition and was achieved by submerging a glass tube with a porous end in the electrolyte, connected to an O_2 gas line. A three electrode configuration was used with a silver chloride reference electrode and coiled platinum wire acting as counter electrode.

figure 24: Image of iron-copper solution during deposition.

Deposition parameters

Samples were potentiostatically deposited at 50°C for 1000 s at -0.6 V vs. $Ag/AgCl_{(sat)}$. The electrolyte was bubbled with 100 mmHg molecular oxygen and stirred at 500 rpm throughout the deposition.

Annealing

The as-deposited $CuFeO_2$ samples were annealed at 650°C in Ar for 30 minutes in an horizontal tube furnace. The sample was placed inside a sealed alumina tube, with Ar supplied inside this tube. The furnace was heated at a rate of 1°C min^{-1} and cooled down to room temperature in Ar atmospheric.

4.1.4 Pulsed Laser Deposition

After electrochemical deposition of Cu_2O, pulsed laser deposition (PLD) was performed on a selection of samples in order to study the effects of a PLD deposited TiO_2 layer on top of the Cu_2O electrode. PLD was performed in Ar-atmosphere at 100°C with amorphous TiO_2 as target material. 5000 laser pulses of 30 mJ cm^{-2} at a frequency of 5 Hz were used. The sample was cooled at 5° min^{-1}.

4.2   Materials Characterization

The morphology and substrate coverage have been investigated using an FEI Quanta 200 Field Emission Gun - Environmental SEM (FEG-ESEM). The microscope is equipped with an Everhart Thornley Detector (ETD) that detects secondary electrons and primarily yields information about sample topography, and a Solid-State Detector (SSD) detecting the backscattered electrons, providing information about the phase composition of the sample. Furthermore, the microscope is equipped with EDS (Energy Dispersive X-ray Spectrometer) for investigating the elements present. EDS is not quantitatively accurate but can yield qualitative information about what elements are present in the investigates area. The instrument was operated under high-vacuum.

The crystal structure was investigated using a Rigaku MiniFlex 600 XRD with a $Cu_{\alpha,1}$ radiation source (λ = 1.5046 Å). Measurements were done in the range $2\theta = \{20°,90°\}$ with scan rates ranging from $50°$ min^{-1} to $2°$ min^{-1}, depending on substrate and method. The MiniFlex had to be used in XRF-mode while studying the ss-mesh substrates due to high concentrations of Fe. The resulting diffractograms were analyzed using the Powder Diffraction File database by the International Centre for Diffraction Data (ICDD).

4.3   Photoelectrochemical Characterization

In this section the setup and measurement techniques used for the photoelectrochemical characterization are presented in addition to the equipment used. All photoelectrochemical measurements have been carried out using a Gamry Reference 3000 Potentiostat/Galvanostat, with Gamry instrument framework software.

4.3.1   Photoelectrochemical Cell Setup

Two cell configurations have been used in this work, namely a three electrode liquid cell and a solid state photoelectrochemical (PEC) cell. The three electrode cell used a three-neck beaker with a equipped with a quartz window. A saturated calomel electrode (SCE) electrode was used as a reference electrode (E^0_{SCE} = +0.241 V vs. SHE) and a Pt-electrode acted as the counter electrode. The contact and wires leading to the mesh sample were covered in epoxy and Teflon tape to make sure that the measured sample area always equaled 1 cm^2 (nominal). A 0.5 M $NaSO_4$ aqueous solution was used as electrolyte in the cell and in an effort to remove any residual oxygen dissolved in the solution, the cell was flushed with N_2 for at least 20 minutes before characterization was initiated. This was important since oxygen can act as a sacrificial electron scavenger as briefly discussed in the literature section, and hence affect measurements.

The solid-state PEC (SS-PEC) cell was made by first saturating a Whatman Cyclopore track etched membrane (25 mm diameter, pore size 0.2 μm) with 400 μl of 5% Nafion® (2 x 100 μl on each side, dry before each application), then using 200 μl 5% Nafion® as adhesive for the electrodes. In this manner, electrodes were 'glued' to the membrane; one electrode on each side of the membrane in the center. Afterwards, about

13 kPa pressure was applied to the stack for 12 h at room temperature to fabricate a compact three-layered structure. This layered structure was subsequently mounted in a purpous-built device where the membrane separated two chambers, each chamber connected to its separate gas-mixer, facilitating atmospheric difference between the two sides. The front chamber was additionally equipped with a quartz sight glass, enabeling sample illumination from one side. Wires connected the electrodes to outside connections. Cu_2O on fine ss-mesh substrate was used as cathode in all SS-PEC measurements. Two different materials were used as anode material: a Pt-C electrocatalyst on c-paper (c-black) and anodized TiO_2 nanotubes on Ti-mesh, both prepared as described by Xu et al. [9] The total amount of Pt-C, measured by weighing the c-paper substrate before and after applying Pt-C solution, was found to be ~1.7 mg on a 2 cm^2 circular area.

4.3.2   Light Source

All photoelectrochemical characterization was done using a Newport Oriel® LCS-100 solar simulator with a 100 W ozone-free xenon lamp and a AM1.5G filter. The working distance was regularly checked using a calibrated Newport monocrystalline silicon reference solar cell to achieve a constant intensity of 100 mW cm^{-2} (1 sun). This light source was equipped with an electronic shutter and hence pre-defined light on/off periods can be determined

4.3.3   Cyclic Voltammetry

Cyclic voltammetry (CV) is a technique measuring currents while scanning back and forth over a set potential interval. CV gives information about the reactions that occurs when going in cathodic and anodic directions, and can be used to clean surfaces of contaminants by scanning between OER and HER. In this work CV has been used to check that the electrolytes used show the expected reduction peaks associated with the respective deposition parameters (results not reported). Also, substrate cleaning by CV was employed and assessed, but was found superfluous.

4.3.4   Linear Sweep Voltammetry

Linear sweep voltammetry (LSV) are very similar to CV in that the method measures current at given potentials, but LSV only sweep from a potential to another, one time. LSV is used in work to investigate photocurrents; achieved by finding the absolute value between currents measured in dark vs. light.

4.3.5   Chronoamperometry

Chronoamperometry (CA) is a technique where the potential is set (or stepped) at fixed value and the resulting current is measured. This is particularly useful for studying stability of electrodes when combined

with light on/off cycles. CA is employed in this study to investigate the photodegradation of Cu_2O electrode over time. A constant potential of -0.6 V vs. SCE is used on all CA measurements as this falls close to 0 V vs. RHE in a 0.5 M $NaSO_4$ (pH = 5.6) solution as seen from

$$E_{RHE} = E_{ref} + 0.059 \text{ pH} + E^0_{ref} \tag{4.37}$$

where $E^0_{ref} = E^0_{SCE} = +0.241$ V. With $E_{ref} = E_{SCE} = -0.6$ V and pH = 5.6, it is seen that $E_{RHE} = 0.028$ V.

By utilizing light on/off cycles in CA measurements it is also possible to establish photocurrents in the same way as in LSV, by comparing light on/off current measurements.

4.3.6   Open Circuit Potential

Open circuit potential (OCP) is a measurement of the potential between two electrodes during open circuit operations. OCP is used in this work to establish photovoltage, that is, the difference in measured OCP between light and dark.

4.4   Computational

All calculations in this thesis were conducted using the Vienna *ab initio* simulation package (VASP) with the goal of gaining better understanding of the Cu_2O crystal structure, as well as comparing the electronic structures produced by the PBE and PBE+U functionals. The break conditions for the electronic self consistent field calculations were set to $\Delta E < 10^{-6}$ eV and $\Delta F < 0.02$ eV Å^{-1}, and after performing convergence tests the energy cut-off value for plane wave expansion was set to 500 eV after performing a cut-off test to within 10 meV. A k-point density of (5x5x5) and (4x4x4) was used for PBE and PBE+U calculations respectively. The cubic unit cell of Cu_2O used in the calculations was acquired from ref. [82].

4.5   Sources of Error

Avoiding all errors in experimental work such as this is an impossible task, and it is therefore important to identify sources of error, and invest time in minimizing them. This sections above contains methods used to achieve the results presented in the next section, but these methods are by no means perfect or without errors.

First of all, and maybe the hardest to avoid, the electrode area of the different meshes are difficult to predict with accuracy. One could imagine that calculating the surface area of the wires in the mesh, and multiply by the number of wires per cm^2, would be the most appropriate. However, a big portion of this area will be in contact with other wires, area that would not get exposed to the electrolyte. By taking the approach used in this work, i.e., normalizing the area per nominal area by looking at the mesh as a 2D structure exposed to the incident light, errors in, e.g., photocurrent measurements are unavoidable.

The light source was regularly calibrated, but the sample placement at the working distance yielding 1 sun was performed manually. The discrepancy in intensity around the working distance was checked with the calibrated solar cell provided by the manufacturer and found to be reasonably small, and a sample placement within ±3 mm relative to the working distance of 1 sun intensity, was demonstrated to perform within ±0.01 sun.

A digital pH meter was used and regularly calibrated; however, with the ponderous effect of pH on Cu_2O deposition, even pH fluctuations within the margin of error of the instrument (pH ± 0.01) could potentially affect the sample outcome and performance.

Constructing SS-PEC cells were difficult in many ways, and results and outcomes of these cells are assumed to be highly dependent on mechanical and structural factors (membrane adhesion, contact to ouside wire, membrane integrity etc). Routines to make every cell the same were employed, but quantitative results such as photocurrents are still thought to have been greatly affected by the factors mentioned above.

5 Results and Discussion

5.1 Fabrication and Characterization of Cuprous Oxide Electrodes

As previously discussed in the literature section the bandgap and band locations of Cu_2O make it highly suitable for PEC cell solar-to-hydrogen operations. With a bandgap of 2.1 eV and a favorably located conduction band, it has been shown to evolve hydrogen upon illumination in aqueous solutions. Simultaneously, previous works indicates that Cu_2O photocorrodes quickly and thereby losing photocatalytic capabilities. It is established that deposition parameters affect Cu_2O performance significantly in PEC operations, and a better understanding of these deposition parameters are therefore needed.

This section investigates electrochemical deposition of Cu_2O, discusses the use of different substrates concerning performance, and study deposition parameters and their effect on the resulting Cu_2O electrodes. Cu_2O electrodes are incorporated in a solid-state PEC cells to examine the stability of the electrodes in a non-liquid phase. It also reports on the results achieved by covering Cu_2O electrodes by a layer of TiO_2 with the purpose of improving performance and increase stability.

5.1.1 Electrochemical Deposition of Cu_2O

As one of the primary goals of this thesis is to investigate the possibilities for a solid-state photoelectrochemical cell (SS-PEC) with water splitting capabilities using Cu_2O as a photocathode, a lot of effort has gone into studying the mechanisms of deposition of this material. Cu_2O has been deposited on several different substrates in an attempt to find the best performing and best suitable substrate for use in the SS-PEC cell. The criteria set forth are good photocurrent, mechanical compatibility with the SS-PEC cell, deposition reproducibility, and surface coverage.

Initial depositions were conducted using carbon paper (C-paper) as a substrate. The C-paper has a favourable porous structure that provides a large surface area, and will allow any gas products to escape during PEC cell operation. Besides, C-paper substrates are highly conducting, and since it is a very bad electrocatalyst for HER, any photoelectric activity seen during electrochemical characterization would be accredited the Cu_2O electrode. Furthermore, the carbon paper has been successfully used in previous versions of the SS-PEC cell as support for Pt-C electrocatalyst. All depositions on C-paper were deposited galvanostatically, and typical results are shown in figure 25 (left). Ti-mesh and stainless steel mesh (ss-mesh) were later used as substrates to compare performance with the C-paper. Both Ti-mesh and ss-mesh have much the same beneficial features as C-paper, such as conductivity, bad HER electrocatalysts and porosity to facilitate removal of any gas product.
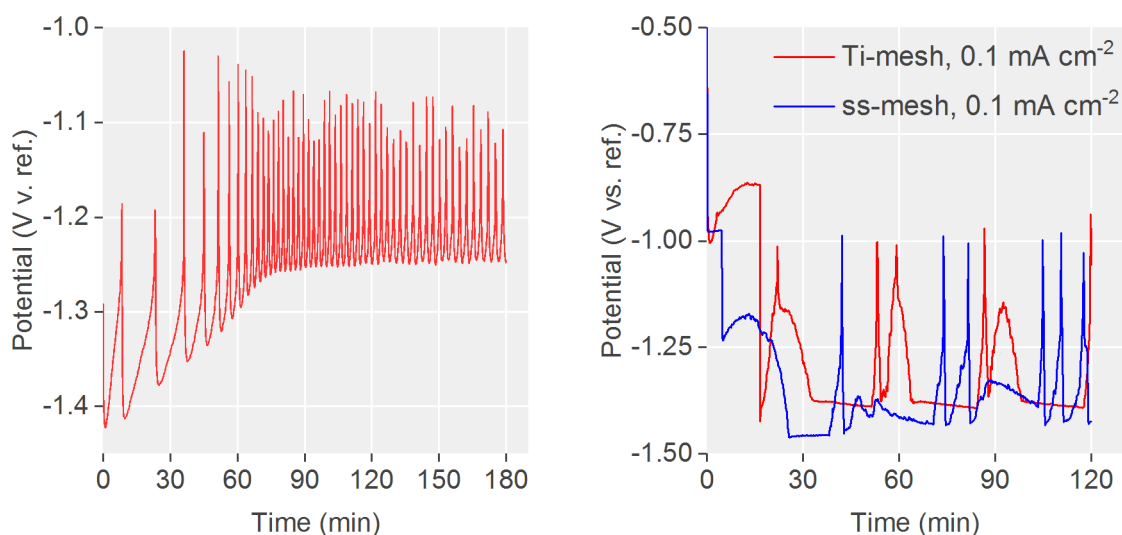
figure 25: Galvanostatic electrodeposition of Cu_2O at -0.1 mA cm^{-2} at 30°C for 180 min on C-paper substrate (left) and on Ti-mesh and ss-mesh substrates at 0.1 mA cm^{-2} at 30°C for 120 min (right). Temperature was regulated by heat plate.

The resulting potential vs. time plots of the depositions on C-paper, Ti-mesh, and ss-mesh seen in figure 25 show fluctuating potentials. This behaviour are usually the result of a change in depositing species and further investigation led to the papers of Switzer et al. [44] and Leopold et al. [45] where the authors propose a mechanism for the spontaneous potential oscillations seen in figure 25. Leopold et al. believe that the oscillations are caused by variations in pH close to the electrode and that potential spikes relate to a *decrease* in pH at the cathode. From reaction (3.34) and (3.33) it is seen that formation of Cu_2O consumes OH$^-$. If OH$^-$ ions in the solution experience low mobility, it is possible that more OH$^-$ are consumed at the electrode surface than what the solution can provide during the periods of potential decrease. At a certain point, the concentration of OH$^-$ reach values too low to support Cu_2O formation and a sudden shift to Cu deposition is seen. From the Pourbaix diagram of the aqueous Cu-O system (figure 23), it is likely that we see a transition over the Cu-Cu_2O phase boundary during this type of deposition.

Spontaneous Potential Oscillations

To better understand the spontaneous potential oscillations occurring during galvanostatic deposition, the deposition mechanisms and the structures resulting from these oscillations were studied. Since the oscillations were thought to be an indication for co-deposition of Cu_2O and Cu, it was deemed essential to gain a better understanding of this process; metallic Cu in the samples are known to deteriorate performance and avoiding oscillations during depositions were thought beneficial.

To investigate this phenomenon, several samples were deposited consecutively on ss-mesh substrates from the same solution without replenishing KOH, as a lowered pH in the electrolyte were thought to trigger the oscillations. As shown in figure 26, the oscillations were in fact encountered after a steady, non-oscillating period. Deposition of this samples was started after approximately 300 min of deposition at -0.25

mA from the same electrolyte; this sample is henceforth referred to as *sample 2*. Due to the steady and typical depositing potential observed, *sample 1* is acting as a reference in this case (sample 1 was not deposited from the same solution as sample 2 but with identical parameters). These samples were then investigated using SEM, TEM, EDS, and XRD.
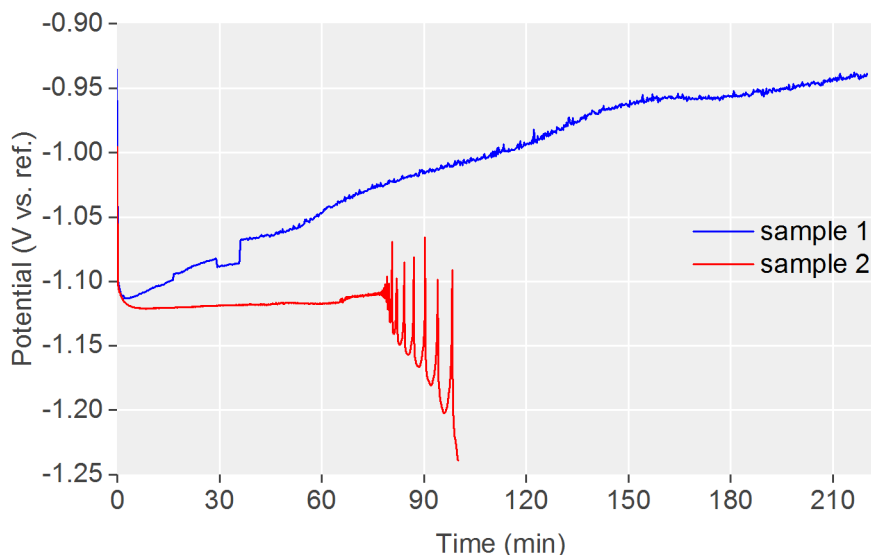

figure 26: Potentials measured during galvanostatic deposition of samples 1 and sample 2. Both samples were deposited at -0.25 mA, 30°C and pH 12 on ss-mesh substrates.

SEM was used to examine both sample 1 and sample 2, and the resulting images are shown in figure 27. The left SEM image shows the Cu$_2$O crystalline structure we expect to see, while the right SEM image exhibit a different morphology. The underlying structure in sample 2 seems to be the same as the structure seen in sample 1, but with additional new structures on top. These structures are henceforth termed *cauliflower structures*, and appear in all samples where potential oscillations start after a period of deposition at 'steady,' non-oscillating potentials. It is therefore assumed that these cauliflower structures arise as a direct consequence of the potential oscillations observed during galvanostatic deposition.
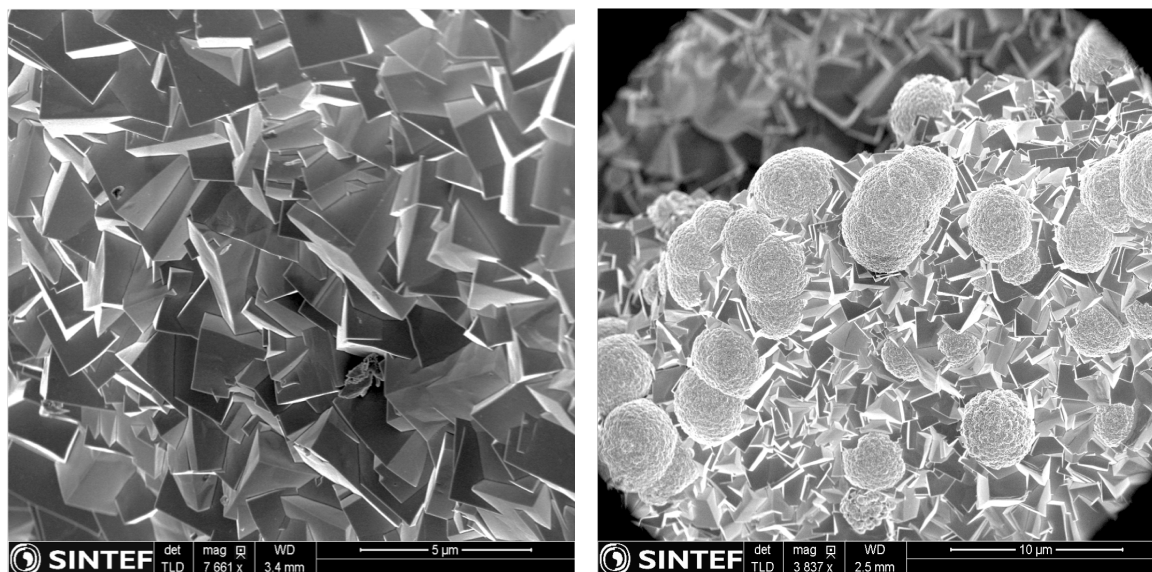
figure 27: SEM images of sample 1 (reference sample, left) and sample 2 (right)

By looking at a cross-section of these cauliflower structures with scanning transmission electron micros-
copy (STEM), it is clear that the cauliflower structures grow on top of already established crystalline Cu_2O.
The cauliflower structures in figure 28 show that the structures are composed of a mix of phases, indicated
by the contrast in the high angle annular dark field (HAADF) STEM scan. Energy-dispersive x-ray spec-
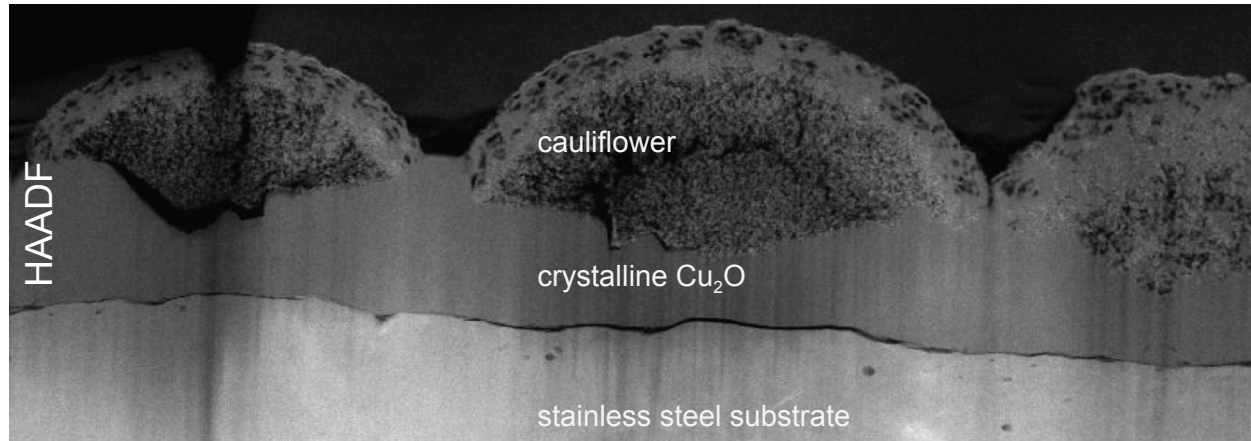

figure 28: Focused ion beam (FIB) lamella cut accross 3 cauliflower structures in sample 2.

troscopy (EDS) was subsequently used to establish the composition of these phases, and the results from
this EDS analysis are shown in figure 29. The first thing to notice is that EDS indicates Cu_2O below the
cauliflower structures as indicated by the red-green (yellow) color in the bottom part of both EDS images.
However, inside the cauliflower, variations in Cu and O densities are observed. Metallic Cu is assumed to
dominate in areas of high Cu concentrations in conjunction with low O concentrations, and hence Cu_2O is
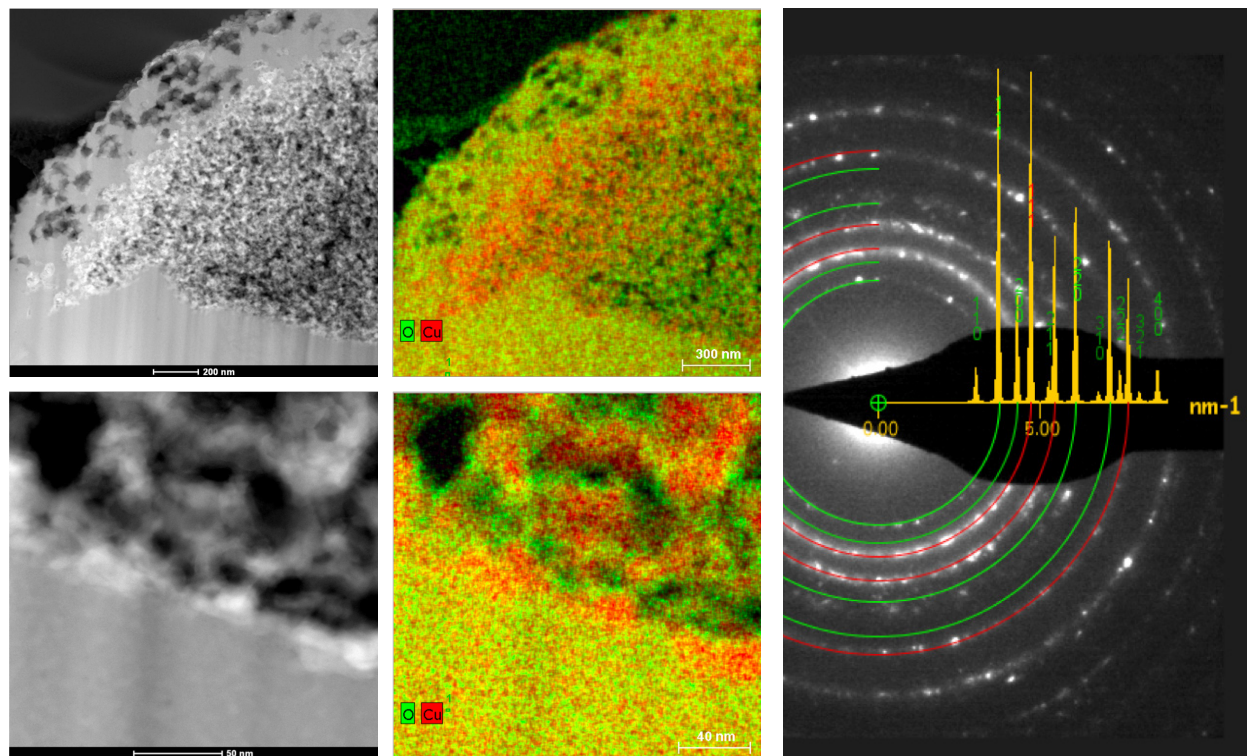
figure 29: HAADF (right) and EDS analysis (left) of the
cauliflower structures on sample 2.

figure 30: XRD of the cauliflow-
er structure. Green lines are Cu_2O
and red lines are metallic Cu.

presumed dominant in areas of high O content. The dark spots are accredited to voids in the structure.

In figure 30, the XRD pattern of the cauliflower structure is shown, confirming a significant amount of metallic Cu in the cauliflower structure, and this backs up the assumption that the Cu-rich areas are regions of metallic Cu.

This mixture of phases and unordered structure indicate that Cu_2O and Cu might be competing for nucleation and growth during the potential oscillations. Even if STEM is not a statistical method (i.e., looking at a very limited area), the cauliflower structure examined show layering of dominant species; however, the distinct layering shown by Switzer et al. [44] is not seen. The TEM results presented by Leopold et al. [45] are quite similar to that found in this work, and the same porous structure and small grain size are observed.

As earlier discussed, metallic content in the structure deteriorates Cu_2O performance, and efforts were therefore directed at avoiding the spontaneous potential oscillations during deposition. Two methods were utilized in an attempt to prevent these oscillations:

1. Keep the solution temperature stable at a level where OH^- ions are mobile enough to sustain the concentrations needed for Cu_2O deposition at the cathode.

2. Use low deposition currents to maintain an electrode potential of no more than $\sim$ -1.1 V vs. V_{ref}, resulting in sufficiently low deposition rates and hence never let the OH^- concentrations at the electrode surface reach a deficit.

To achieve the first point, a transition from controlling solution temperature by a heat plate to a circulating water bath was made, introducing a higher level of temperature control and a more uniform temperature throughout the deposition electrolyte. The enhanced temperature control, in combination with greater insights as to what potentials facilitate oscillations in the system (second point), resulted in highly reproducible depositions free of oscillations as seen in figure 31.
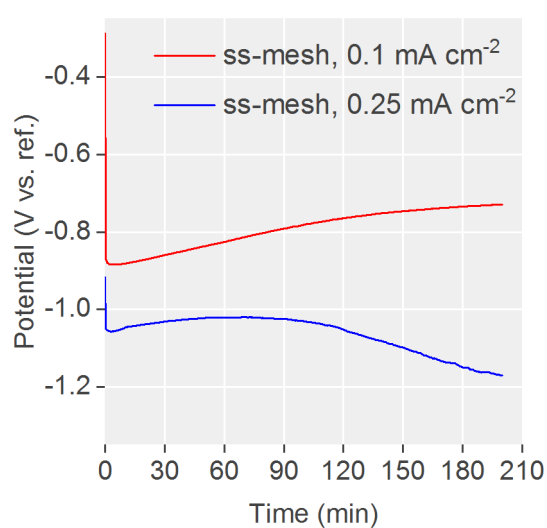

figure 31: Galvanostatic electrodeposition on ss-mesh at 0.1 mA cm^{-2} and 0.25 mA cm^{-2} employing a double walled beaker to control deposition temperature (right).

5.1.2   Materials Characterization of Cu$_2$O

Scanning Electron Microscopy

SEM was used to determine surface coverage and morphologies with the aim of establishing the best-suited substrate for depositing samples for subsequent use in SS-PEC cell. Examples of SEM results are shown in figure 32.

Grain sizes in samples deposited on C-paper were typically smaller (< 0.1 μm to 2 μm) than those on ss-mesh, as were grain sizes in samples deposited on Ti-mesh, although a few large grains (~ 5 μm) are visible
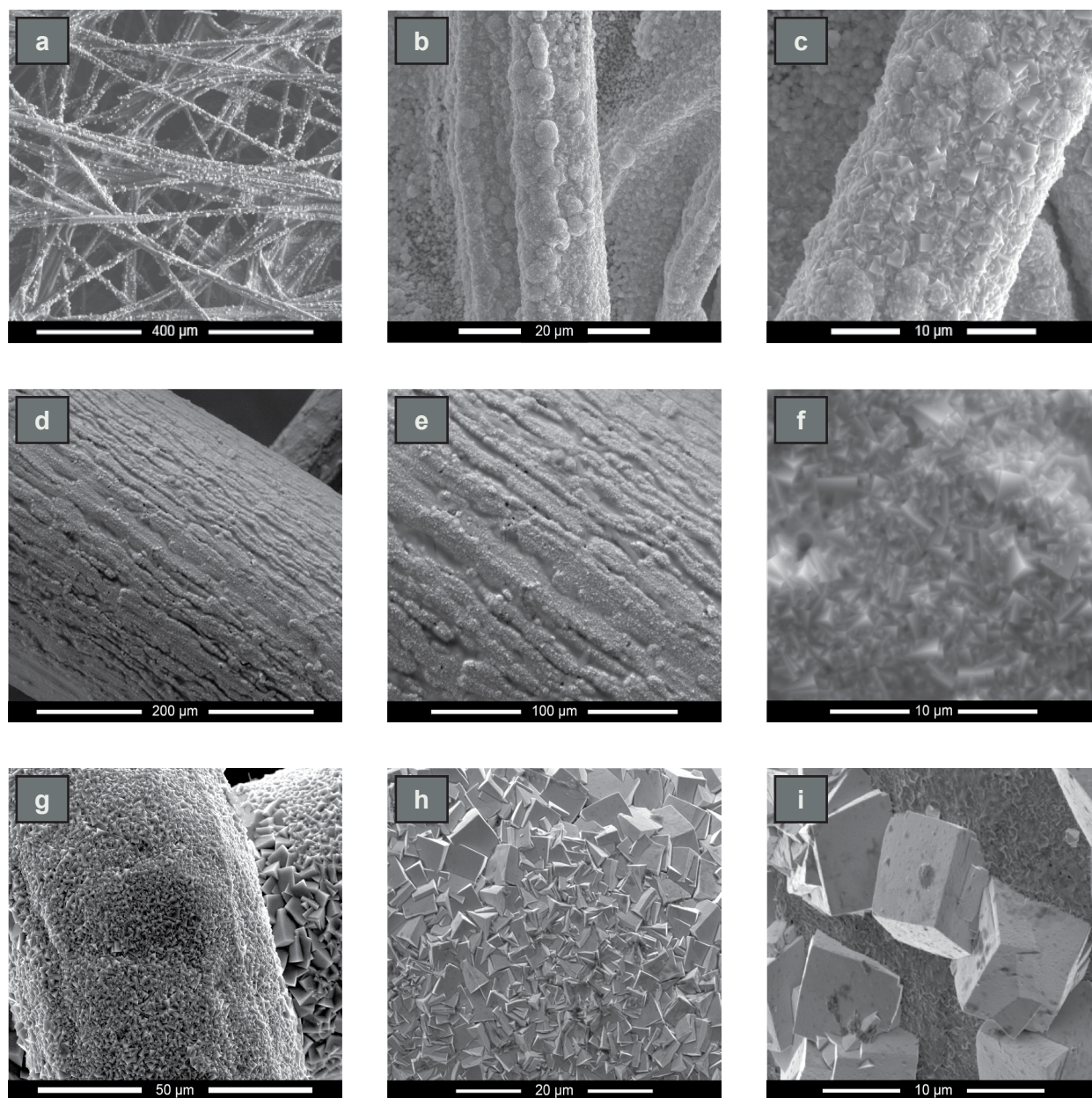
figure 32: SEM images of Cu$_2$O on C-paper substrate (a-c) (working distance (WD) 11 mm, acceleration voltage 15 kV, ETD detector), Ti-mesh substrate (d-f) (working distance (WD) 10.3 mm, acceleration voltage 20 kV, ETD detector) and ss-mesh substrate (g-i) (working distance (WD) 10, 9.8, 9.4 mm, acceleration voltage 20, 5, 2 kV, ETD detector).

in these. On ss-mesh samples, grains were typically in the 2 to 5 μm range.

C-paper depositions produced areas of only partial coverage as seen in figure 32 (a), a likely reason for the low photocurrents later discussed. The Ti-mesh samples generally had good surface coverage but seemed to have longitudinal cracks and less consistent coverage than, e.g., the ss-mesh. The ss-mesh substrate showed close to perfect coverage of polycrystalline Cu_2O with the most uniform grain size.

SEM was used to investigate a wide range of samples, and while samples deposited on ss-mesh exhibited the most consistent results in general; one reason why it was chosen as the preferred substrate for further work.

SEM was also used to determine the thickness of the deposited material on the ss-mesh substrate. In figure 33, a side view of a galvanostatically deposited sample shows that the thickness of the deposited poly-crystalline Cu_2O varies significantly across the surface, with a thickness in the 1-3.5 μm range. This thickness was the result of a 220 min galvanostatic deposition at -0.25 mA at 30°C.
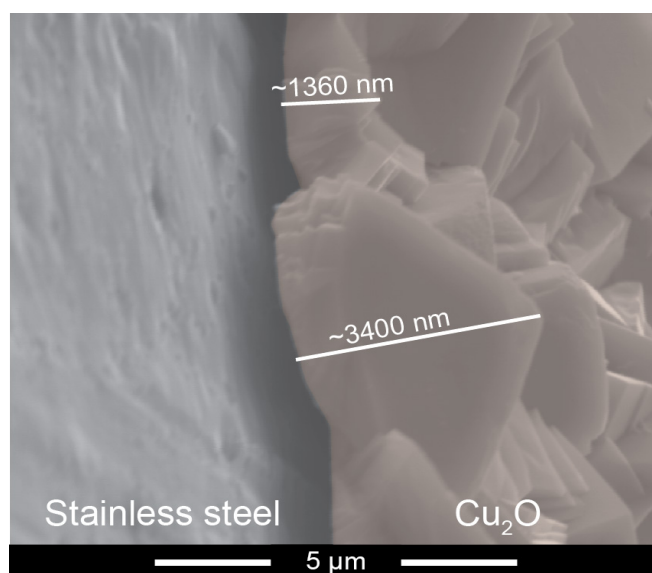
figure 33: Side view of Cu_2O galvanostatically deposited at -0.25 mA for 220 min at 30°C. Colors added for contrast.

Scanning Transmission Electron Microscopy

STEM was used to study the crystallinity and microstructure of deposited samples. Annular bright field (ABF) and annular dark field (ADF) were used to examine the stress and strain in the structure, while HAADF was used to investigate the composition of the studied area. A selection of the resulting images are provided in figure 34.

The images show an apparent tendency for columnar crystal growth perpendicular to the surface of the substrate. The sample in figure 34 is approximately 1 - 2 μm thick. The difference in contrast in the ABF and ADF images indicate that these columns are highly strained structures with a high concentration of dislocations; an indication of fast crystal growth during deposition. It is known that single crystal Cu_2O reduce to metallic Cu in aqueous solution under illumination; however, Hara et al. [70] show continuous water splitting by Cu_2O powders (size: 0.3–0.5 μm, surface area: 6 m^2 g^{-1}) over a period of 1900 h. It is

not clear though, whether the stability of Cu_2O could be increased by decreasing crystal size to match the 0.3 - 0.5 μm powder.

By investigating the HAADF images, it is apparent that the lack of contrast shows that these columnar crystals are highly uniform in composition, indicating low to no Cu metal content. The lower three images of figure 34 show highly crystalline structures at the atomic level with a well aligned atomic structure.
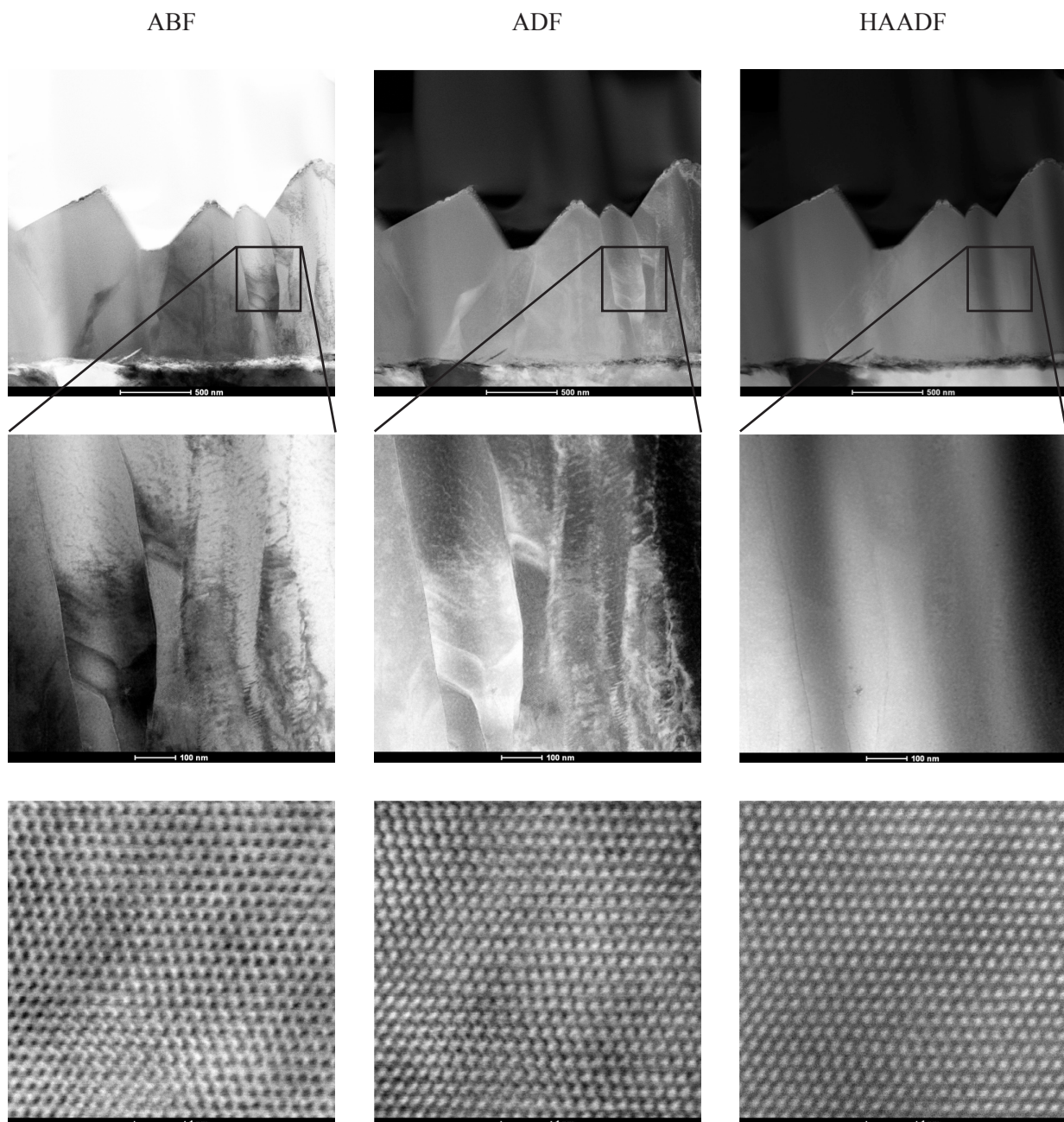

figure 34: STEM images of sample deposited galvanostatically at -0.2 mA on ss-mesh for 100 min at 30°C in pH 12.

X-Ray Diffraction

XRD analysis was performed before and after deposition on all substrates to confirm the Cu_2O phase. The XRD-patterns for the deposited samples on different substrates are presented in figure 35. Only peaks corresponding to Cu_2O, or the substrates, was observed in samples before illumination, except in Ti-mesh samples. However, peaks corresponding to the ss-mesh overlap any metallic Cu peaks, and it is therefore not possible to confirm that the ss-mesh samples do not contain metallic Cu. Hence, it is concluded that Cu_2O were successfully deposited on all substrates, and that metallic Cu are present in samples deposited on Ti-mesh and. On samples deposited on ss-mesh substrates, the presence of metallic Cu cannot be ruled out due to the overlapping 2θ angles matching the substrate.

XRD scanning parameters had to be optimized to achieve good results with the ss-mesh samples. Materials with high Fe-concentrations produce a lot of background noise and require the Rigaku XRD instrument to be used in 'XRF-mode.' Hence, comparisons of intensities and other quantitative methods between the substrates were not performed.
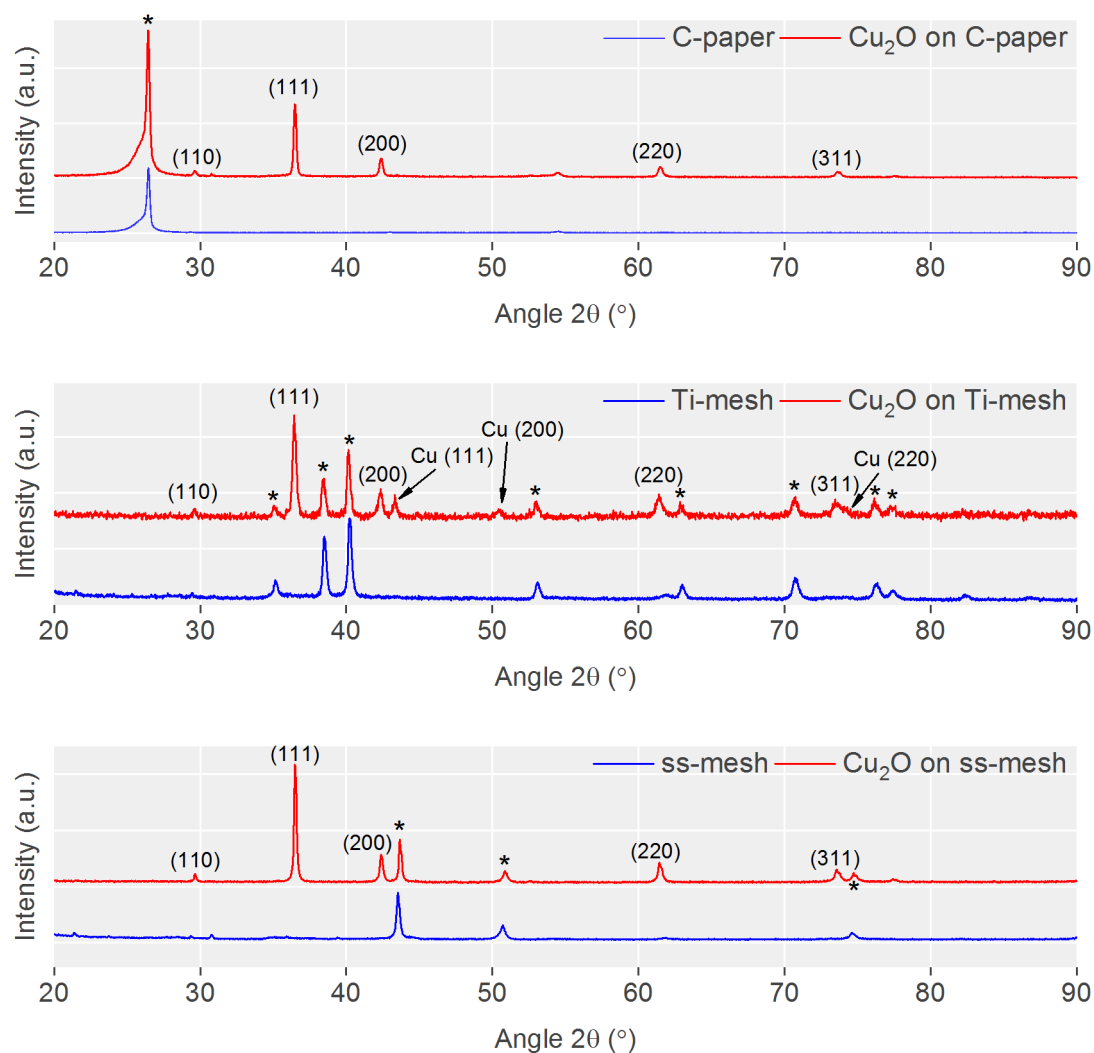

figure 35: XRD plots of substrates and Cu_2O on the respective substrate. '*' indicate substrate reflections. Metallic Cu reflections are labeled 'Cu(...)', while Cu_2O reflections are labeled '(...)'.

5.1.3 Photoelectrochemical Characterization

To compare results of different substrates and again compare these with the work of others, a rough normalization of electrode area was conducted. To normalize the electrode area in *dark* measurements, both front and back were treated as active areas, while only the illuminated side of the electrode were treated as active during *light on* measurements

$$A_{\text{el, dark}} = 2A_{\text{nom}} \times (A_{\text{norm}}) \qquad (5.38)$$

$$A_{\text{el, light}} = A_{\text{nom}} \times (A_{\text{norm}}) \qquad (5.39)$$

where A_{el} is the exposed electrode area, A_{nom} the nominal electrode area, and A_{norm} the calculated normalized area from table 3. The measured values in dark were divided by $A_{\text{el, dark}}$, and measurements in light divided by $A_{\text{el, light}}$.

Open Circuit Potential

OCP was conducted to establish the photovoltage, V_{ph}, of the deposited samples. The results are shown in figure 36. The plots show that the mean potential of the system shifts ~80 mV more positive over the measurement period, probably due to chemical surface passivation of Cu_2O, and possibly leading to a CuO surface.

By extrapolating two lines along the potentials measured in light (green line figure 36 (left)) and dark (blue line figure 36 (left)), it was possible to find the photovoltage development over time by extracting the absolute value between the two. The resulting photovoltage, V_{ph}, is shown in figure 36 (right), and shows a decreasing V_{ph}, dropping from 35 mV to 14 mV over a period of 3 hours (1.5 h illumination). The drop in
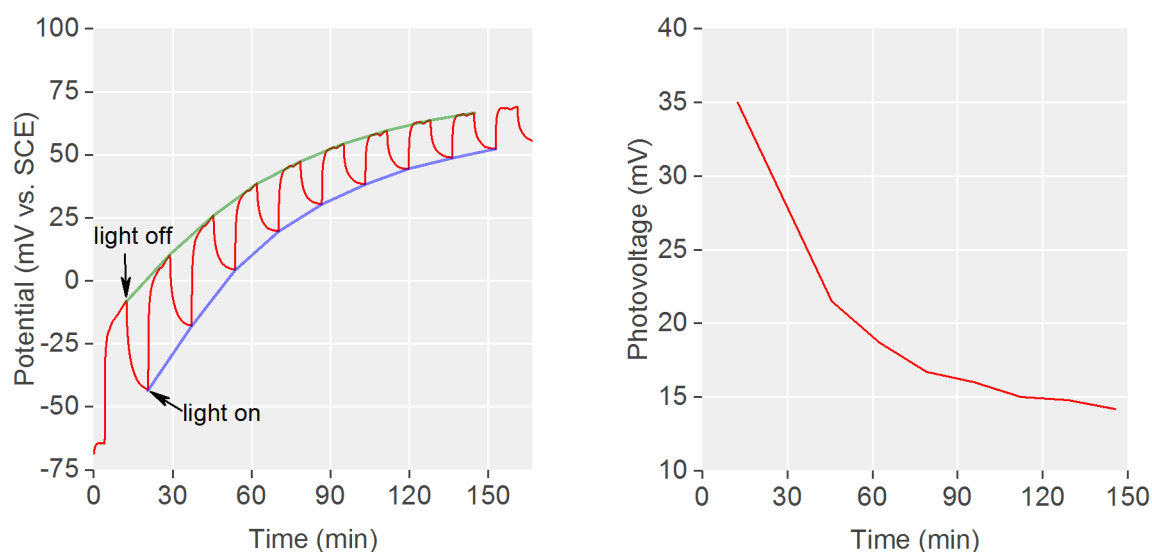

figure 36: OCP of Cu_2O sample deposited at -0.2 mA for 220 min at 30°C (left). Calculated photovoltage (right) from the difference between potentials measured in dark (blue line, extrapolated) and potentials measured in light (green line, extrapolated) Each cycle consist of 500 s light on and 500 s light off.

V_{ph} is also assumed to be a result of the chemical passivation of the surface by the $NaSO_4$ solution, and not due to the reduction of Cu_2O to metallic copper.

After running OCP for 3 hours, the photocurrent was investigated by linear sweep voltammetry (LSV) as shown in figure 37. The photocurrent, J_{ph}, was found by subtracting the normalized values during the dark (dark run 1, 2) from the normalized values during illumination (light run 1, 2). The sample exhibited a photocurrent, $J_{ph} = 126$ µA cm^{-2} at -0.6 V vs. SCE on the first illuminated LSV measurement (light run 1) after OCP, while the second illuminated LSV measurement (light run 2) showed $J_{ph} = 68$ µA cm^{-2} at -0.6 V vs. SCE.
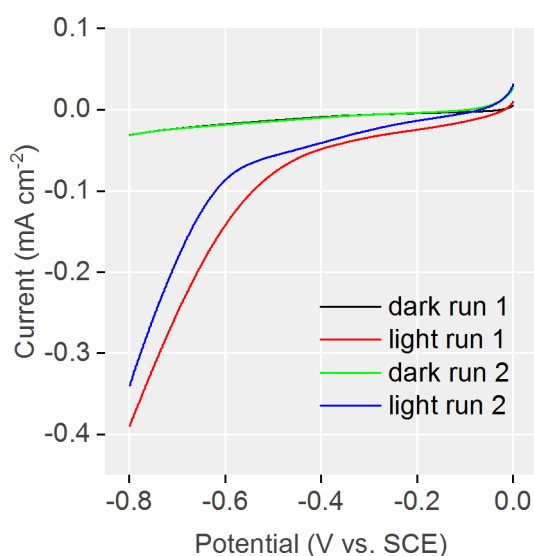
figure 37: LSV measurement of sample deposited at -0.2 mA for 220 min at 30°C after 3 h of OCP with 500 s light on/off.

A photocurrent of 126 µA cm^{-2} is, as later shown, amongst the worst Cu_2O electrodes measured in this work. If the bad performance is due to passivation of the surface during OCP, or that it is just not an optimized electrode from the start is unclear. Measuring the sample by LSV before OCP would deteriorate the sample, and OCP values would not be realistic.

On the basis that the surface change over time in OCP measurements, it is assumed that the actual photovoltage of the Cu_2O sample measured is found by using the values at the start of the measurement before surface passivation evolves, hence $V_{ph} \sim 35$ mV.

Linear Sweep Voltammetry

LSV measurements have been used in this work to study photocurrents of deposited electrodes. Photocurrents were determined by subtracting dark currents from currents obtained during illumination. The photocurrent at -0.6 V vs. SCE was chosen as the reference point as this falls close to 0 V vs. RHE[1].

Resulting LSV measurements are shown in figure 38 and show the calculated photocurrent for all sub-

---

[1]   From the equation $E_{RHE} = E_{ref} + 0.059$ pH $+ E^0_{ref}$, SCE $= +0.241$ V vs. SHE, pH of 0.5 M $NaSO_4 = 5.6$

strates, in addition to the currents measured in the dark and during illumination (blue and red, respectively). To gain a better understanding of the performance of the different substrates, a statistical analysis was performed collectively on all the measured samples. The results of these calculations are compiled in figure 39. The thin black vertical line indicates the total spread in the measured values. The green box shows an area that excludes values below 25%, or above 75%, of the mean value of the set. The mean is the mean value of all samples in the set, and the median line indicates the median value of the set. Five samples on c-paper, two samples on Ti-mesh, and seven samples on ss-mesh make up the sets.

This analysis shows that C-paper samples had the lowest mean photocurrent of -0.14 mA cm^{-2}, Ti-mesh samples had a mean photocurrent of -0.24 µA cm^{-2} and the ss-mesh samples a mean of -0.41 mA cm^{-2}; the top performing ss-mesh electrode showing a photocurrent of -1.11 mA cm^{-2}; this electrode was deposited galvanostatically at -0.1 mA for 120 minutes at 30°C.
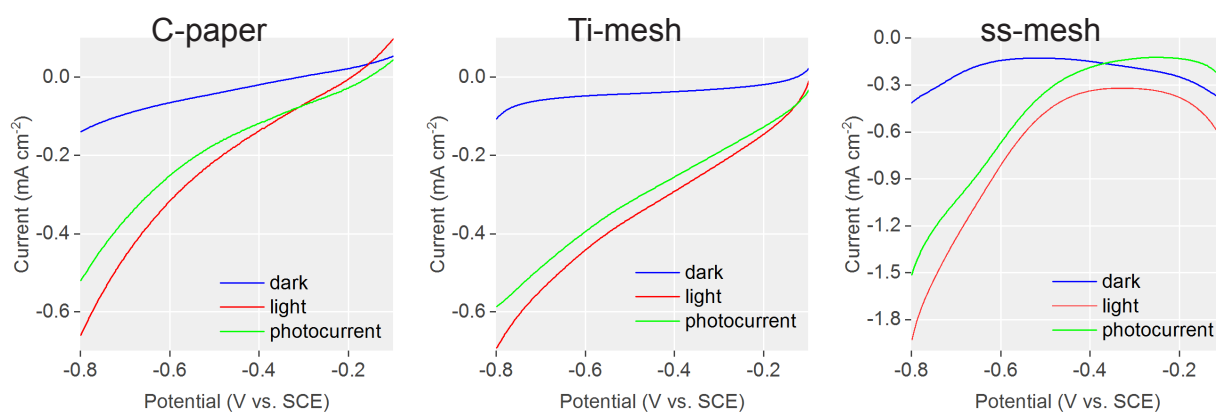

figure 38: LSV of Cu$_2$O galvanostatically deposited on the different substrates at -0.1 mA for 120 min at 30°C.
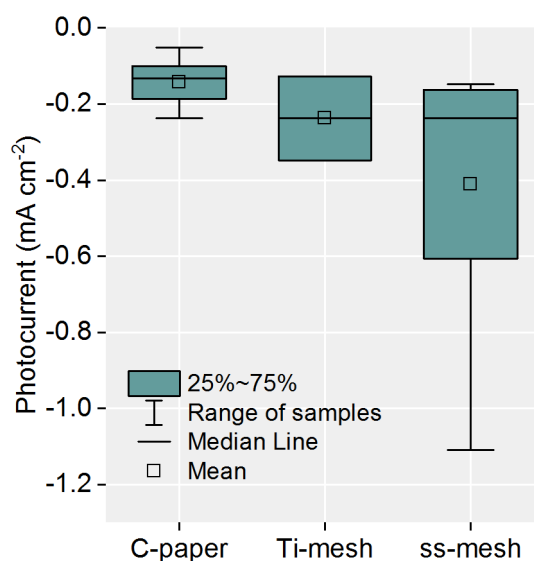

figure 39: Comparison of substrates with respect to photocurrents at -0.6 V vs. SCE. The negative sign indicating cathodic currents as appropriate for a p-type semiconductor.

Chronoamperometry

CA is used in this work to establish the photodegradation of Cu_2O during illumination in an aqueous solution. By applying a constant potential to the Cu_2O electrode, the current is measured and recorded as in figure 40. 10 s of illumination succeeds 10 s of dark measurements to confirm that the sample is photo-active. The potential is set to -0.6 V vs. SCE in all measurements.

The mean photocurrent of the first light-on cycle was calculated to be -0.83 mA cm^{-2}, and to quantify the degradation, an arbitrarily chosen value of 15% (-0.12 mA cm^{-2}) of the initial photocurrent was used. This value is indicated by the black line in figure 40. It was derived that the sample measured in figure 40 degrades to 15% of the initial photocurrent (black line) within ~700 s of measurement[2]; this equals ~350 s of illumination, an indication that Cu_2O does, in fact, degrade fast under these conditions.
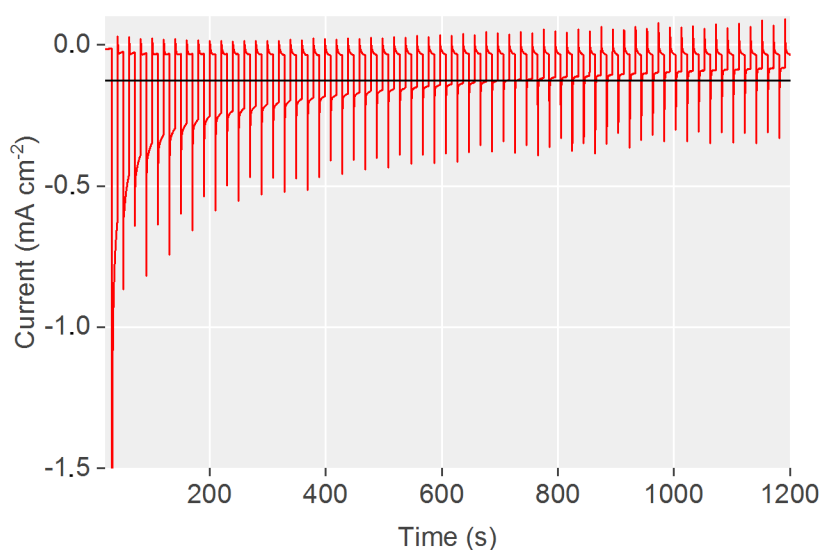

figure 40: CA of Cu_2O sample deposited on ss-mesh at -0.6 V vs. SCE. Sample deposited at -0.25 mA for 100 min at 30°C. Black line indicating 15% of initial photocurrent.

TiO₂ Protective Layer

With the aim of stabilizing the Cu_2O electrode, the surface was coated with a layer of TiO_2 by PLD. Previous studies have shown that TiO_2 deposited by ALD can increase performance and, in conjunction with other materials, stabilize the Cu_2O cathode. Two sets of two samples were deposited, equal in deposition parameters[3], one reference and one for TiO_2 coating in each set. The deposition parameters used here are not those found to produce the best electrodes, but chosen for effiency and reproducability; hence, photocurrents in bare samples are not top of the line. One additional sample (same parameters) was deposited to be investigated by STEM and EDS for structural and compositional analysis, and the results are shown in figure 41. In the area investigated, a thin uniform layer of TiO_2 is observed on top of crystalline Cu_2O, and EDS analysis determined this layer to be approximately 20 nm thick. However, figure 41 (c) shows no indication of crystalline TiO_2, and it is concluded that the deposited TiO_2 layer is amorphous in nature.

---

2   Assuming constant dark current values
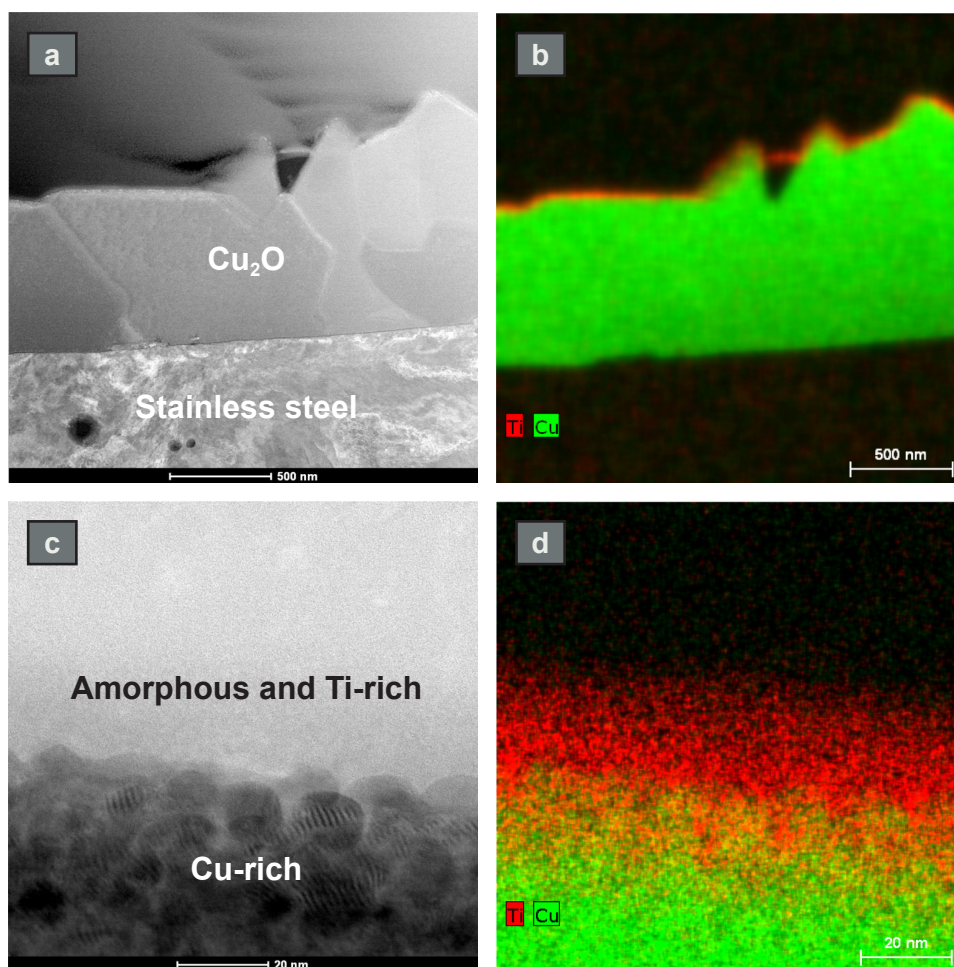
3   -0.25 mA for 100 min at 30°C on ss-mesh.

figure 41: ADF-STEM (left) and EDS images (right) of Cu_2O samples galvanostatically deposited on ss-mesh (-0.25 mA, 100 min, 30°C) with a TiO_2 layer on top, deposited by PLD (5000 laser pulses of 30 mJ cm^{-2}, frequency 5 Hz, 100°C, Ar-atmosphere)

The CA measurements were conducted in a 0.5 M $NaSO_4$ electrolyte using a three-electrode setup as described in the methods section. The light source was set to operate on a 10 s light on/off cycle, and the results from these measurements are shown in figure 42. The bare Cu_2O sample shows a mean photocurrent
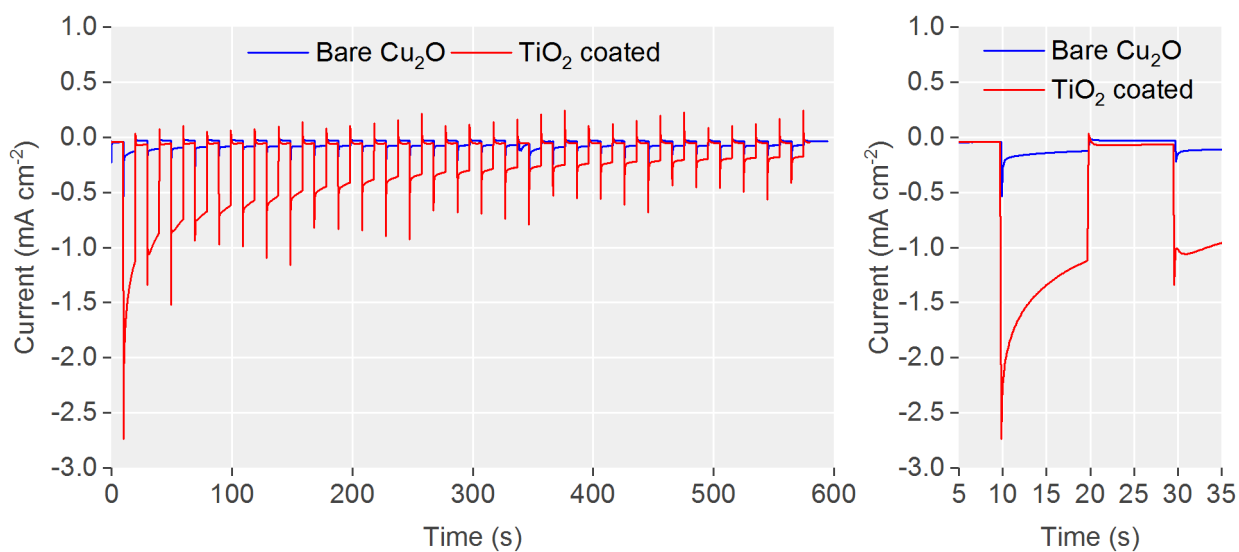

figure 42: CA at -0.6 V vs. SCE of two Cu_2O samples galvanostatically deposited on ss-mesh at -0.25 mA for 100 min at 30°C, both bare and covered with TiO_2 by PLD.

during the first light-on cycle of J_{ph} = -0.12 mA cm^{-2}, while the TiO$_2$ covered sample shows a photocurrent of J_{ph} = -1.38 mA cm^{-2}, at -0.6 V vs. SCE. This result was reproduced on the second set of samples, and it is therefore concluded that PLD deposited TiO$_2$ have a significant effect on the photocurrent of Cu$_2$O photoelectrodes.

However, stability is still poor, and as previous works have shown, TiO$_2$ alone is not able to stabilize the Cu$_2$O electrode. The last cycle of the TiO$_2$ covered sample shows a photocurrent of -0.12 mA cm^{-2} after a total of 280 s of illumination; less than 10 % of the initial photocurrent. An even faster degradation of performance is observed compared to the sample shown in figure 40; the photocurrent falls to -0.12 mA cm^{-2} after 280 s of illumination in the TiO$_2$ covered sample, while the bare sample (reported in figure 40) drops to -0.12 mA cm^{-2} after 350 s of illumination.

The increased photocurrent is assumed to be a result of an enhanced electron-hole separation mechanism arising from the band structures of the two phases (assuming n-type TiO$_2$) and the interface that forms when they come in contact, as proposed in figure 43. After the two phases come in contact and align Fermi-levels, electrons have an energetically favorable route into the TiO$_2$, and subsequently the semiconductor-electrolyte interface, while holes go to Cu$_2$O bulk.
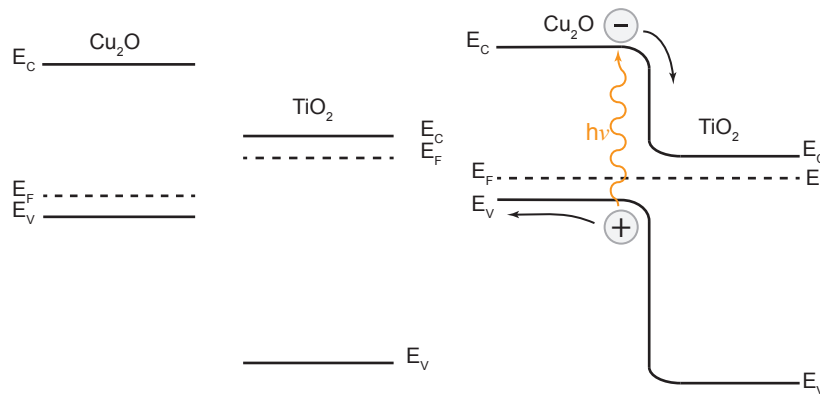

figure 43: Schematics of proposed electron hole separation mechanism by formation of a p-n-junction between the Cu$_2$O electrode and TiO$_2$ layer.

5.2   Solid State Photoelectrochemical Cell

As stated in the introduction the main hypothesis to be tested in this project is whether Cu$_2$O will remain stable under dry conditions in a SS-PEC cell or not. To test this hypothesis, cells were prepared as discussed in methods and measured by OCP and CA to establish photovoltage and photocurrent values, respectively. CA was additionally used to investigate the stability of the system.

Two different cell configurations were prepared using Cu$_2$O as a photocathode: one cell with Pt-C electrocatalyst on C-paper operating as photoanode, and one with anodized TiO$_2$. In the first case (a) and (b) the Cu$_2$O electrode was defined as the working electrode, i.e., measured potentials are that of Cu$_2$O with respect to the reference, Pt-C. In the latter, TiO$_2$ was defined as the working electrode, and Cu$_2$O was acting as the reference electrode. The anode side of the cell was always provided with wet Ar gas, while the

cathode side (Cu_2O side) was kept dry with dried Ar at all times. An initial period of 2-4 hours of flushing the system with gas was implemented before electrochemical measurements.

Results from the OCP measurement for the Cu_2O/Pt-C-cell are shown in figure 44 a) and b), and the Cu_2O/TiO_2-cell is shown in figure 44 c) and d). Both measurements use a 60 min light off/on cycle with the aim of establishing a photovoltage for the two systems. However, as the figures show, no apparent equilibrium was reached in the measurement intervals used, but certain trends appear, and these are used to gain some understanding of the photovoltages in the system.

The Cu_2O/Pt-C-cell shows two trends, one for light on and one for light off, and can aid in extracting a photovoltage. When the light is turned on, a spike in potential towards more positive values is observed, which is typical and expected when using a p-type electrode material. However, the potential drops back
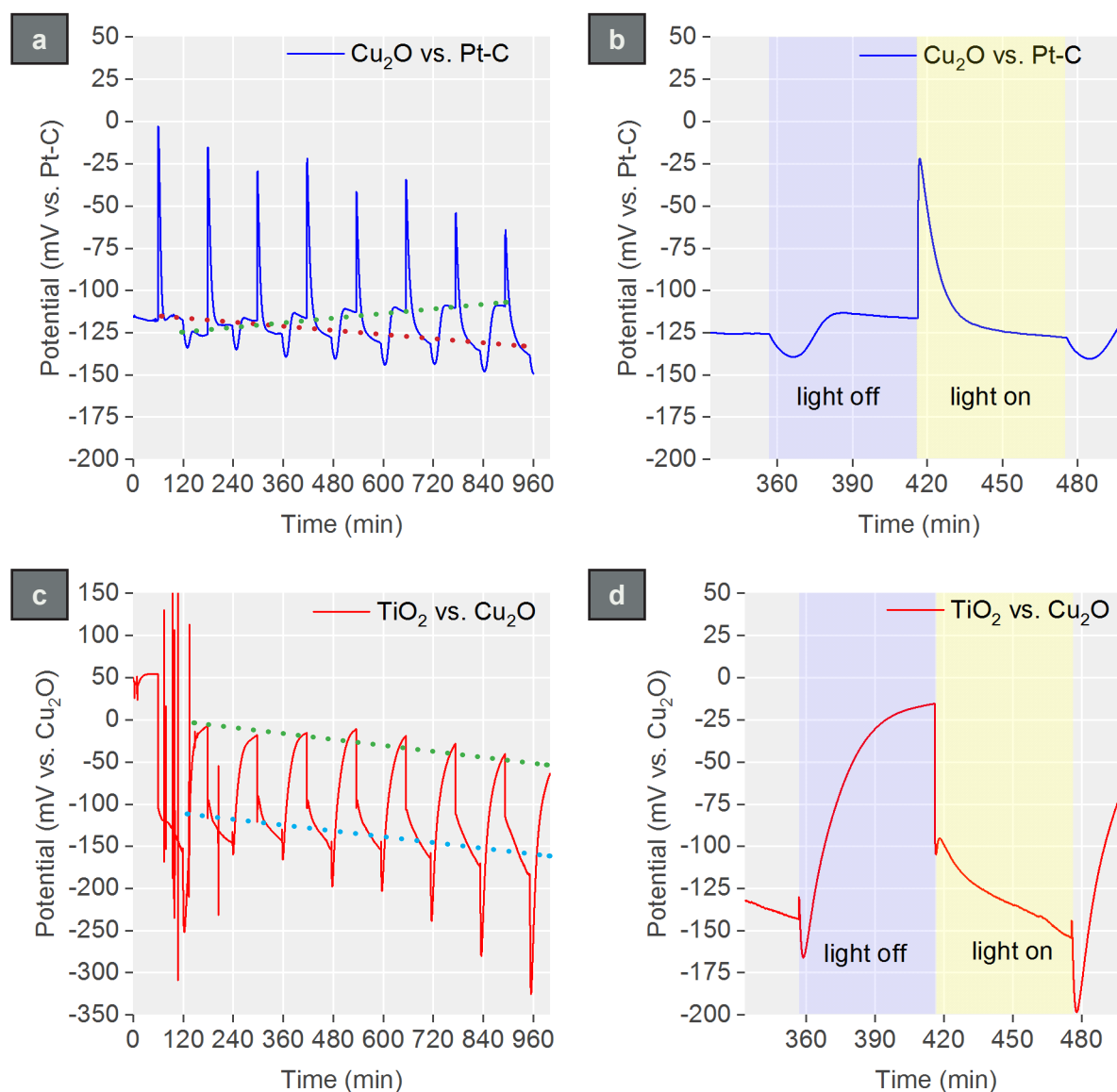

figure 44: OCP of SS-PEC cell using galvanostatically deposited Cu_2O (-0.2 mA for 220 min at 30°C) as photocathodes. Pt-C electrocatalyst on C-paper (a-b) and anodized TiO_2-mesh (c-d) employed as photoanodes. Cu_2O is always defined as the working electrode. Cu_2O is illuminated (Pt-C electrode acting as the back electrode) in figure a and b, while TiO_2 is illuminated in figure c and d (Cu_2O serving as the back electrode).

to more negative values within ~20 min, showing that the Cu_2O photocathode is not able to sustain the charge set up by illumination. If this quasi-plateau is taken as the OCP value of light on (red dotted line in figure 44), it is seen that the light OCP values shift towards more negative values over time, while the dark OCP values (green dotted line in figure 44) shift to more positive values. Using these trends, steady-state photovoltages (difference in green and red trend line) range from approximately +10 mV to -25 mV over the measurement period. A much higher photovoltage arises if the peak values of light and dark are used, ranging from approximately +75 mV to +120 mV.

The Cu_2O/TiO_2-cell also shows trends for light on and light off, indicated by blue and green lines in figure 44, respectively. If these trends are used as a measure for photovoltage values, no apparent change in photovoltage over the period of measuring was observed, and remain constant at approximately -110 mV. The negative sign is consistent with the fact that n-type TiO_2 is defined as working electrode. However, the system as a whole shifts to more negative potentials, and this might be the same effect as discussed earlier, i.e., chemical passivation of the Cu_2O electrode. In this setup, Cu_2O acts as the reference electrode and a shift toward more negative values are in line with the results seen when measuring OCP in a three electrode system. The reason for the chemical passivation of Cu_2O is probably because the electrode is immersed in Nafion®, an acidic medium.

After OCP was performed on the $Cu_2O/Pt-C$-cell, LSV was used to investigate any photocurrents in the cell. As shown in figure 45, a small photocurrent was detected when operated at -2.0 V vs. SCE; the first cycle showing J_{ph} = -1.5 µA cm^{-2} and the last cycle showing J_{ph} = -0.8 µA cm^{-2}. The shift towards more negative currents during illumination is what we expect to see at the Cu_2O electrode, as it is p-type and cathodic currents arise as a result. It is also apparent that photodegradation of the Cu_2O cathode occurs, as the drop in J_{ph} from the first cycle to the last, after ~1800 s illumination, is approximately 50% of the initial
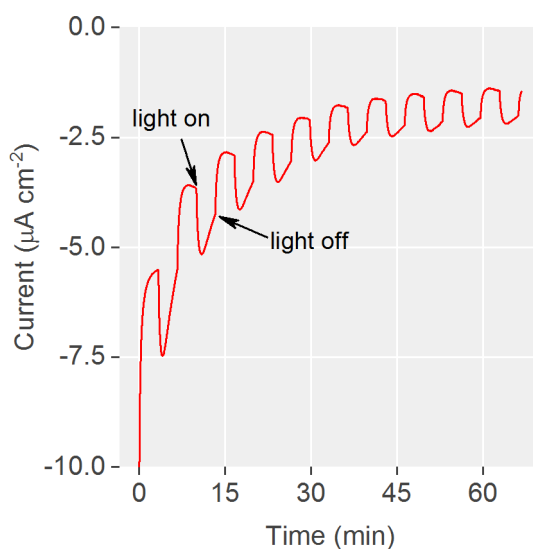

figure 45: CA of SS-PEC cell using galvanostatically deposited Cu_2O (-0.2 mA for 220 min at 30°C) as a photocathode and Pt-C electrocatalyst on C-paper as photoanode. The illuminated front electrode is Cu_2O. Cu_2O defined as the working electrode. Measured at -2.0 V vs. Pt-C using a 200 s light on/off cycle.

value. This drop in photocurrent is much smaller than the drop observed during measurements in aqueous solutions; however, the currents are also much smaller. As the reduction of Cu_2O to metallic Cu are electrochemical, a low current will equal a low reduction rate. It is therefore concluded that the Cu_2O electrode experience degradation even when it is operated in a dry atmosphere, and possibly to the same extent.The reduction is attributed to the fact that as protons are supplied to the Cu_2O photocathode, the energetically favourable reduction is

$$Cu_2O + 2e^- + 2H^+ \rightarrow Cu + H_2O$$

rather than

$$2H^+ + 2e^- \rightarrow H_2$$

LSV was also attempted with the Cu_2O/TiO_2-cell, but no photocurrent was detected, even if a photoresponse was shown by OCP. This is probably due to the fact that the TiO_2 mesh was immersed entirely in Nafion®, prohibiting any atmospheric water to react at the electrode surface.

5.3   Fabrication and Characterization of Delafossite Electrodes

In an effort to find new and more suitable materials for HER PEC cell operations, delafossite ($CuFeO_2$) was chosen as a suitable candidate. According to literature, $CuFeO_2$ has a smaller bandgap (~1.5 eV) than Cu_2O, which means that it can utilize a greater part of the incident sunlight, and it is highly stable in aqueous solutions under illumination, and prolonged operation in PEC cell operations is therefore possible. With a well situated CBM for HER, $CuFeO_2$ has the potential to act as a high-performance photocathode for HER in PEC cells. However, as discussed in the literature section, the materials properties are highly dependent on deposition method and parameters. It is therefore essential to gain a better understanding of deposition parameters, and this section seeks to investigate this subject.

Electrodeposition was chosen as the preferred method for deposition due to its simplicity, low energy consumption and ease of scalability. Subsequent structural and electrochemical characterization was performed to establish materials properties and PEC suitability. This section presents the results from the experimental work done on $CuFeO_2$, with a subsequent discussion of these results.

5.3.1   Electrochemical Deposition of $CuFeO_2$

Electrochemical deposition of $CuFeO_2$ was conducted according to the procedure described in the methids section on FTO substrates. FTO was chosen as a substrate to obtain comparable results to other works on $CuFeO_2$, where FTO have been used as a substrate for electrochemical deposition.

A typical current vs. time curve resulting from deposition at -0.6 V vs. Ag/AgCl$_{sat}$ is shown in figure 46. The resulting films were dark yellow to brown with uniform coverage, but this result only appeared when doubling the concentration of $Fe(ClO_4)_3$ in the solution from 0.005 M to 0.01 M. At 0.005 M $Fe(ClO_4)_3$

little to no material was observed on the FTO substrate. Even after the concentration of $Fe(ClO_4)_3$ was increased to 0.01 M, EDS analysis was not able to establish the presence of Fe in the as-deposited films.

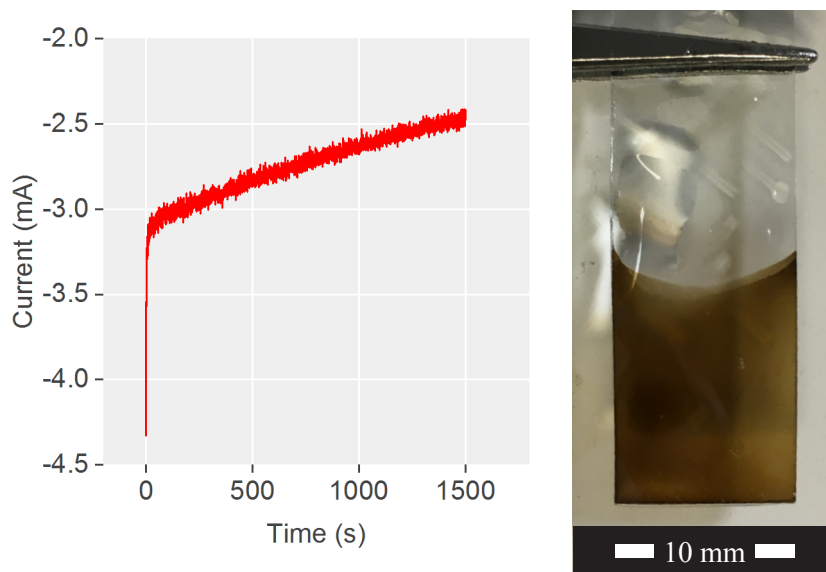**figure 46:** Potentiostatic deposition of $CuFeO_2$ from a 0.01 M $CuCl_2$, 0.01 M $Fe(ClO_4)_3$, 0.1 M $LiClO_4$ DMSO electrolyte at 50°C for 1500 s (left) at -0.6 V vs. $Ag/AgCl_{sat}$, and a digital image of the resulting film on FTO (right).

5.3.2 Materials Characterization of CuFeO₂

XRD

XRD analysis was conducted to establish the as-deposited composition and crystallinity, and if annealed samples exhibited crystalline $CuFeO_2$. The results from this XRD analysis are given in figure 47 and show that the distinct peaks that arise from the FTO are found in both pre- and post-annealed samples. The
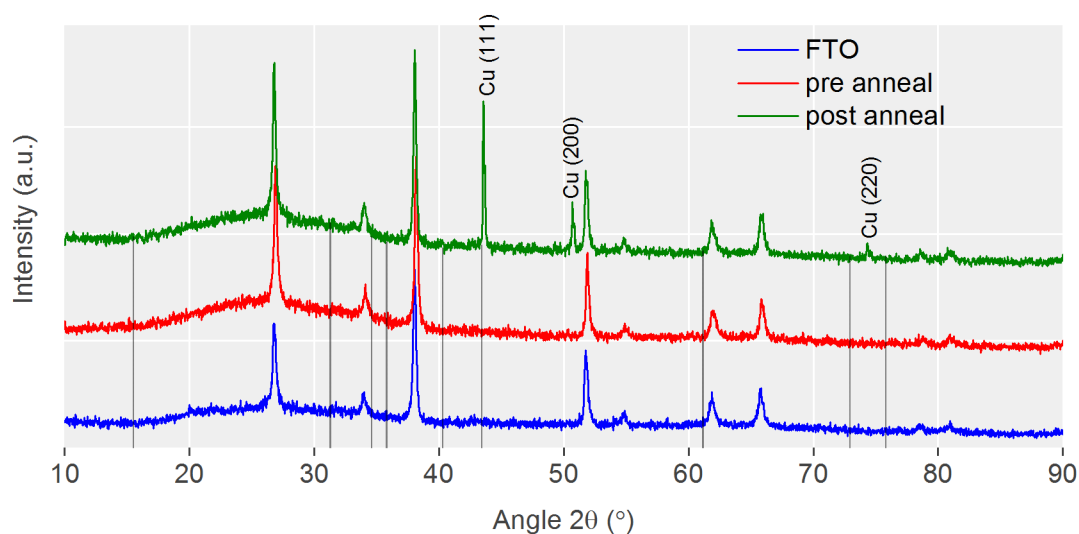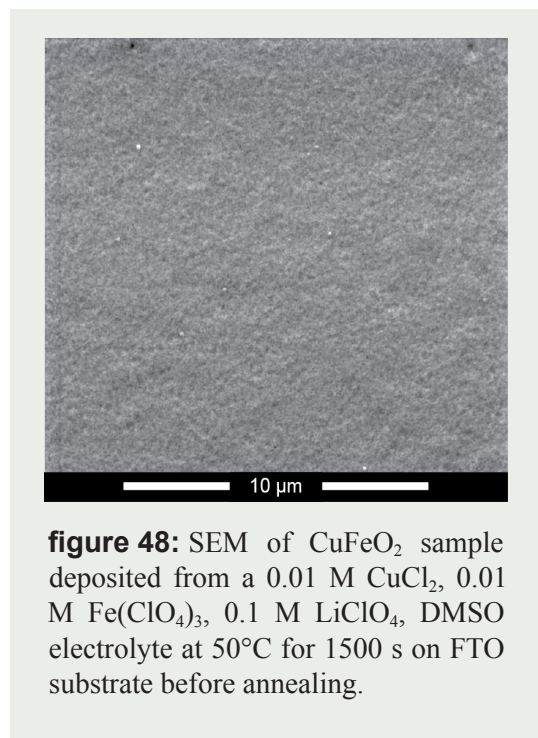

figure 47: Results from XRD analysis of FTO substrate, $CuFeO_2$ sample on FTO before annealing and $CuFeO_2$ sample on FTO after annealing. Gray verticle lines indicate $CuFeO_2$ 2θ angles, while the three reflection planes of metallic Cu are shown on their respective peaks.

pre-annealed sample shows no signs of crystallinity, and it is thus concluded that the as-deposited samples are amorphous in nature. After annealing at 650°C for 30 minutes, three new peaks appear; peaks ascribed to metallic copper. No $CuFeO_2$ peaks are present in the XRD spectrum shown in figure 47 ($CuFeO_2$ Bragg planes indicated by gray vertical lines) nor is Cu_2O or Fe_2O_3 peaks; only peaks attributed to the substrate is observed in the annealed sample.

Scanning Electron Microscopy

Before the samples were annealed, SEM was used to study the as-deposited film morphology as shown in figure 48. SEM investigations showed a featureless surface, consistent with the XRD results where it concluded that the as-deposited film was amorphous in nature.

figure 48: SEM of $CuFeO_2$ sample deposited from a 0.01 M $CuCl_2$, 0.01 M $Fe(ClO_4)_3$, 0.1 M $LiClO_4$, DMSO electrolyte at 50°C for 1500 s on FTO substrate before annealing.

After the sample was annealed at 650°C for 30 minutes, the sample was again investigated in the SEM. As seen in figure 49, the surficial structure has changed during annealing and the material agglomerate into small quasi-spherical particles on the surface. These particles measure 1 - 3 μm and are spread evenly all over the surface of the samples as shown in figure 49 (a). Close to the edge of where deposited material is found, a greater spread in particle size is seen, in conjunction with less uniform particle coverage, as depicted in figure 49 (c).

To determine the atomic composition of these particles, a EDS spot analysis of the particle was conducted. The results show that these particles contain 100% Cu. With the additional information provided by the XRD analysis of the sample (i.e., the green line in figure 47), it is concluded that these particles are metallic Cu. No evidence of Fe in the underlying film, nor in the particles, was found, by EDS analysis.
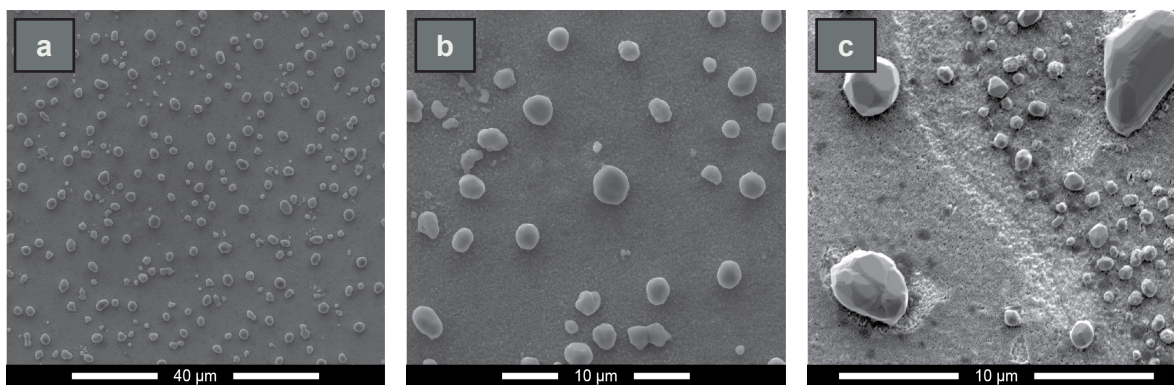

figure 49: SEM of $CuFeO_2$ sample deposited from a 0.01 M $CuCl_2$, 0.01 M $Fe(ClO_4)_3$, 0.1 M LiClO$_4$, DMSO electrolyte at 50°C for 1500 s on FTO substrate after annealing at 650°C for 30 min.

The reason for not observing any Fe in the films, neither before or after annealing, is most likely due to the wrong deposition parameters for Fe_2O_3-deposition, and that the reducing conditions during annealing reduce Cu-ions to metallic Cu in the absence of Fe-ions.

5.3.3   Photoelectrochemical Characterization of $CuFeO_2$

After XRD and SEM analysis, the samples were tested in a PEC setup for electrochemical characterization. Unfortunately, non of the samples exhibited any photoresponse or sign of electrochemical activity. It was therefor concluded that the deposition and preparation of $CuFeO_2$ samples failed, most likely due to the wrong deposition potentials for Fe_2O_3 to deposit.

5.4   Calculations of the Electronic Sructure of Cuprous Oxide

The computational experiments aimed to gain a better understanding of the material and compare different functionals for calculating the electronic structure of Cu_2O. First, a comparison between the PBE and the PBE+U functionals was performed, and the electronic structures were compared. The most important parameter in this respect is the bandgap, and the resulting bandgap predictions produced by the two functionals, are given in figure 50. The calculated bandgap by PBE was $E_g = 0.4677$ eV, while PBE+U produced
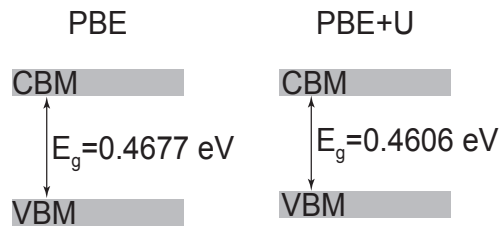

PBE   PBE+U

CBM   CBM

$E_g = 0.4677$ eV $E_g = 0.4606$ eV

VBM   VBM

figure 50: Comparison of bandgap values as calculated by PBE and PBE+U in the Γ-point of Cu_2O.

$E_g = 0.4606$. These results show a slight difference in E_g, but as the system was converged to within 10 meV, uncertainty down to the second decimal means that it is impossible to differentiate the two. Both functionals show a vastly underestimated bandgap compared to experimental bandgap values (2.1 eV). As PBE+U typically predict the bandgap of structures of Cu_2O better than PBE, [80] it was assumed that some unknown factors affected the PBE+U calculations and hence PBE+U was not used for further calculations of the electronic structure.

Calculations of DOS as shown in figure 51 were done using the PBE functional. The VBM is set to 0 eV as per convention, and a small bandgap of $E_g \sim 0.46$ eV is highlighted in the inset of figure 51. The lower states close to -20 eV are the O-2s electron states with a very small amount of Cu-states. The states between -7 and -5 eV are a combination of O-2p and Cu-3d states, with a close to 50/50 mix, while the states from -5 eV to 0 eV are an O-2p/Cu-3d mix with Cu-3d states being highly dominant. This is more
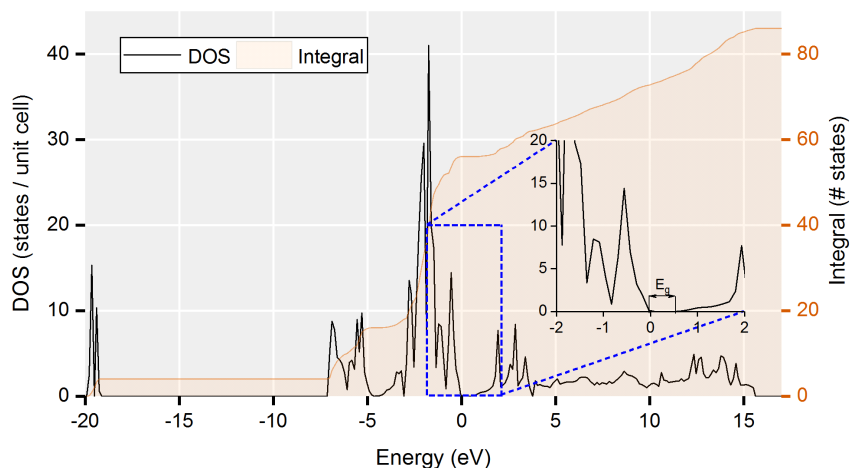
figure 51: Calculation of DOS of Cu₂O using the PBE functional with the inset showing an enhanced view of teh DOS at and around VBM and CBM.

clearly shown at the right side of figure 52, where O-states have been given an orange color and Cu-states have been given a blue color.

The results in figure 52 have been modified so that the bandgap is manually set to 2.1 eV to match experimental results. The electronic band structure of the conduction band are hence shifted to more positive values but remain otherwise unchanged. The resulting band structure is in good agreement with other works on *ab initio* calculations on the Cu₂O structure, showing a direct bandgap in the Γ-point and similar curvature of the CBM and VBM. This work also finds the valence band to be primarily build up of Cu-3d states, which is also in good agreement with other works.

A qualitative analysis of the electronic band structure of Cu₂O in figure 52, according to equation (2.5) and (2.6), reveals that the effective mass of holes is higher than that of electrons in the Γ-point, i.e., the
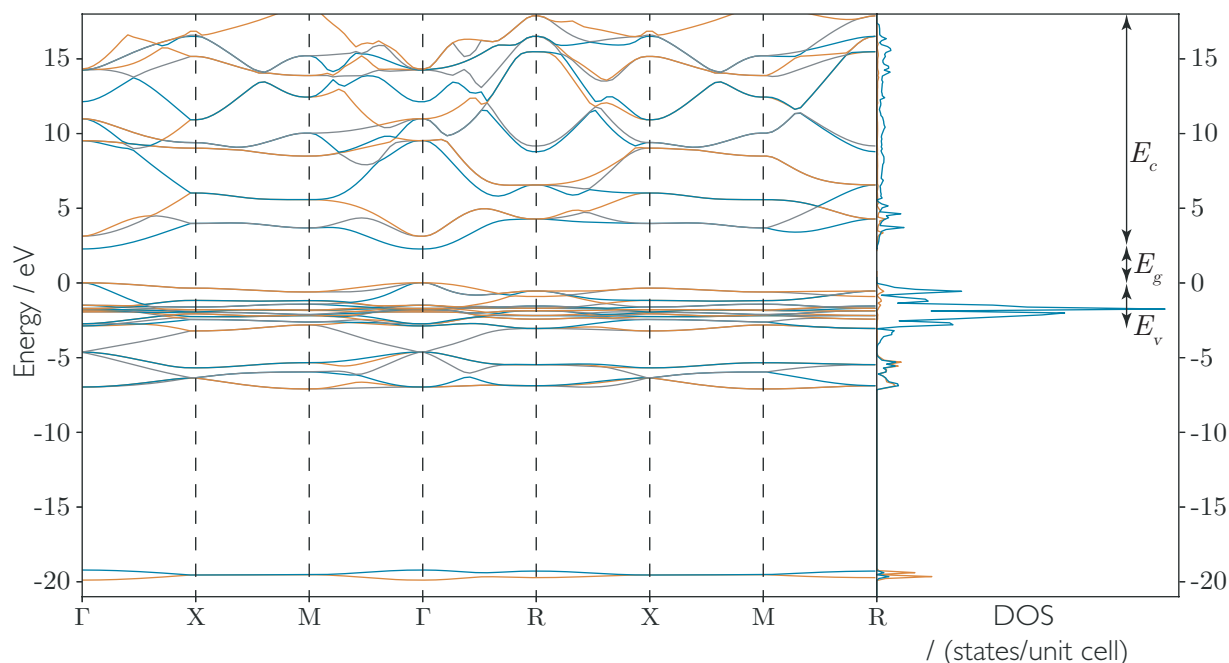

figure 52: Calculation of electronic band structure and DOS of Cu₂O using the PBE functional

curvature in the valence band is smaller than in the conduction band. Since the mobility of charge carriers are inversely proportional to the effective mass, the mobility of electrons (in the conduction band) is higher than the mobility of holes (in the valence band). In general, it is observed that the bands below the valence band have much less curvature than the bands above the conduction band, and electrons excited to any of these bands will experience high mobility. This feature is highly favorable in STH operation as electrons are required to go to the surface to reduce hydrogen efficiently.

6   Conclusions

In this work, electrodeposited cuprous oxide photocathodes are investigated as a candidate for use in photoelectrochemical cells. Through investigating the electrodeposition system, spontaneous potential oscillations arising from pH fluctuations at the electrode was encountered. This study offers evidence of metallic Cu depositing as a direct consequence of these oscillations. Through this investigation and the understanding gained thereof, the oscillations were eradicated, and highly crystalline Cu_2O was achieved.

Several substrates were used to deposit Cu_2O, and it was found that stainless steel mesh outperformed Ti-mesh and carbon-paper substrates in regards to surface coverage, reproducibility and measured photocurrents. The best performing Cu_2O electrode on stainless steel mesh exhibited a photocurrent of -1.1 mA cm^{-2} at -0.6 V vs. SCE in a 0.5 M $NaSO_4$ electrolyte after being deposited galvanostatically at -0.1 mA for 120 minutes at 30°C. Chronoamperometry confirmed expected photocorrosion, and a drop in photocurrent to less than 15% of the initial value was encountered after ~250 s of illumination.

By covering the Cu_2O electrode with a layer of amorphous TiO_2, an increase in photocurrent to 1.38 mA cm^{-2} at -0.6 V vs. SCE in a 0.5 M $NaSO_4$ electrolyte was observed. This was 0.28 mA higher than the best *bare* Cu_2O electrode, as mentioned above, and approximately ten times higher than that found in reference samples with the same deposition parameters. However, electrode instability persisted, and after ~280 s of illumination photocurrents dropped to less than 10% of the initial photocurrent.

In addition, an all solid-state photoelectrochemical device was accomplished, and a maximum photovoltage of +120 mV was achieved. The solid-state cell, with an illuminated Cu_2O photocathode, exhibited a photocurrent of -1.5 μA cm^{-2} at -2.0 V vs. the Pt-C electrocatalyst anode under purely wet gaseous conditions, at room temperature.

Outlooks

Because of the stability and favourable bandgap, $CuFeO_2$ is an exciting material and could become an essential photocathode material in the future. To successfully achieve $CuFeO_2$ electrodes by electrochemical deposition, a thorough investigation of the deposition solution will be needed. By establishing the reduction potentials relevant to accomplish the co-deposition of Fe_2O_3 and Cu_2O, more accurate deposition parameters must be determined.

The most significant concern in using Cu_2O as a photocathode material in solar-to-hydrogen systems is the stability. A lot of work has already been directed towards finding solutions to the instability, but more work is needed. It is interesting how continued hydrogen evolution over a 1900 hour period has been shown in the literature, and that no one can reproduce these experiments in solid electrode operations. If a solution exists to this problem, it could be linked with grain size in the crystal structures, an effect of grain boundaries and nano-size effects; tunable parameters when using electrochemical deposition.

The increase in photocurrent when covering the Cu_2O electrode by PLD deposited TiO_2 is assumed to arise because of band alignments at the Cu_2O/TiO_2 interface. However, by examining the layer by x-ray photoelectron spectroscopy (XPS), it is possible to determine the valence of Ti in the amorphous layer and gain valuable insight into the mechanisms at play.The investigation of amorphous structures for such applications is also becoming important and more studies (experimental and theoretical) are needed.

Bibliography

[1] Norwegian Research Council, (2017). Annual Report 2017. URL: https://www.forskningsradet.no/no/Arsrapport/1254018067302

[2] Corby, S. (2017). Hydrogen is the future, not battery-electric cars: Lexus | CarAdvice. Retrieved May 2, 2018, from https://www.caradvice.com.au/588509/hydrogen-is-the-future-not-battery-electric-cars-lexus/

[3] U.S. Department of Energy, (2016). Fuel Cells Powering Critical Infrastructure in Disasters. Retrieved from https://www.energy.gov/sites/prod/files/2016/12/f34/fcto_fuel_cells_during_storms.pdf

[4] U.S. Department of Energy, (2015). Fuel Cell Technologies Office, Multi-Year Research, Development, and Demonstration Plan, 11007, 1-44. https://www.energy.gov/eere/fuelcells/downloads/fuel-cell-technologies-office-multi-year-research-development-and-22

[5] Septina, W., & Tilley, S. D. (2017). Emerging Earth-abundant materials for scalable solar water splitting. Current Opinion in Electrochemistry, 2(1), 120–127. https://doi.org/10.1016/j.coelec.2017.03.010

[6] Paracchino, A., Laporte, V., Sivula, K., Grätzel, M., & Thimsen, E. (2011). Highly active oxide photocathode for photoelectrochemical water reduction. Nature Materials, 10(6), 456–461. https://doi.org/10.1038/nmat3017

[7] Hu, S., Xiang, C., Haussener, S., Berger, A. D., & Lewis, N. S. (2013). An analysis of the optimal band gaps of light absorbers in integrated tandem photoelectrochemical water-splitting systems. Energy & Environmental Science, 6(10), 2984. https://doi.org/10.1039/c3ee40453f

[8] Schöppel, H. R. and Gerischer, H. (1971), Die kathodische Reduktion von Cu-I-oxid-Elektroden als Beispiel für den Mechanismus der Reduktion eines Halbleiter-Kristalls. Berichte der Bunsengesellschaft für physikalische Chemie, 75: 1237-1239.

[9] Xu, K., Chatzitakis, A., & Norby, T. (2016). Solid-state photoelectrochemical cell with TiO_2 nanotubes for water splitting. Photochem. Photobiol. Sci., 238, 37–38. https://doi.org/10.1039/C6P-P00217J

[10] Busch, G. (1989). Early history of the physics and chemistry of semiconductors-from doubts to fact in a hundred years. European Journal of Physics, 10(4), 254.

[11] Becquerel, E. (1839). Memoire Sur Les Effets Électriques Produits Sous L'influence Des Rayons Solaires. Comptes Rendus, 9, 561-567.

[12] Peter, L. M. (2016). Semiconductor electrochemistry. In Photoelectrochemical Solar Fuel Production: From Basic Principles to Advanced Devices (pp. 3–40). https://doi.org/10.1007/978-3-319-29641-8_1

[13] Streetman, B.G. & Banerjee, S.K. (2015). Solid State Electronic Devices: Global Edition, Pearson.

[14] Würfel P. & Würfel U. (2009). Physics of solar cells. From basic principles to advanced concepts. Wiley, Weinheim

[15] Bard, A., & Faulkner, L. (2001). Electrochemical methods: Fundamentals and applications (2nd ed.). New York: Wiley.

[16] Grätzel, M. (2001). Photoelectrochemical cells. Nature. https://doi.org/10.1038/35104607

[17] Gelderman, K., Lee, L., & Donne, S. W. (2007). Flat-Band Potential of a Semiconductor: Using the Mott–Schottky Equation. Journal of Chemical Education, 84(4), 685. https://doi.org/10.1021/ed084p685

[18] Bak, T., Nowotny, J., Rekas, M., & Sorrell, C. (2002). Photo-electrochemical hydrogen generation from water using solar energy. Materials-related aspects. International Journal of Hydrogen Energy, 27(10), 991–1022. https://doi.org/10.1016/S0360-3199(02)00022-8

[19] Sholl, D. S. & Steckel, J. A. (2009). Density Functional Theory: A Practical Introduction, John Wiley & Sons, Inc., Hoboken, NJ, USA.

[20] Hohenberg, P., & Kohn, W. (1964). Inhomogeneous Electron Gas, 136(3B), B864–B871. https://doi.org/10.1103/PhysRev.136.B864

[21] Kohn, W., & Sham, L. J. (1965). Self-Consistent Equations Including Exchange and Correlation Effects. Physical Review, 140(4A), A1133–A1138. https://doi.org/10.1103/PhysRev.140.A1133

[22] Perdew, J. P. & Wang, Y. (1992). Accurate and simple analytic representation of the electron-gas correlation energy. Physical Review B, 45(23), 13244–13249. https://doi.org/10.1103/PhysRevB.45.13244

[23] Perdew, J. P., Burke, K. & Ernzerhof, M. (1996). Generalized gradient approximation made simple. Physical Review Letters, 77(18), 3865–3868. https://doi.org/10.1103/PhysRevLett.77.3865

[24] Perdew, J. P., Ernzerhof, M., & Burke, K. (1996). Rationale for mixing exact exchange with density functional approximations. Journal of Chemical Physics, 105(22), 9982–9985. https://doi.org/10.1063/1.472933

[25] Heyd, J., Scuseria, G. E., & Ernzerhof, M. (2003). Hybrid functionals based on a screened Coulomb potential. Journal of Chemical Physics, 118(18), 8207–8215. https://doi.org/10.1063/1.1564060

[26] Grondahl, L. O. (1927). Unidirectional current-carrying device, U.S. Patent 1,640,335

[27] Grondahl, L. O. (1926). Theories of a new solid junction rectifier. Science, 64(1656).

[28] Ito, T., Yamaguchi, H., Okabe, K., & Masumi, T. (1998) Single-crystal growth and characterization of Cu_2O and CuO. Journal of Materials Science, 33(14), 3555–3566. https://doi.org/10.1023/A:1004690809547

[29] Rakhshani, A. E., Al-Jassar, A. A., & Varghese, J. (1987). Electrodeposition and characterization of cuprous oxide. Thin Solid Films, 148(2), 191–201. https://doi.org/10.1016/0040-6090(87)90157-X

[30] Paracchino, A., Brauer, J. C., Moser, J. E., Thimsen, E., & Graetzel, M. (2012). Synthesis and characterization of high-photoactivity electrodeposited Cu_2O solar absorber by photoelectrochemistry and ultrafast spectroscopy. Journal of Physical Chemistry C, 116(13), 7341–7350. https://doi.org/10.1021/jp301176y

[31] de Jongh, P. E., Vanmaekelbergh, D., & Kelly, J. J. (1999). Cu_2O: Electrodeposition and Characterization. Chemistry of Materials, 11(12), 3512–3517. https://doi.org/10.1021/cm991054e

[32] Yang, W. Y., Kim, W. G., & Rhee, S. W. (2008). Radio frequency sputter deposition of single phase cuprous oxide using Cu_2O as a target material and its resistive switching properties. Thin Solid Films, 517(2), 967–971. https://doi.org/10.1016/j.tsf.2008.08.184

[33] Dolai, S., Das, S., Hussain, S., Bhar, R., & Pal, A. K. (2017). Cuprous oxide (Cu_2O) thin films prepared by reactive d.c. sputtering technique. Vacuum, 141, 296–306. https://doi.org/10.1016/j.vacuum.2017.04.033

[34] Ahn, J. S., Pode, R., & Lee, K. B. (2017). Stoichiometric p-type Cu_2O thin films prepared by reactive sputtering with facing target. Thin Solid Films, 623, 121–126. https://doi.org/10.1016/j.tsf.2017.01.008

[35] Sun, H., Chen, S.-C., Wen, C.-K., Chuang, T.-H., Arab Pour Yazdi, M., Sanchette, F., & Billard, A. (2017). p-type cuprous oxide thin films with high conductivity deposited by high power impulse magnetron sputtering. Ceramics International, 43(8), 6214–6220. https://doi.org/10.1016/j.ceramint.2017.02.019

[36] Kawaguchi, K., Kita, R., Nishiyama, M., & Morishita, T. (1994). Molecular beam epitaxy growth of CuO and Cu_2O films with controlling the oxygen content by the flux ratio of Cu/O^+. Journal of Crystal Growth, 143(3–4), 221–226. https://doi.org/10.1016/0022-0248(94)90059-0

[37] Kracht, M., Schörmann, J., & Eickhoff, M. (2016). Plasma assisted molecular beam epitaxy of Cu_2O on MgO(001): Influence of copper flux on epitaxial orientation. Journal of Crystal Growth, 436, 87–91. https://doi.org/10.1016/j.jcrysgro.2015.11.041

[38] Ogale, S. B., Bilurkar, P. G., Mate, N., Kanetkar, S. M., Parikh, N., & Patnaik, B. (1992). Deposition of copper oxide thin films on different substrates by pulsed excimer laser ablation. Journal of Applied Physics, 72(8), 3765–3769. https://doi.org/10.1063/1.352271

[39] Chen, A., Long, H., Li, X., Li, Y., Yang, G., & Lu, P. (2009). Controlled growth and characteristics of single-phase Cu_2O and CuO films by pulsed laser deposition. Vacuum, 83(6), 927–930. https://doi.org/10.1016/j.vacuum.2008.10.003

[40] Meyer, B. K., Polity, A., Reppin, D., Becker, M., Hering, P., Klar, P. J., … Ronning, C. (2012). Binary copper oxide semiconductors: From materials towards devices. Physica Status Solidi (B), 249(8), 1487–1509. https://doi.org/10.1002/pssb.201248128

[41] Pollack, G. P., & Trivich, D. (1975). Photoelectric properties of cuprous oxide. Journal of Applied Physics, 46(1), 163–172. https://doi.org/10.1063/1.321312

[42] Stareck, J. E. (1943). Electrodeposition of cuprous oxides and baths therefor, U.S. Patent 2,313,454

[43] Yang, Y. (2017). Electrodeposition of p-Type Cuprous Oxide and its Application in Oxide Solar Cells (Doctoral dissertation). University of Waterloo, Ontario, Canada. http://hdl.handle.net/10012/11150

[44] Switzer, J. A., Hung, C.-J., Huang, L.-Y., Miller, F. S., Zhou, Y., Raub, E. R., … Bohannan, E. W. (1998). Potential oscillations during the electrochemical self-assembly of copper/cuprous oxide layered nanostructures. Journal of Materials Research, 13(4), 909–916. https://doi.org/10.1557/JMR.1998.0124

[45] Leopold, S., Herranen, M., & Carlsson, J.-O. (2001). Spontaneous Potential Oscillations in the Cu(II)/Tartrate and Lactate Systems, Aspects of Mechanisms and Film Deposition. Journal of The Electrochemical Society, 148(8), C513. https://doi.org/10.1149/1.1379949

[46] Wisniak, J. (2009). Charles Friedel. Educación Química, 20, 447–455.

[47] Rogers, A. F. (1913). Delafossite, a Cuprous Metaferrite from Bisbee, Arizone. American Journal of Science, 35(4), 290–294. https://doi.org/10.2475/ajs.s4-35.207.290

[48] Pabst, A. (1946). Notes on the Structure of Delafossite. American Mineralogist, 31(11), 539–546. Retrieved from http://www.minsocam.org/ammin/AM31/AM31_539.pdf

[49]   Soller, W., & Thompson, A. J. (1935). The Crystal Structure of Cuprous Ferrite. American Journal of Physical Review 47, 644.

[50]   Effenberger, H. (1991). Structure of hexagonal copper(I) ferrite. Acta Crystallographica Section C, 47(12), 2644–2646. https://doi.org/10.1107/S0108270191006790

[51]   Zhao, T.-R., Hasegawa, M., & Takei, H. (1996). Crystal growth and characterization of cuprous ferrite ($CuFeO_2$). Journal of Crystal Growth, 166(1–4), 408–413. https://doi.org/10.1016/0022-0248(95)00520-X

[52]   John, M., Heuss-A??bichler, S., Park, S. H., Ullrich, A., Benka, G., Petersen, N., … Horn, S. R. (2016). Low-temperature synthesis of $CuFeO_2$ (delafossite) at 70°C: A new process solely by precipitation and ageing. Journal of Solid State Chemistry, 233, 390–396. https://doi.org/10.1016/j.jssc.2015.11.011

[53]   Pierre Villars (Chief Editor), PAULING FILE in: Inorganic Solid Phases, SpringerMaterials (online database), Springer, Heidelberg (ed.) SpringerMaterials

[54]   Momma, K. & Izumi, F. (2011). VESTA 3 for three-dimensional visualization of crystal, volumetric and morphology data. Journal of Applied Crystallography. 44, 1272-1276.

[55]   Prévot, M. S., Jeanbourquin, X. A., Bourée, W. S., Abdi, F., Friedrich, D., van de Krol, R., … Sivula, K. (2017). Evaluating Charge Carrier Transport and Surface States in $CuFeO_2$ Photocathodes. Chemistry of Materials, 29(11), 4952–4962. https://doi.org/10.1021/acs.chemmater.7b01284

[56]   Chen, H.-Y., & Wu, J.-H. (2012). Characterization and optoelectronic properties of sol–gel-derived $CuFeO_2$ thin films. Thin Solid Films, 520, 5029–5035. https://doi.org/10.1016/j.tsf.2012.03.032

[57]   Deng, Z., Fang, X., Wu, S., Dong, W., Shao, J., Wang, S., & Lei, M. (2014). The morphologies and optoelectronic properties of delafossite $CuFeO_2$ thin films prepared by PEG assisted sol-gel method. Journal of Sol-Gel Science and Technology, 71(2), 297–302. https://doi.org/10.1007/s10971-014-3369-6

[58]   Xiong, D., Qi, Y., Li, X., Liu, X., Tao, H., Chen, W., & Zhao, X. (2015). Hydrothermal synthesis of delafossite $CuFeO_2$ crystals at 100°C. RSC Adv., 5(61), 49280–49286. https://doi.org/10.1039/C5RA08227G

[59]   Choi, D. H., Moon, S. J., Hong, J. S., An, S. Y., Shim, I.-B., & Kim, C. S. (2009). Impurity dependent semiconductor type of epitaxial $CuFeO_2$ (111) thin films deposited by using a pulsed laser deposition. Thin Solid Films, 517, 3987–3989. https://doi.org/10.1016/j.tsf.2009.01.111

[60]   Li, S. Z., Liu, J., Wang, X. Z., Yan, B. W., Li, H., & Liu, J. –M. (2012). Epitaxial growth of delafossite $CuFeO_2$ thin films by pulse laser deposition. Physica B: Condensed Matter, 407(13), 2412–2415. https://doi.org/10.1016/j.physb.2012.03.037

[61]   Barnabé, A., Mugnier, E., Presmanes, L., & Tailhades, P. (2006). Preparation of delafossite $CuFeO_2$ thin films by rf-sputtering on conventional glass substrate. Materials Letters, 60(29–30), 3468–3470. https://doi.org/10.1016/j.matlet.2006.03.033

[62]   Deng, Z., Fang, X., Wang, X., Wu, S., Dong, W., Shao, J., & Tao, R. (2015). Characterization of amorphous p-type transparent $CuFeO_2$ thin films prepared by radio frequency magnetron sputtering method at room temperature. Thin Solid Films, 589, 17–21. https://doi.org/10.1016/j.tsf.2015.04.066

[63]   Read, C. G., Park, Y., & Choi, K.-S. (2012). Electrochemical Synthesis of p-Type $CuFeO_2$ Electrodes for Use in a Photoelectrochemical Cell. The Journal of Physical Chemistry Letters, 3(14), 1872–1876. https://doi.org/10.1021/jz300709t

[64] Riveros, G., Garín, C., Ramírez, D., Dalchiele, E. A., Marotti, R. E., Pereyra, C. J., … Ramos-Barrado, J. R. (2015). Delafossite $CuFeO_2$ thin films electrochemically grown from a DMSO based solution. Electrochimica Acta, 164, 297–306. https://doi.org/10.1016/j.electacta.2015.02.226

[65] Garrels, R. M., & Christ, C. M. (1965). Solutions, Minerals, and Equilibria. Harpers' Geoscience Series. Harper and Row, New York.

[66] Fujishima, A., & Honda, K. (1972). Electrochemical Photolysis of Water at a Semiconductor Electrode. Nature, 238(5358), 37–38. https://doi.org/10.1038/238037a0

[67] Yoneyama, H., Sakamoto, H., & Tamura, H. (1975). A Photo-electochemical cell with production of hydrogen and oxygen by a cell reaction. Electrochimica Acta, 20(5), 341–345. https://doi.org/10.1016/0013-4686(75)90016-X

[68] Roger, I., Shipman, M. A., & Symes, M. D. (2017). Earth-abundant catalysts for electrochemical and photoelectrochemical water splitting. Nature Reviews Chemistry. Nature Publishing Group. https://doi.org/10.1038/s41570-016-0003

[69] Young, J. L., Steiner, M. A., Döscher, H., France, R. M., Turner, J. A., & Deutsch, T. G. (2017). Direct solar-to-hydrogen conversion via inverted metamorphic multi-junction semiconductor architectures. Nature Energy, 2(4). https://doi.org/10.1038/nenergy.2017.28

[70] Hara, M., Kondo, T., Komoda, M., Ikeda, S., Shinohara, K., Tanaka, A., … Tanaka, A. (1998). Cu_2O as a photocatalyst for overall water splitting under visible light irradiation. Chemical Communications, 2(3), 357–358. https://doi.org/10.1039/a707440i

[71] de Jongh, P. E., Vanmaekelbergh, D., & Kelly, J. J. (2000). Photoelectrochemistry of Electrodeposited Cu_2O. Journal of The Electrochemical Society, 147(2), 486-489. https://doi.org/10.1149/1.1393221

[72] Nian, J. N., Hu, C. C., & Teng, H. (2008). Electrodeposited p-type Cu_2O for H_2 evolution from photoelectrolysis of water under visible light illumination. International Journal of Hydrogen Energy, 33(12), 2897–2903. https://doi.org/10.1016/j.ijhydene.2008.03.052

[73] Jang, Y. J., Park, Y. Bin, Kim, H. E., Choi, Y. H., Choi, S. H., & Lee, J. S. (2016). Oxygen-Intercalated $CuFeO_2$ Photocathode Fabricated by Hybrid Microwave Annealing for Efficient Solar Hydrogen Production. Chemistry of Materials, 28(17), 6054–6061. https://doi.org/10.1021/acs.chemmater.6b00460

[74] Prévot, M. S. (2017). Investigating and controlling charge carrier behavior in p-type delafossite $CuFeO_2$ photocathodes for solar fuel production (Doctoral dissertation). École Polytechnique Fédérale de Lausanne. Retrieved from https://infoscience.epfl.ch/record/230138/files/EPFL_TH7915.pdf

[75] Prévot, M. S., Li, Y., Guijarro, N., & Sivula, K. (2016). Improving charge collection with delafossite photocathodes: a host–guest $CuAlO_2/CuFeO_2$ approach. J. Mater. Chem. A, 4(8), 3018–3026. https://doi.org/10.1039/C5TA06336A

[76] Tablero Crespo, C. (2018). Potentiality of $CuFeO_2$-delafossite as a solar energy converter. Solar Energy, 163, 162–166. https://doi.org/10.1016/j.solener.2018.01.091

[77] Isseroff, L. Y., & Carter, E. A. (2012). Importance of reference Hamiltonians containing exact exchange for accurate one-shot GW calculations of Cu_2O. PHYSICAL REVIEW B, 8522. https://doi.org/10.1103/PhysRevB.85.235142

[78] Bendavid, L. I., & Carter, E. A. (2013). First-principles predictions of the structure, stability, and photocatalytic potential of Cu_2O surfaces. Journal of Physical Chemistry B, 117(49), 15750–15760. https://doi.org/10.1021/jp406454c

[79] Heinemann, M., Eifert, B., & Heiliger, C. (2013). Band structure and phase stability of the copper oxides Cu_2O, CuO, and Cu_4O_3. Physical Review B, 87(11), 115111. https://doi.org/10.1103/PhysRevB.87.115111

[80] Raebiger, H., Lany, S., & Zunger, A. (2007). Origins of the p-type nature and cation deficiency in Cu_2O and related materials. Physical Review B - Condensed Matter and Materials Physics, 76(4). https://doi.org/10.1103/PhysRevB.76.045209

[81] Beverskog, B., & Puigdomenech, I. (1995). Revised Pourbaix Diagrams for Copper at 5 to 150°C. Swedish Nuclear Power Inspectorate, (SKI Report 95:73).

[82] Kirfel, A., & Eichhorn, K. (1990). Accurate structure analysis with synchrotron radiation. The electron density in Al_2O_3 and Cu_2O. Acta Crystallographica A, 46(4), 271 - 284. https://doi.org/10.1107/S0108767389012596

Appendix - HSE

Risk Assesment of CuSO₄ / Lactic Acid Solution

0.2 M CuSO$_4$ ≈ 3% solution.

CuSO$_4$ CLP classifications:

H302 Harmful if swallowed

- using table 3.1.2 of CLP regulations (oral exposure route) shows Cat.4 and converted acute toxicity point meas. = 500

- equation 3.1.3.6.1

  $$ATE_{mix} = (100 \times ATE_i) / C_i = (100 \times 500) / 3(\%) \approx 1.6 \times 10^4$$

- using table 3.1.1 shows $1.6 \times 10^4 > 2000$ resulting in H302 not applying to a 3% CuSO$_4$ solution

  H302 N/A

H315 Causes skin irritation (skin irr. 2)

- table 3.2.3 in CLP regulations show that concentrations must exceed 10% to be applicable

  H315 N/A

H319 Causes serious eye irritation (eye irr. 2)

- table 3.3.3 in CLP regulations show that concentrations must exceed 10% to be applicable

  H319 N/A

H400 Very toxic to aquatic life (aquatic acute 1)

- using lowest given value in chapter 12 of SDS → 0.024 mg l^{-1}

- for this value, table 4.1.3 in CLP regulations gives a multiplying factor of M = 10

- according to table 4.1.1 in CLP regulations: $3\% \times 10 = 30\% > 25\%$, resulting in acute category 1

  H400 applicable

H410 Very toxic to aquatic life with long lasting effect (aquatic chronic 1)

- using lowest given value in chapter 12 of SDS → 0.024 mg l^{-1}

- for this value, table 4.1.3 in CLP regulations gives a multiplying factor of M = 10

- according to table 4.1.2 in CLP regulations: $3\% \times 10 = 30\% > 25\%$, resulting in chronic category 1

  H410 applicable

3.0 M lactic acid ≈ 22% solution

Lactic acid CLP classifications:

H318 Causes serious eye damage (eye dam. 1)

- concentrations > 3% resulta in eye dam. 1

H318 applicable

H315 Causes skin irritation (skin irr. 2)

concentration > 10% resulting in skin irr. 2

H315 applicable

2.0 M KOH ≈ 12% solution

KOH CLP classifications:

H302 Harmfull if swallowed (acute tox. 4)

- using table 3.1.2 of CLP regulations (oral exposure route) shows Cat.4 and converted acute toxicity point meas. = 500
- equation 3.1.3.6.1

    $ATE_{mix} = (100 \times ATE_i) / C_i = (100 \times 500) / 12(\%) \approx 4.1 \times 10^3$

- using table 3.1.1 shows $1.6 \times 10^4 > 2000$ resulting in H302 not applying to a 3% $CuSO_4$ solution

    H302 N/A (however applicable above 25% solution)

H314 Causes severe skin burns and eye damage (skin corr. 1A)

- CLP regulations states that concentrations above 5% results in skin corr. 1A

    H314 applicable

Risk Assesment of $CuCl_2$ / $Fe(ClO_4)_3$ / $LiClO_4$ / DMSO solution

0.01M $CuCl_2$ ≈ 0.12%

$CuCl_2$ CLP classifications:

H302 Harmful if swallowed

- using table 3.1.2 of CLP regulations (oral exposure route) shows Cat.4 and converted acute toxicity point meas. = 500
- equation 3.1.3.6.1

    $ATE_{mix} = (100 \times ATE_i) / C_i = (100 \times 500) / 0.12(\%) \approx 4.2 \times 10^5$

- using table 3.1.1 shows $4.01 \times 10^5 > 2000$ resulting in H302 not applying to a 0.12% $CuCl_2$ solution

    H302 N/A

H312 Harmful in contact with skin (acute tox. 4)

- using table 3.1.2 of CLP regulations (oral exposure route) shows Cat.4 and converted acute toxicity point meas. = 1100
- equation 3.1.3.6.1

    $ATE_{mix} = (100 \times ATE_i) / C_i = (100 \times 1100) / 0.12(\%) \approx 9.2 \times 10^5$

- using table 3.1.1 shows $9.2 \times 10^5 > 2000$ resulting in H312 not applying to a 0.12% $CuCl_2$ solution

H302 N/A

H315 Causes skin irritation (skin irr. 2)

- table 3.2.3 in CLP regulations show that concentrations must exceed 10% to be applicable

  H315 N/A

H318 Causes serious eye damage (eye dam. 1)

- concentrations > 3% results in eye dam. 1, concentrations > 1% results in eye irr. 2.

  H318 N/A

H400 Very toxic to aquatic life (aquatic acute 1)

  H400 N/A (as per chapter 4 of CLP regulations)

H411 Toxic to aquatic life with long lasting effects (aquatic chronic 2)

  H411 N/A (as per chapter 4 of CLP regulations)

0.005 M Fe(ClO$_4$)$_3$ ≈ 0.15%

Fe(ClO$_4$)$_3$ CLP classifications:

H315 Causes skin irritation (skin irr. 2)

- table 3.2.3 in CLP regulations show that concentrations must exceed 10% to be applicable

  H315 N/A

H319 Causes serious eye irritation (eye irr. 2)

- table 3.3.3 in CLP regulations show that concentrations must exceed 10% to be applicable

  H319 N/A

H335 May cause respiratory irritation (STOT SE 3)

- table 3.8.3.4.5 in CLP regulations show that concentrations must exceed 20% to be applicable

  H335 N/A

0.1 M LiClO$_4$ ≈ 0.95%

LiClO$_4$ CLP classifications:

H315 Causes skin irritation (skin irr. 2)

- table 3.2.3 in CLP regulations show that concentrations must exceed 10% to be applicable

  H315 N/A

H319 Causes serious eye irritation (eye irr. 2)

- table 3.3.3 in CLP regulations show that concentrations must exceed 10% to be applicable

  H319 N/A

H335 May cause respiratory irritation (STOT SE 3)

- table 3.8.3.4.5 in CLP regulations show that concentrations must excede 20% to be applicable

  H335 N/A

DMSO - not hazardous according to SDS

Note on the above risk assessment:

Mixing these solutions was done in a fume hood, as the chemicals themselves can pose risk. Especially $LiClO_4$ were treated with extra caution because of the H335 label and a dust mask was used at all times handling this outside the fume hood. In addition, gloves and protective glasses was always used when working with any chemical.

Labels for chemicals

Copper (II) Sulphate,
3 % CuSO₄ (0.2 mol/l),
CAS nr. 7758-98-7,

Lactic acid
23% Lactic acid
50-21-5

Danger
Causes serious eye damage
Causes skin irritation
Very toxic to aquatic life with long lasting effects

Wear protective gloves and eye protection. IF IN EYES: Rinse cautiously with water for several minutes. Remove contact lenses, if present and easy to do. Continue rinsing. Immediately call a POISON CENTER (22591300)/ doctor(113). IF ON SKIN: Wash with plenty of water. Avoid release to the environment. Collect spillage. Dispose of contents / container to an approved waste disposal plant.

Made by   Date
Lars Kristian Henriksen   08 feb 17

Potassium Hydroxide
12% KOH (2.0 M)
CAS nr. 1310-58-3

Danger
Causes severe skin burns and eye damage

Wear protective gloves and eye protection. IF IN EYES: Rinse cautiously with water for several minutes. Remove contact lenses, if present and easy to do. Continue rinsing. IF ON SKIN (or hair): Take off immediately all contaminated clothing. Rinse skin with water [or shower]. IF SWALLOWED: Rinse mouth. Do NOT induce vomiting. If INHALED: Remove person to fresh air and keep comfortable for breathing.

Made by   Date
Lars Kristian Henriksen   29 aug 17

C₂H₆SO
DMSO
Solvent
CAS # 67-68-5

CuCl₂
0.01M (0.12%)
7447-39-4

Fe(ClO₄)₃
0.005M (0.15%)
15201-61-3

LiClO₄
0.1M (0.95%)
7791-03-9

Not a hazardous mixture.
Not a hazardous mixture.

If breathed in, move person into fresh air. If not breathing, give artificial respiration. Consult a physician. In case of skin contact, wash off with soap and plenty of water. Consult a physician. In case of eye contact, flush eyes with water as a precaution. If swallowed, do NOT induce vomiting. Never give anything by mouth to an unconscious person. Rinse mouth with water. Consult a physician.

Made by   Date
Lars Kristian Henriksen   _____

figure 53: Chemical labels made for solutions used in this work.